Flexible devices for energy harvesting based on printed organic piezoelectric P(VDF-TrFE) materials

Elena Gusarova

Communauté
UNIVERSITÉ Grenoble Alpes

THÈSE

Pour obtenir le grade de

DOCTEUR DE LA COMMUNAUTÉ UNIVERSITÉ GRENOBLE ALPES

Spécialité : **Nanoélectronique et nanotechnologie**

Arrêté ministériel : 7 août 2006

Présentée par

Elena Gusarova

Thèse dirigée par **Bernard Viala**

préparée au sein du **Laboratoire CEA-Leti**
dans **l'École Doctorale d'Electronique, Electrotechnique, Automatique, Traitement du Signal (EEATS)**

Dispositifs souples pour la récupération d'énergie à base de matériaux organiques piézoélectriques P(VDF-TrFE) imprimés

Thèse soutenue publiquement le **16 décembre 2015**,
Devant le jury composé de:

Dr. Paul Muralt
Professeur, EPFL, Rapporteur et président
Dr. Philippe Pernod
Professeur, Ecole Centrale de Lille, Rapporteur
Dr. Ian Cayrefourcq
Docteur Ingénieur, Directeur des technologies Emergentes, Arkema-France, Membre
Dr. Bernard Viala
Ingénieur de Recherche, HDR, CEA-Leti, Directeur de thèse
Dr. Orphée Cugat
Directeur de Recherche, CNRS, G2ELab, Co-directeur de thèse
Dr. Leticia Gimeno
Maitre de conférences, UJF/UGA, G2ELab, Encadrant
Dr. Romain Gwoziecki
Ingénieur de Recherche, CEA-Liten, Invité
Dr. Fabrice Domingues Dos Santos
Docteur Ingénieur, Président Piezotech, Invité

Résumé

Le but de cette thèse était d'étudier des solutions innovantes pour la récupération d'énergie pour pouvoir alimenter de manière autonome les futurs capteurs et nœuds communicants sans fil de l'Internet des Objets (IoT pour Internet of Things). Le travail s'est focalisé sur des matériaux piézoélectriques souples et sur une approche composite et multiphysique. L'objectif est de récupérer de l'énergie à partir de déformations directes ou induites provenant de sources à la fois mécaniques et thermiques et en particulier de sources négligées jusqu'alors (lentes et de faibles intensités). L'idée maitresse est l'hybridation de plusieurs matériaux fonctionnels avec un cœur du système constitué par des microgénérateurs piézoélectriques (et pyroélectriques) imprimés nécessaires à la génération de charges électriques. L'originalité de ce travail est d'avoir réalisé un système de récupération d'énergie entièrement flexible, au format d'une carte de crédit et compatible avec de plus grandes dimensions, en utilisant des copolymères piézoélectriques de P(VDF-TrFE) sous forme d'encres. Ce matériau est flexible et particulièrement résistant, ce qui le rend attractif pour des applications mettant en jeu formes complexes, notamment, courbes. Un autre avantage du copolymère de P(VDF-TrFE) est qu'il ne nécessite pas de pré-déformation mécanique comme pour le polymère PVDF et il commence à être aujourd'hui disponible sous forme d'encres pour l'électronique imprimée, ce qui simplifiera et réduira les coûts de fabrication à termes.

En premier, nous décrivons le procédé de fabrication par sérigraphie des microgénérateurs en P(VDF-TrFE), suivi par les caractérisations ferroélectriques puis piézoélectriques des dispositifs. A cet effet, nous avons développé des techniques de mesures originales en circuit ouvert qui ont été testées et validées au préalable avec des échantillons de PVDF commercial. La dernière étape a été de réaliser un prototype de récupération d'énergie thermique flexible de faible encombrement (sans radiateur). Cela a été réalisé en hybridant les microgénérateurs précédemment fabriqués avec des feuilles d'alliages à mémoire de forme thermique à base de NiTi, qui est un matériau sensible à un seuil de température donnée.

Les résultats phares de cette étude sont : 1) le dépôt multicouches de P(VDF-TrFE) combiné au dépôt d'une électrode souple en PEDOT:PSS, 2) l'établissement des caractéristiques ferroélectriques et piézoélectriques en fonction de l'épaisseur de P(VDF-TrFE) et enfin 3) la détermination d'un coefficient g_{31} supérieur à la normale avec 0.15 V·m/N. Aussi, nous avons démontré la capacité de ces microgénérateurs à délivrer des

tensions utiles de l'ordre de 10 V avec ici une densité d'énergie de proche de 500 μJ/cm^3, ces valeurs étant limitées aux conditions de test utilisées.

Nous concluons ce travail sur une preuve de concept fonctionnelle de récupérateur d'énergie thermique flexible apte à détecter ou utiliser des variations lentes et faibles de température à partir de sources élémentaires, produisant pour l'instant 37 V (correspondant à 95 μJ) à 65 ºC, et qui à termes pourront être l'air ambiant (chaud ou froid) ou la chaleur de la peau.

Abstract

This work aims to study innovative solutions for energy harvesting applicable to autonomous wireless sensors for IoT (Internet of Things). It is focused on flexible piezoelectric composite materials and a multi-physical approach. The objective is to harvest energy via strain-induced phenomena from both mechanical and thermal sources, and particularly sources neglected so far (slow and low). The main idea is the hybridization of different functional materials with the core of the system being screen printed piezo/pyro-electric microgenerators, mandatory to generate electrical charges. The originality of this work is to realize large area flexible energy harvesting systems by using ink-based piezoelectric copolymers of polyvinylidene fluoride P(VDF-TrFE). This material is very flexible and durable which makes it attractive for applications in systems with complex shapes. Another benefit of P(VDF-TrFE) is that it does not need to be pre-stretched as PVDF and it is now available in inks for printable electronics which can simplify and reduce the price of the fabrication process.

We first describe the fabrication process of the screen printed P(VDF-TrFE) microgenerators, followed by ferroelectric and piezoelectric characterizations. For this purpose we have developed optimized methods in open-circuit conditions adapted for flexible systems tested and validated on commercial bulk PVDF. The last step was to realize a low profile thermal flexible energy harvester prototype (no radiator). It was done by hybridization of the fabricated microgenerators and foils of shape memory NiTi-based alloy, which is a functional material sensitive to a given temperature threshold.

The key outcomes of this work are: 1) the successful deposition of multilayers of P(VDF-TrFE) and organic PEDOT:PSS electrode, 2) dielectric, ferroelectric and direct piezoelectric constants reported as a function of film thickness, and 3) the g_{31} direct voltage coefficient, measured for the first time, and showing the record value of 0.15 V·m/N. Also, we have demonstrated that in open-circuit conditions, the microgenerators can produce a useful strain-induced voltage of 10 V with an energy density close to 500 μJ/cm^3, these values being limited by the experimental set-up.

The concept of thermal energy harvesting composite based on thin film screen printed P(VDF-TrFE) microgenerators was realized and demonstrated to be effective. We conclude with a functional prototype of flexible energy harvester, able to detect non-continuous slow thermal events and producing 37 V (corresponding to 95 μJ) at 65 ºC.

Acknowledgements

I would like first to thank my wonderful supervisor team: Bernard Viala, Orphée Cugat and Leticia Gimeno. Thank you for guiding and encouraging me, showing opportunities and giving constructive critics.

There have been many people who helped me and worked side by side during these years. I would like to thank each and every one of them. I would especially like to thank Aurélia Plihon, who taught me a lot, Gor Lebedev and Dmitry Zakharov, whose example inspired me and put me on this road. And, of course, the girls from my office: Hélène Takacs, Jennifer Guillaume and Raissa Shema who helped me to settle in a new country and learn a new language.

Very big thanks must also go to my good friends Pasha Shpak and Ivan Voznyuk, which I met during this work and who shared the working life, joy and supported me at the most difficult times.

Finally, I would like to dedicate this work to my beloved husband Boris Gusarov, who is the Atlas which holds my World on his shoulders.

Contents

List of figures

List of tables

Chapter 1. Introduction and motivations

In the coming years the global climate and environment challenge will take a major role in our daily lives. The goal of reducing energy consumption and ecological footprint requires a multiplicity of solutions at different levels: from individual customer to major infrastructure and industrial systems. In the case of consumer products, there is a single source nowadays powering the very large number of low power electronic devices in our close environment: electrochemical, with disposable batteries. Tomorrow, commercial applications shall target alternative free energy sources found in nature which have been disregarded so far. They can be thermal, mechanical and electromagnetic. These "green" solutions (battery-less or plug-less to sector) are based on one or more of three separate main physical principles: the Peltier-Seebeck effect (also called thermoelectric effect), generating a constant electrical voltage with a fixed temperature gradient; the pyroelectric effect, producing an electric current with a temperature change; the direct piezoelectric effect consisting in generation of an electric voltage under the action of mechanical stress; and finally the inductive effect which creates an electric current through a conductor in the presence of a variable magnetic field.

The originality of our work is to realize flexible and large area (cm^2) energy harvesting systems by exploiting organic piezoelectric materials based on polyvinylidene fluoride (PVDF). This material is very flexible and durable which makes it attractive for applications in systems with complex shapes, for example in cases where the energy should be harvested from twisted cables or pipes, used in contact with skin or integrated in packaging of consumer products. In addition, PVDF and their copolymers are available in large sheets, opening perspectives to use it for large area electronics. These properties will allow systems with PVDF to benefit from high energy and power outputs, potentially superior to conventional solutions which use rigid piezoelectric materials such as ceramics.

Another benefit of PVDF and their copolymers is that they are becoming available in inks for printable electronics, which can simplify and reduce the cost of fabrication process.

Therefore, the objective of this work is to realize thin films based harvesters keeping large area as a target by means of screen printing methods.

1.1 Flexible electronics

In recent years flexible or printed electronics has received a great attention. It has a number of advantages over Si-based electronics. Among them are high flexibility and lightweight which can be critical for numerous applications, such as wearable electronics. Also, they can be transparent, which can be used in photovoltaic applications [1] and smart packaging, for food as an example. Another very important field of applications involves the interface with biology. Organic materials offer better mechanical compatibility with tissue than traditional electronic materials, and their flexibility suits the nonplanar form factors often required for implants [2]. Furthermore, flexible electronics have other advantages such as low-cost synthesis of material, and easy manufacture of thin film devices by printing technologies or vacuum evaporation/sublimation, or solution cast and large surfaces [3]. Furthermore it can be extended to "smart materials and systems" with new ink-based functional materials such as electroactive polymers for example.

Thus, the use of printed electronics gives the possibility to reach new functionalities and create new applications. For now, we can distinguish four main application families [4]:

- Displaying
- Lighting
- Sensing
- Powering

1.1.1 Printed electronics: usual techniques

An important strategy for design and fabrication of flexible electronics is to use solution-processable materials that can be directly printed and integrated into high-performance electronic components on plastic substrates. Motivations for using printed electronics include the potential economy with high-throughput printing methods and the compatibility of printing with roll-to-roll processing on large-area plastic or paper substrates [5].

Polymers are typically soluble in organic solvents and are often used for solution processing [6]. A variety of functional inks based on conductive, semiconducting and insulating polymer materials have been developed. Due to their low processing temperature it becomes possible to reduce the production costs by replacing Si substrates with low-cost flexible materials such as plastic, thin glass, and even paper. Also, printing processes provide efficient research and production platforms, such as PICTIC at CEA Liten, with high speed manufacturing, which makes them interesting for the industry [7]. To deposit organic thin-film layers, various printing techniques exist, each with their advantages and disadvantages. We will now briefly explain a few of the most promising techniques below.

Screen printing

Screen printing is one of the most used mass-printing techniques. A schematic representation of the screen printing process is shown on Figure 1.1.

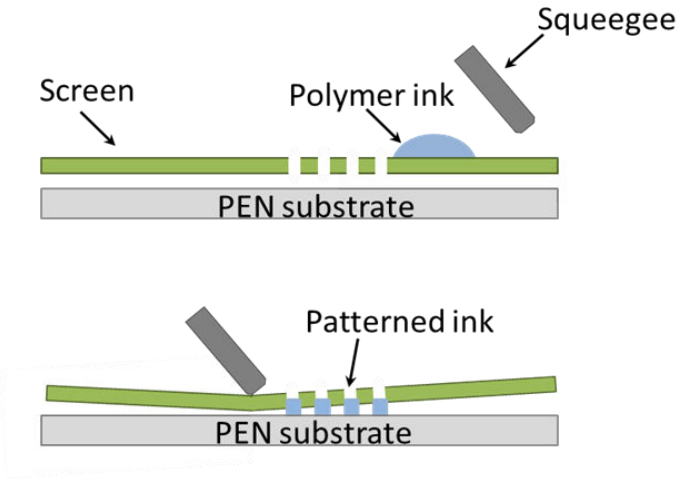

Figure 1.1. Schematic representation of the screen printing process.

During deposition, a screen with the pattern is placed above the surface of the substrate. The polymer ink is loaded onto the screen, which is then swept by a rubber ‘‘squeegee’’ with a certain velocity across the surface of the screen. At the point of contact, the solution flows through the screen patterns to the surface of the substrate. The material is thus transferred to the substrate, forming the desired pattern. The screen is typically made of a porous mesh, from materials such as a porous fabric, aluminum or stainless steel [8]. This process is very simple and cheap compared to other methods. The thickness of the deposited layer is dependent on the solution viscosity and velocity. This technique allows preparing

relatively thick layers (from one to several microns). The resolution is limited to 20-100 μm , similar to inkjet printing, and the printing speed is typically 2–3 m^2/s [6]. The main disadvantages of this technique are difficulties of producing thin and homogeneous layers, wasting of big quantity of material which stays on the screen during deposition, and high consumption of solvents for screen cleaning.

Gravure printing

Gravure printing is a transfer printing technique in which ink is carried from an ink fountain to a printing surface using an engraved gravure cylinder (Figure 1.2). This cylinder is covered with periodic cells filled with ink, and the excess is scraped off its surface using a blade. A printing substrate is placed between the rubber-covered impression cylinder and the gravure cylinder with ink. While the two cylinders are rotated, they pattern the ink onto a printing substrate. The use of gravure printing is attractive because of its high throughput, good control over the feature size, and flexibility in terms of the substrate selection. The temperature of the cylinder, ink and substrate can be controlled to optimize the printed features. The width and thickness of the pattern depend on the width and depth of the engravings in the mold, the printing speed, the ink viscosity, and the ink/substrate surface energies [7]. This is a mass-printing technique which is much more productive than other printing techniques, with a high throughput of 10–60 m^2/s [6].

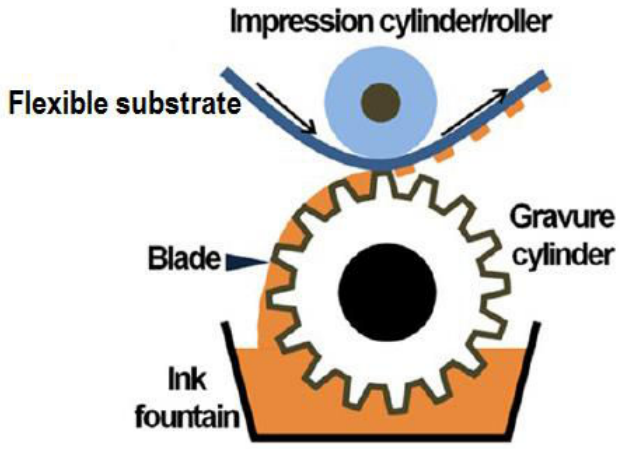

Figure 1.2. Schematic representation of the gravure printing process [7].

Inkjet printing

The inkjet printing process is a noncontact digital printing method. In this technique a nozzle is used to deposit small volumes (droplets) of the solution on different locations of the substrate, similar to a desktop printer [9], as shown on the Figure 1.3.

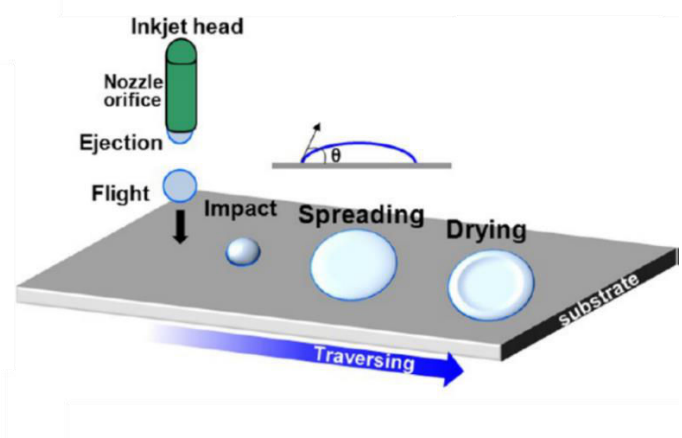

Figure 1.3. Schematic representation of the inkjet printing process [7].

The absence of mask or screen, which are used for other techniques, allows fast and easy changes to the desired design and avoid material waste (coating then etching for example). Inkjet printing is a relatively compact set-up, which makes it commonly used for the laboratory scale. The achievable resolution with conventional inkjet printing is 20-50 μm [6]. Solvent type, ink concentration and viscosity fine-tuning is required to control the shape, thickness and morphology of the droplet. The inkjet printing has some disadvantages compared to mass-printing technology – using a nozzle causes yield-limiting factor in terms of throughput (0.01–0.5 m^2/s) [6]. Moreover, film uniformity and homogeneity is also limited because of the drop-wise deposition of layers. Thus it makes this technique more suitable for the lab-scale manufacturing.

Conclusions

Here we have presented the most used printing methods for production of electronic components on plastic substrates. Their main characteristics in terms of solution viscosity, layer deposition thickness and throughput range are summarized in Table 1.1.

Table 1.1. Characteristics of the various printing techniques. Summarized from [6].

Printing techniques	Type of printing	Viscosity [Pas]	Thickness [μm]	Throughput [m^2/s]	Features
Inkjet	Direct write	0.001–0.04	0.01-20	0.01–0.5	Non-contact, small ink quantities, digital printing, low viscosity ink, slow speed
Screen	Direct write	0.5–50	0.015-100	2–3	Robust, simple, thick layer, large feature size, high ink viscosity, wasting of material
Gravure	Transfer	0.01–0.2	< 0.1–8	3–60	Fast printing, high resolution, relatively high plate cost, low dot gain

All described techniques are compatible with roll-to-roll (R2R) manufacturing. It is a commercial mass-printing process that combines different printing techniques for the fabrication of complete components and devices.

Here only the three most common methods are described, but a variety of different other printing method exists. Typically, the aim is to fabricate transparent and semi-transparent, bendable and even rollable flexible electronic devices such as organic light-emitting diode (OLED)-based displays [10], radio frequency identification (RFID) tags [11] and organic solar cells (OSCs) [12].

1.1.2 Printed electronics: the emblematic example of RFID

Internet links billions of “objets” globally, through computers and computerized devices and services of any size and capability and the applications running on them. The Internet of Things (IoT) is a new concept which can be considered as a giant future evolution of the Internet with including intelligent interconnections of various objects in the physical world, such as vehicles, cell phones, homes, and people [13]. To realize this interconnection each physical object needs to be connected via wireless RF nodes or equipped with RFID tags or other identification bar-codes that can be sensed by the smart sensor devices [14].

Back to printed electronics, RFID tags are the most relevant example of ultra large mass-fabrication of electronic flexible devices with ~ 7 billion tags produced in 2014 [15]. RFID systems (Figure 1.4) are composed of one or more readers and several RFID tags [16]. Each tag is characterized by a unique identifier. Readers trigger the tag transmission by generating an appropriate signal, which represents a query for the possible presence of tags in the surrounding area and for their IDs. Therefore they can be used in an incredibly wide range

of applications such as monitoring of objects in real-time, spanning from logistic to e-health and security [17].

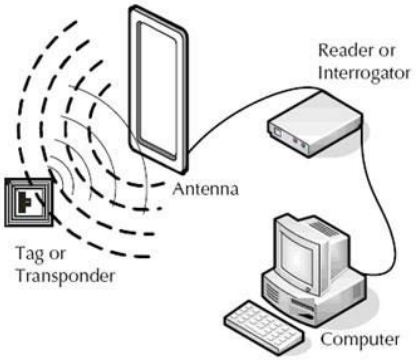

Figure 1.4. RFID system [18].

From a physical point of view, a RFID tag is a small microchip for wireless data transmission. It is generally attached to an antenna in a package that resembles an ordinary adhesive sticker (Figure 1.5). Modern RFID tags can reach size less than 0.1 mm^2 [17].

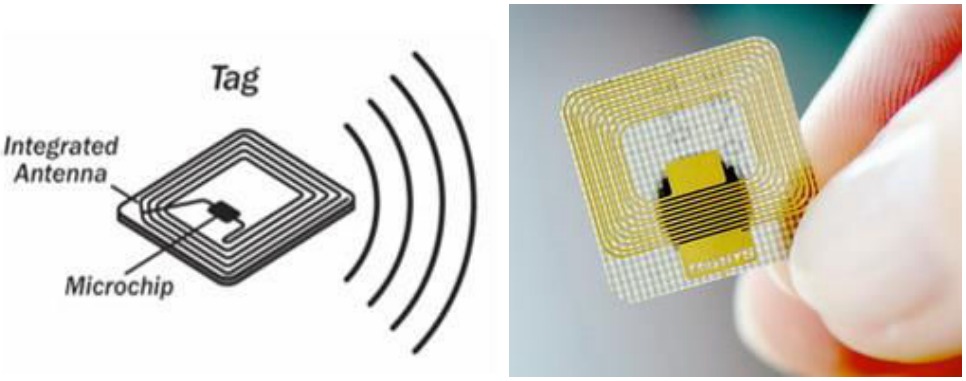

Figure 1.5. RFID tag [18].

Usually, RFID tags are passive, which means they do not have onboard power supplies and harvest the energy required for transmitting their ID from the query signal transmitted by a RFID reader in the proximity. In fact, this signal generates a current into the tag antenna by induction and this current is utilized to supply the microchip which will transmit the tag ID. Usually, the efficiency of this power conversion is very low [17]. The operational range of RFID tag is also low, typically 10-50 cm [19]. RFID tags can be also powered by batteries, but in this case batteries need to be regularly changed.

Silicon RFID tags however, are still not yet suitable to tag individual goods as envisioned by the IoT. Tagging individual items that may be thrown away after use requires the tag to cost only a few euro cents. Although the cost of a silicon microchip is not an issue and even continues to decrease by scaling, the need to make an external connection between the microchip with the antenna and possibly with sensors puts a lower limit to the total cost of the tag [25]. In addition, these connections are subjected to mechanical failure if the goods are handled harshly during transport [24]. A route to solve both problems could be to fabricate the entire tag, chip with antenna and sensors, on the same, flexible substrate using thin-film technology [9].

1.1.3 Printed electronics: flexible and transparent electrodes

In all cases, IoT massive deployment will benefit from highly flexible, conformable, foldable or wearable materials. In particular, compliant electrodes and interconnections are one of the key elements in realizing next-generation of highly flexible electronics [20]. Indeed, modern applications are expected to emerge in our daily life, for instance sensors printed on goods, electronic newspapers, and wearable electronic devices and displays [21]. Many of those forthcoming applications require low-cost production and special electrodes. These electrodes need to have a series of characteristics, such as superior flexibility, transparency, high conductivity, long term stability etc.

Promising candidates for electrodes are conducting polymers, among which great attention is given to PEDOT or poly(3,4-ethylenedioxythiophene), which was developed in 1980s at Bayer AG research laboratories in Germany [22]. Its backbone structure is shown on the Figure 1.6.

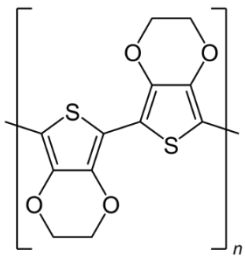

Figure 1.6. The backbone structure of PEDOT.

PEDOT has high conductivity (~300 S/cm), good stability in the oxidized state and transparency [23]. But it has a large disadvantage which is poor solubility.

PEDOT low solubility problem was solved with further research by mixing it with water-soluble poly(styrene sulfonate) (PSS). The resulting combination of PEDOT:PSS yielded in a water-soluble system with good film-forming properties, high conductivity (~ 10 S/cm), high visible light transmissivity, and excellent stability. Figure 1.7 shows the backbone structure of PEDOT:PSS. Films of PEDOT:PSS can be heated in air at 100^{o}C for over 1000 h with only a minimal change in conductivity [23].

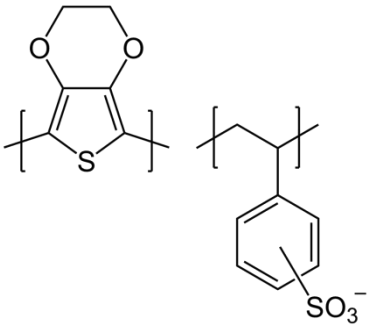

Figure 1.7. The backbone structure of PEDOT:PSS.

Thanks to combination of good conductive properties and transparency, PEDOT:PSS is widely used for solar cells as electrode material [24]–[26].

1.2 Energy harvesting: towards flexibility

Our closest world is surrounded by a variety of disregarded energy sources. So far, mankind actively uses fossil energies and nuclear power, completed by solar, wind and water energies. But we can imagine and find the way on how to use new minor sources of energy. One of the possibilities is energy harvesting, which is a process of capture, conversion, use and storage of useful electrical energy from alternative external sources. Energy harvesting is a new option to dispense with electric power sector or disposal batteries. It is aimed to replace conventional power supplies for low power consumer electronics and embedded systems and thus produce self-powered devices. Below, to give ideas of this concept we present some examples of important works dedicated to this topic, and using simple common piezoelectric materials. The focus is on flexible systems.

In 1996 Starner showed a theoretical estimation and comparison of power generation for a wearable computer by using everyday actions such as leg motion, breath, blood pressure etc. (Figure 1.8). He demonstrated that by using piezoelectric (see 1.2.1) shoe inserts it is possible to generate 5 W of electrical power in the process of walking [27].

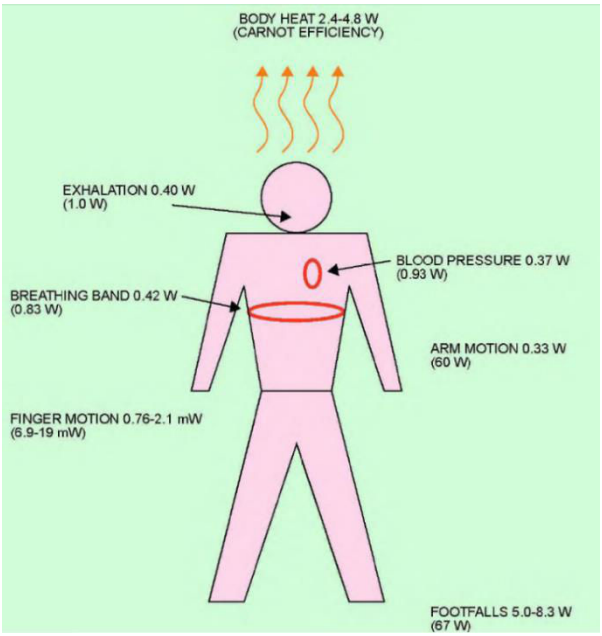

Figure 1.8. Power from body-driven sources; total power for each action is included in parentheses [27].

Guigon et al. [28] produced a system for harvesting energy from rain with a piezoelectric flexible structure (Figure 1.9). In this study a syringe pump was used to create identical drops which fall from a height of 3.5 cm into 25 µm PVDF piezoelectric polymer surface. After impact the observed voltage peak was almost 3 V. The work also demonstrated good correlation between theoretical and experimental results.

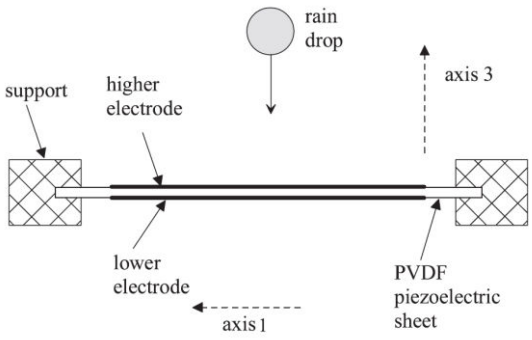

Figure 1.9. System of raindrop energy harvesting from [28].

In 2011 S. Takamatsu et al. [29] built an all-polymer energy harvesting device for low frequency applications consisting of a PET polymer substrate, PEDOT:PSS conductive polymer electrode, PVDF piezoelectric film. To deposit the PVDF film on PET substrate, authors developed a low temperature coating process using low boiling temperature solvent (Methyl ethyl ketone) and annealing under 150 ˚C. To induce strain on the PVDF layer, the whole structure was bent with a known radius as shown on Figure 1.10. The strain-generated electric potential of 2 V was demonstrated. However, the thickness of the PVDF layer and strain values were not reported.

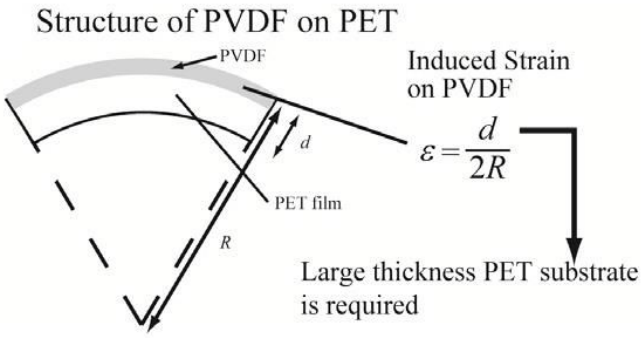

Figure 1.10. Strain generation by bending of all-polymer piezoelectric energy harvesting device [29].

In 2013 G. Canavese et al. [30] reported work with the direct and converse piezoelectric characterization of three P(VDF-TrFE) structures for flexible tactile sensors and bendable energy harvesters. In order to test the piezoelectric effect in direct mode, they reproduced the raindrop experiment. Water drops delivered by a syringe pump impacted the surface of the piezoelectric polymer structures, thus producing a compressive deformation and generating an impulse of charges. Authors have reported producing up to 9 V with a single drop. However, thickness of PVDF layer that was used to produce this voltage was not mentioned.

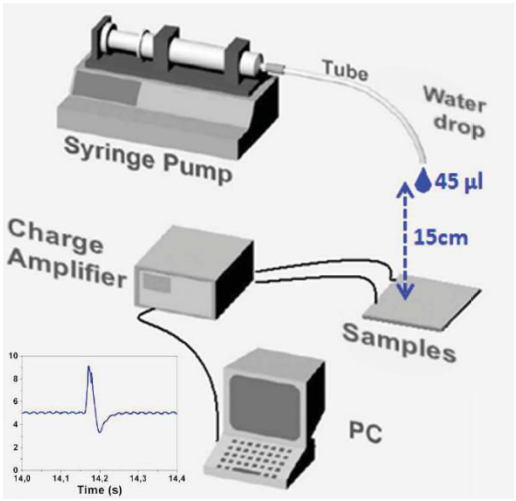

Figure 1.11. Scheme of the experimental set-up used to investigate the direct piezoelectric response of the P(VDF-TrFE) samples [30].

In the same year Lee et al. [31] showed a first fully stretchable and flexible device based on a piezoelectric copolymer P(VDF-TrFE) thin film for harvesting mechanical and thermal energy from human body (Figure 1.12). To realize this they used a PDMS/CNT composite and graphene as electrodes. The total produced voltage from both piezoelectric and pyroelectric effects was measured to be 1.4 V. Device demonstrated stable output potential even after 30% of applied strain. Unfortunately, the temperature and strain were not provided.

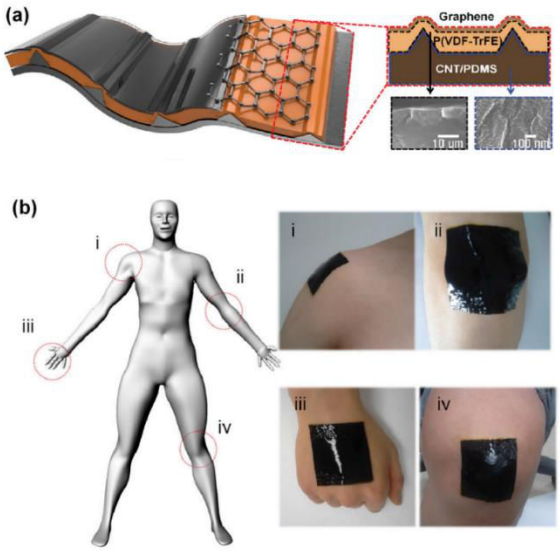

Figure 1.12. (a) Schematic illustration of the flexible nanogenerator, (b) photo images of the nanogenerator at various location on human body, showing good compatibility of the device with various parts of body [31].

More recently, in 2014 Z. Pi et al. [32] fabricated flexible nano- and microgenerators based on direct piezoelectric effect using a spin-coated P(VDF-TrFE) thin film as functional layer on a polyimide substrate. To characterize the performance of these generators the electrical output under applied mechanical strain was measured. Samples were bent using mechanical loading equipment (Figure 1.13) reaching a strain magnitude of 0.9%. The resulting open-circuit voltage detected at a loading frequency f = 0.5 Hz was equal to ~7 V for films of 6.5 µm. As authors mentioned, this value of voltage output is higher than typically achieved in other flexible piezoelectric nanogenerators. Based on the provided values and taking into account the typical value of P(VDF-TrFE) Young's modulus (1.5 GPa) we can estimate piezoelectric g_{31} coefficient to be 0.08 V·m/N.

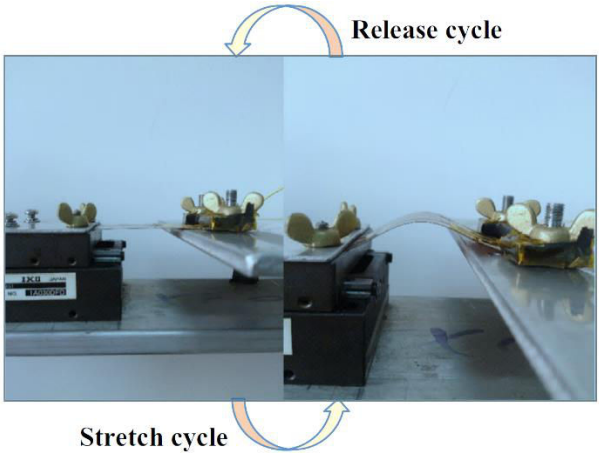

Figure 1.13. Stretch and release cycles scheme of mechanical loading equipment.

All the above mentioned examples are based on the direct piezoelectric effect. The piezoelectric coefficients are used to compare piezoelectric performants of different materials. We will now introduce piezoelectricity and the different piezoelectric coefficients.

1.2.1 Introduction to piezoelectricity and pyroelectricity

As we have just seen, piezoelectric materials have the unique ability to produce electrical voltage under applied mechanical strain or force (direct piezoelectric effect). Similarly, the application of a voltage across the material will cause strain (converse piezoelectric effect). Due to these characteristics, piezoelectric materials are widely used for different applications such as ignition systems, audio buzzers, actuators and sensing

applications. Today a number of developers try to use these materials for harvesting energy produced by vibrations, motion from human body, raindrop energy etc.

Piezoelectricity

Piezoelectricity is characterized with proportionality coefficients between mechanical and electrical values. Since piezo materials are anisotropic, these coefficients are determined for each direction of the element and indexed X_{ij}, with i corresponding to the direction of the electrical measurement, and j corresponding to the direction of the mechanical force. The axes of the material are numbered from 1 to 3 (Figure 1.14). The direction of polarization usually is made to coincide with the 3-axis.

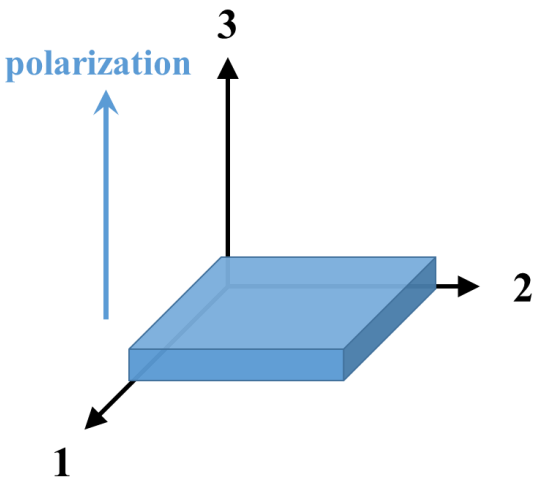

Figure 1.14. Axes definition of piezo elements.

The most frequently used physical constants to characterize piezoelectric material are:

- d_{ij} the piezoelectric charge constant;
- g_{ij} the piezoelectric voltage constant;
- k_{ij} the electromechanical coupling factor;
- ε_{ij} the dielectric permittivity.

The d_{ij} coefficient is obtained by measuring the electrical charge density, which is created at the surface of the film by mechanical stress applied to a piezoelectric material. The value is given in C/N. It also gives the mechanical strain experienced by a piezoelectric material when an electrical field is applied. This coefficient is usually used to characterize piezoelectric material for actuator applications.

In turn, the g_{ij} coefficient indicates the electrical field generated when the mechanical stress is applied along the j axis. It is measured in V·m/N. This coefficient is less known than d_{ij} than but is essential for piezoelectric generators. The g coefficients are usually calculated from d coefficients by:

$$g_{ij} = \frac{d_{ij}}{\varepsilon} \tag{1.1}$$

In this work we want to characterize and compare the piezoelectric materials for energy harvesting applications. Thus the knowledge of g_{ij} is capital. We will describe later our proper measurement techniques to achieve direct estimations of g_{ij}.

With these coefficients, it is possible to estimate the theoretical voltage output of a piezoelectric material, using the piezoelectric coupling matrix [33]. The fundamental matrix of interactions is written in the following form:

$$\begin{cases} S_{ij} = s_{ij}^{E} \cdot \mathrm{T} + d_{ij} \cdot \mathrm{E} \\ \mathrm{D} = d_{ij} \cdot \mathrm{T} + \varepsilon_{ij}^{T} \cdot \mathrm{E} \end{cases} \tag{1.2}$$

where D is the electric displacement field, E is the electric field, T is the mechanical stress, S is the mechanical strain, s is the flexibility [Pa-1 or m2N-1], d is the piezoelectric coefficient [C/N or m/V], g is the piezoelectric voltage coefficient [V·m/N or m2/C], and h is the piezoelectric coefficient [N/C or V/m].

In the case where the sample is mechanically free (T is constant) and it is connected to an open electrical circuit (D is constant), the matrix can be written in the following form:

$$\begin{cases} S = s^{D} \cdot T + {g_{ij}}^{t} \cdot D \\ E = -g_{ij} \cdot T + \beta^{T} \cdot D \end{cases} \tag{1.3}$$

In this case s^{D} is the compliance, equal to inverse Young's modulus of the material, $\beta^{T} = (\varepsilon^{T})^{-1}$ is the permeability constant under constant T and g^{T} is a transposed matrix of g. Under the experimental conditions of an open circuit D is equal to zero, so the matrix can be simplified:

$$\begin{cases} S = s^D T \\ E = -g_{ij} T \end{cases} \tag{1.4}$$

From equation (1.4) we can see that the voltage output of the piezoelectric is determined by the material's thickness, its piezoelectric constant g, and the applied stress:

$$V = -g_{ij} \cdot T \cdot t \tag{1.5}$$

where t is the sample thickness.

From the point of view of the sample geometry, it can be noted that this voltage should be independent on the sample length and width, considering that equivalent stress is applied, and should only be dependent on the thickness.

The equation (1.5) can be then rewritten as a function of material strain:

$$V = -g_{ij} \cdot S \cdot YM \cdot t \tag{1.6}$$

where YM is the Young's modulus of the material.

The latter analytical equation is valid in such experimental conditions, where the electrical displacement field and the stress are constant.

Pyroelectricity

Pyroelectricity is a subclass of piezoelectricity. These materials are able to produce electric voltage under temporal temperature changes. They are characterized by a pyroelectric coefficient p_i, which shows changes in the spontaneous polarization vector with temperature:

$$p_i = \frac{\partial P_{S,i}}{\partial T} \tag{1.7}$$

where p_i [C /m^2 K] is the vector of pyroelectric coefficients

Pyroelectric properties of materials are commonly used for infrared thermal imaging and non-contact infrared temperature sensors. Such materials can work as pyroelectric generators as well when a constant thermal source is present. They can be used also for

multimodal energy harvesting application in combination with piezoelectric properties, to collect not only mechanical, but also thermal energy, as proposed by our group [34].

The most common pyroelectric (also piezoelectric) materials are polycrystalline ferroelectric ceramics such as barium titanate ($BaTiO_3$) and lead zirconate titanate (PZT), as they have the strongest piezoelectric effect. Recently great attention has been given to piezoelectric polymers, which have obvious advantages in mechanical properties (compared to brittle ceramics) and, as was mentioned previously, are compatible with printing technologies.

Therefore, with the aim to develop fully-flexible pyro/piezoelectric multimodal harvesters in this work, the state of the art of piezoelectric polymers will be introduced now.

1.2.2 Piezoelectric polymers: state of the art

In 1969 Kawai discovered that some polymers, especially polyvinylidene fluoride (PVDF) exhibit a strong piezoelectric effect [35]. PVDF is a semi-crystalline material – it has some crystalline phase regions surrounded by amorphous regions. PVDF has four main crystalline phases known as phase I (β), phase II (α), phase III (γ), and phase IV (δ). The relative quantity of each is dependent on the thermal, mechanical and electrical processing conditions used to produce the PVDF film. The most general form is non-polar α-phase which does not have any piezoelectric properties. Only highly oriented β-phase is responsible for the piezo- and pyro-electric properties of the polymer [36]. It was shown that α-phase can be converted to β by subjection to mechanical stretching [37],[38] (Figure 1.15).

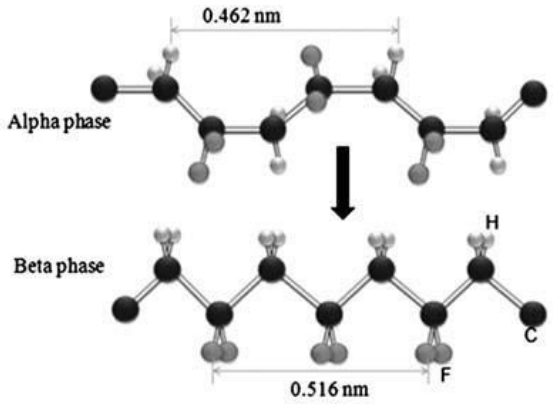

Figure 1.15. Schematic presentation of the transformation in PVDF from α to β-phase. [39].

In order to obtain piezoelectric properties, the β-phase needs to be poled. It consists of applying high electric field to the film in order to orient the molecular dipoles in the same direction. This induces a spatial organization of the macromolecular chain segments [38]. Combination of stretching and polarization provides molecular chain alignment perpendicular to the electric field (dipoles are aligned perpendicular to the chain so parallel to the applied field).

With recent studies, a PVDF copolymer - poly(vinylidene fluoride-trifluoroethylene) (P(VDF-TrFE)) - has attracted great attention. The addition of TrFE into the PVDF system plays an important role in the phase transition behavior. Because of the size of the additional fluorine atom, the copolymer will crystallize directly in beta phase. Thus, no additional stretching is needed, and this copolymer can be directly used to produce final structures from the solution [38]. The copolymer crystal structure, phase transition behavior and ferroelectric properties are affected by the ratio of VDF/TrFE content and the synthesis conditions [40].

Also, other polymer systems based on modification of the P(VDF–TrFE) exist. Among them great attention has been paid to poly(vinylidene-fluoride–trifluoroethylene–chlorotrifluoroethylene) terpolymer (PVDF–TrFE–CTFE). It was shown that the introduction of CTFE into the P(VDF–TrFE) copolymer converts the normal ferroelectric P(VDF–TrFE) into a ferroelectric relaxor with high electrostrictive strain. This material is known to have relaxor properties with a low hysteresis and high dielectric permittivity at ambient temperature [41], [42].

The polymer properties are very different from those of conventional ceramics. In Table 1.2 different polymer and ceramic piezoelectric materials are compared. For piezoelectric generator applications, it is important to compare the g_{ij} voltage coefficient, and not the d_{ij} coefficient which is used for actuators. For energy harvesting, there is a more complete figure of merit (FOM). It was originally proposed in [43] for vibration energy harvesting applications and used in [44] with the 3-1 piezoelectric mode. The FOM is defined as:

$$FOM = \frac{d_{31} g_{31}}{\tan \delta} = \frac{d_{31}^2}{\varepsilon_{33} \tan \delta} \tag{1.8}$$

where g_{31}, d_{31} – piezoelectric constants, ε_{33} – relative permittivity and tan δ – loss tangent.

Our case is different because it is purely static (or very low frequency), with the goal of harvesting a temperature change. Therefore, one can assume that $\tan\delta$ is unity and the FOM simplifies to:

$$FOM = d_{31}g_{31} \tag{1.9}$$

Table 1.2. Comparison table of different polymer and ceramic piezoelectric materials.

Property	Units	PVDF	P(VDF-TrFE)	PMN-PT	PZT	$BaTiO_3$	AlN
Density	10^3 kg/m^3	1.78	1.82	8.3	7.5	5.7	3.3
ε_{33}	-	12	9.4	4200	1200	1700	10
d_{31}	10^{-12} C/N	23	6	-930	-110	-78	-2.6
g_{31}	10^{-3} V·m/N	192	64	-22	-9	-5	-26
$d_{31}g_{31}$	-	4416	384	20460	990	390	68
k_{31}	%	0.12	0.2	0.5	0.59	0.3	0.2
Young's modulus	GPa	3	1.5	15	69	67	320

Based on Table 1.2, the materials can be classified in the following order for generator and harvesting applications, respectively:

- according to g_{31}: PVDF, P(VDF-TrFE), AlN, PMN-PT, PZT and BTO
- according to $d_{31}g_{31}$: PMN-PT, PVDF, PZT, P(VDF-TrFE), BTO and AlN

If we now add to the discussion the fact that flexibility and maximum strain are decisive criteria, PVDF undoubtedly ranks at the 1st place and P(VDF-TrFE) at the 2nd one. Polymers can be deformed up to 20-30%, whereas conventional ceramic materials can only withstand up to 0.1% of strain. This gives undeniable benefits to PVDF and P(VDF-TrFE) for flexible piezoelectric harvesters, when large deformations can be exploited for the applications.

To enlighten this point, we calculated the theoretical voltage output as a function of strain according to equation (1.6) for a selection of piezoelectric materials. The results are shown on Figure 1.16.

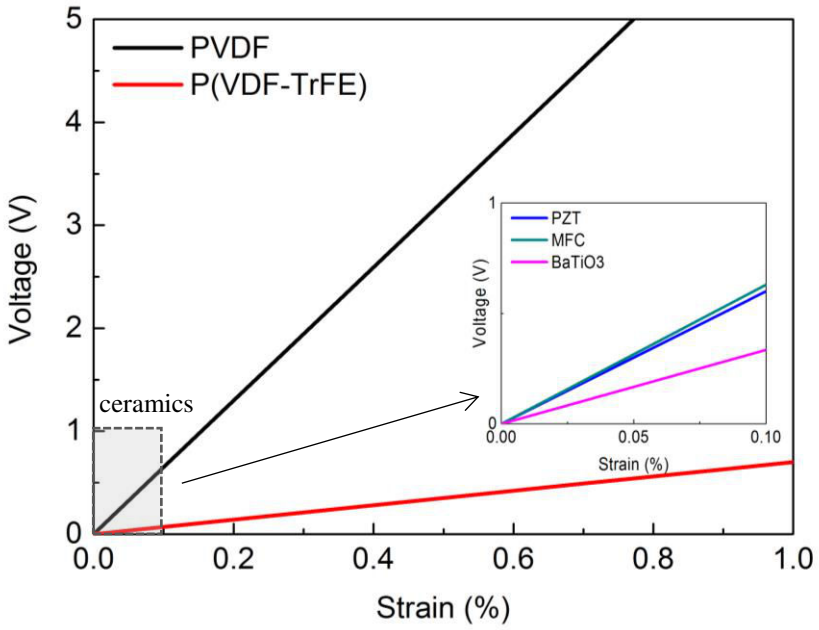

Figure 1.16. Theoretical absolute voltage output as function of applied strain for different piezoelectric materials for 1 μm thickness.

Finally, knowing that P(VDF-TrFE) is more appropriate than PVDF for thin film integration, because it does not need to be stretched, it is indeed the best candidate for the realization of flexible thin film piezoelectric harvesters. In addition, research is focused on techniques to improve P(VDF-TrFE) piezoelectric properties. One of them is nanostructuration.

1.2.3 Piezoelectric polymers: nanostructuration

Since piezoelectric properties of PVDF and its copolymers directly depend on the β-phase, it is a big challenge for researchers to find a way to increase its content in the polymer material. An even more challenging goal is to control properties at a local scale which can be critical for various nanoscale devices such as nanosensors, non-volatile memories and nanogenerators. There are some works that show that confining these materials with nanostructures allows better control of polymer crystallization in the piezoelectric β-phase and in some circumstances orienting these crystallites. Indeed, crystal nucleation is strongly

affected by confining polymer melts into small volumes; the mechanisms involved can be either the exclusion of heterogeneous nuclei or preferential interaction of chains with interfaces [45]. It is therefore possible to control polymer crystallization and increase the content of a particular crystalline phase by nanostructuration depending on the processing conditions. Such nanostructures may also have great potential for high energy density storage applications due to the dramatically increased surface areas over the thin film structure [46]. Different techniques have been applied to produce or pattern organic ferroelectric micro- and nanostructures, including nanoimprint lithography (NIL) [45], [47]–[50], using for example an anodized alumina membrane as a shaping mold [30], [46] or conventional direct drawing (e.g. electrospinning) [51], [52]. Among them, thermal nanoimprint lithography is dominant. It is especially attractive with thermoplastic polymers as a rapid and low-cost technique for the preparation of polymer structures on large areas with feature sizes down to 10 nm [53]. In this technique micro- and nanostructuration is created by the mechanical deformation of a molten polymer film by means of pressing with a hard mold (typically from Si) (Figure 1.17).

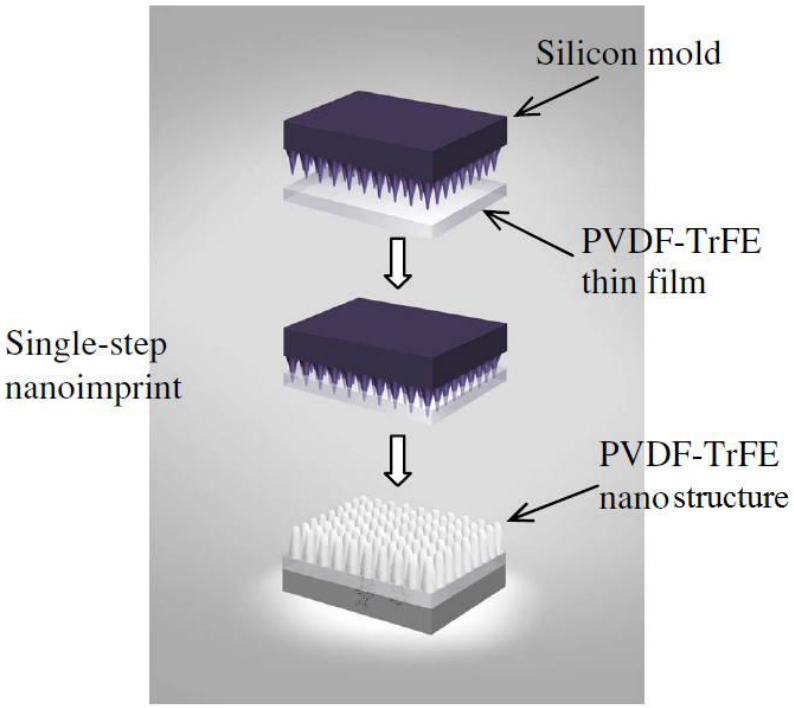

Figure 1.17. Schematic drawing of the nanoimprint process of PVDF-TrFE polymer. [50].

The process takes place under vacuum, to avoid air being trapped between sample and mold. The sample is first heated close to the melting point temperature (step 1 and 2 in Figure

1.18). The mold is then pressed to it with a constant pressure of typically 40 bars for several minutes (step 5), while the temperature is decreased (step 3). Once temperature reaches a certain low point, the pressure is released (step 4). The sample is then dissociated of the mold (demolding).

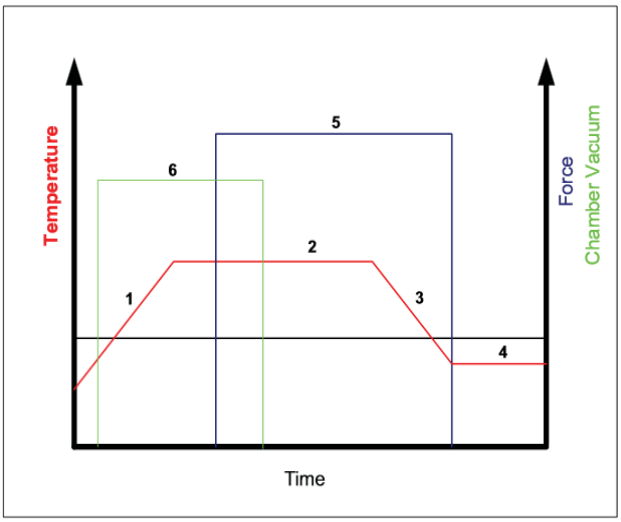

Figure 1.18. Nanoimprint process steps.

The reader may find a more complete state of art of NIL and details about thermo-nanoimprint as used in this work in Cécile Gourgon's article [54], the person who was actively involved in this work at CNRS-LTM.

Because of its potential, this is an exploratory route we will take later in this manuscript. Films of P(VDF-TrFE) will be nanoimprinted in form of fibers after screen printing deposition on interdigital electrodes. The nanoimprint geometry is an inspiration from the structure of MFC macro fiber piezo-ceramic composites which are semi-flexible materials from Smart Material Corp. [55]. The use of such semi flexible piezoelectric materials in our group [34], [56], [57] opened the route of smart composites for energy harvesting that we keep following here towards fully flexible systems.

Thus, next section is a short introduction to composites for energy harvesting with the aim of using fully flexible piezoelectric polymers instead.

1.2.4 Piezoelectric polymers: composites with shape memory alloy

Among the different energy sources, thermal sources are widely available. Usually, thermal energy can be directly converted into electricity by means of thermoelectric [58] (Seebeck effect) or pyroelectric [59] materials. Thermoelectric power generators have already been demonstrated. However, such devices require large spatial temperature gradients with cold source management in order to be efficient. Recently, another concept of thermal-to-electric energy conversion was demonstrated and experimentally approved by our group. It consisted in using hybrid composite structures of semi-flexible ceramic piezoelectric material coupled with shape memory alloy (SMA) [57]. Such coupling aimed on harvesting slow and small temperature variations around a particular temperature threshold which determined by the composition of the alloy.

Numerous metallic alloys exhibit a shape memory effect (SME). Fundamental to this effect is the occurrence of martensitic phase transformation and its subsequent reversal. Basically, a shape memory alloy is deformed in the martensitic phase, and the shape recovery occurs during heating when the alloy undergoes a reverse transformation from martensite to austenite [60]. Both direct and reverse transformations occur within some temperature interval and are characterized by start and finish temperatures. In addition, thermodynamically conditioned thermal hysteresis prevents these temperature intervals from coinciding (Figure 1.19). As a result of this transformation, SMA develops large stress and strain at heating (up to 600 MPa and 10% for NiTi alloy [61]), which can be converted to electrical energy by coupling it with a piezoelectric material, with the mechanical-to-electrical efficiency characterized by coupling coefficient k^2.

Since SMAs are able to produce high values of stress (a realistic value is of ~ 4%), it is important to use highly flexible piezoelectric materials which can withstand such high levels of deformation. The combination of both materials can be used for flexible energy harvesting systems. During this work we have realized an energy harvesting prototype by hybridization P(VDF-TrFE) copolymer generators with NiTi-based SMA.

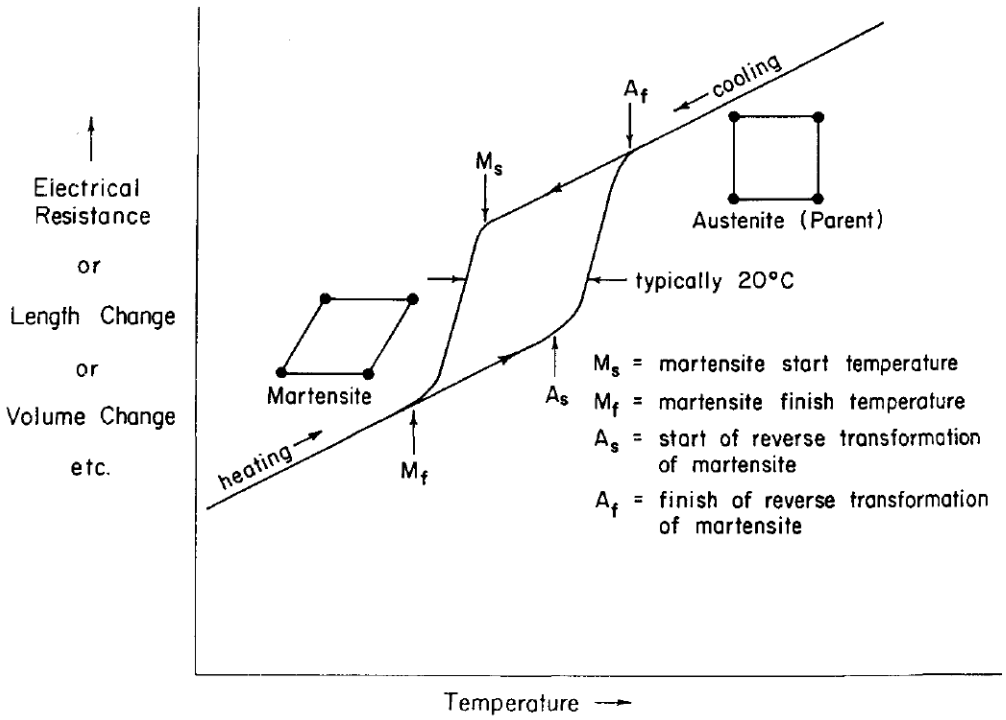

Figure 1.19. Property change vs. temperature for a martensitic transformation occurring in a shape memory alloy. The parent phase (austenite) is represented by the square lattice, which upon martensitic transformation is distorted into the rhombic martensite phase [60].

1.3 Summary of the targets of this work

The main objective of this work is to demonstrate a functional proof of concept of a flexible thermal smart composite structure able to detect and harvest non-continuous or slow and low thermal events. Here we aimed at hybridizing new screen printed P(VDF-TrFE) piezoelectric microgenerators and existing foils of NiTi-based SMA.

We have seen different approaches of energy harvesting using piezoelectric flexible materials. This is a growing field with many possible commercial applications. Using polymers allows new functionalities where high strain and lightweight are necessary. P(VDF-TrFE) copolymer is the best suitable piezoelectric polymer for screen printing deposition and integration, and it is well adapted for such applications. Moreover, it is possible to further enhance their properties by techniques such as nanoimprint lithography.

In this work we have decided to use new formulated inks of P(VDF-TrFE) for screen printing in collaboration with Liten/Arkema. It was a real challenge initially to fabricate new

efficient flexible piezoelectric microgenerators on plastic substrates. The second challenge was to evaluate under realistic conditions the energy harvesting capabilities of such microgenerators by measuring first the piezoelectric voltage and energy without parasitic losses.

The ultimate target was to produce a functional proof of concept of a fully flexible harvester able to detect non-continuous or slow and low thermal events, which will eventually be events such as small temperature changes in ambient air or due to skin contact. Also, establishing the building blocks to further allow realizing a complete thermal autonomous wireless sensors was in the scope of this work. That is why directions of improvement were part of the final objectives including materials, power management circuit and wireless transmission at the end.

Chapter 2. Fabrication process for flexible piezoelectric microgenerators

This chapter presents the materials and methods used to prepare the samples of this study. The full fabrication process flow of the flexible piezoelectric microgenerators is detailed. The experimental work is mainly based on the copolymer of PVDF. The key outcome of this section is the deposition of multilayers of ink-based P(VDF-TrFE) by screen printing. Following the chronology and the progress of the deposition work, we start with a simple single capacitor structure and continue with the design and fabrication of parallel connected capacitors network featuring a credit card format for demonstration. Moreover, to have a broader vision, an exploratory work has been engaged with new inks of terpolymer P(VDF-TrFE-CTFE). This material is known to have relaxor properties with a low hysteresis and high dielectric permittivity at ambient temperature [41], [42]. In particular, original heterostructures of P(VDF-TrFE) and P(VDF-TrFE-CTFE) are realized for the first time. Also, different electrode materials (silver, gold and PEDOT:PSS) are compared to see how they affect the morphology quality of the deposited piezoelectric films.

2.1 Materials and methods

2.1.1 Sample fabrication: overall process flow

In our work the sample fabrication is facing two challenges. One is to develop upstream technological steps and the other is to propose a process flow that meets the needs of industry at the end. That is why the sample fabrication was conducted on the PICTIC platform of Liten which is dedicated to industrial transfer of new printed technologies.

PICTIC has world class research facilities for flexible electronics with 400 m^2 class 10'000 clean room (Figure 2.1). It has various equipments for material fabrication and characterization, including an automatic screen printer.

Figure 2.1. The clean room of the PICTIC platform in Liten.

We will now describe the overall process flow of screen printed sample fabrication (schematically presented in Figure 2.2).

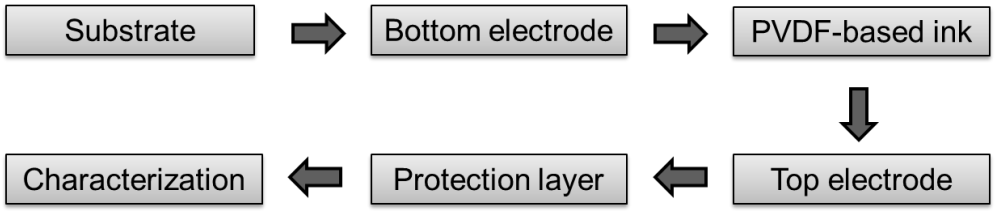

Figure 2.2. The overall process flow of sample fabrication.

First 30 nm Au bottom electrodes were deposited on the 125 µm thick flexible organic substrate by using an Alcatel SCM600 physical vapor deposition (PVD) unit. A shadow mask was used for patterning.

Co- and terpolymer layers were deposited from inks by screen printing technique. The total thicknesses varied from 1.1 to 3.9 µm depending on the number of layers deposited. Then, samples were dried for 3 minutes at 60 ^{o}C on a hot plate, and then 10 minutes in an infrared oven at 120 ^{o}C for terpolymers and at 130 ^{o}C for copolymers. These temperatures and

times satisfy conditions for solvent-removal and crystallization of the piezoelectric β-phase of P(VDF-TrFE) [62]. The first annealing step at 60 ^{o}C was introduced to decrease thermal shock to samples. Without this preliminary annealing we have observed formation of cracks in the P(VDF-TrFE) layer (Figure 2.3).

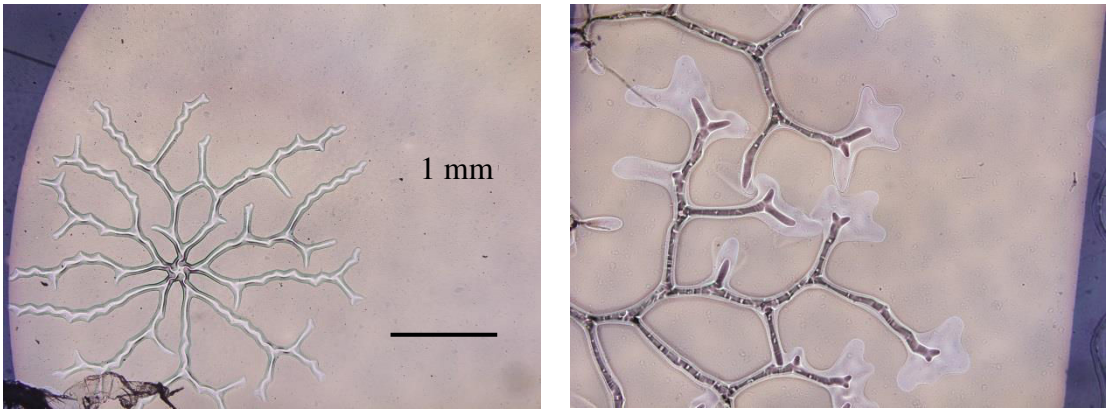

Figure 2.3. Cracks on the 2.6 μm screen printed P(VDF-TrFE) samples without preliminary annealing.

The next step was top electrode deposition by screen printing. Two different materials were used for electrodes: Ag paste (5 μm) or PEDOT:PSS (400 nm). After the deposition, the electrodes were dried the same way as PVDF-based layers.

The last step was the encapsulation of samples with PEDOT:PSS top electrodes. They were covered by a 1 μm protective organic coating using screen printing. This layer is needed to protect PEDOT:PSS as it very sensitive to humidity [63], [64], [65] and keep it on the operating conditions for a long time.

Substrate and its characteristics

A variety of foils are being considered to be used as substrates for flexible electronics taking into consideration their thermal, mechanical and optical properties along with the requirements arising from the various manufacturing processes and operation conditions of the final applications. In general, two classes of substrates are considered: plastic foils and thin metal foils. Thin polymeric foils are extremely attractive for several reasons. First, because they can be made lightweight and inexpensive making it possible to target high-volume and low-cost commercial products. Secondly, processing of these materials being usually carried out at temperatures below 180–120 °C makes them particularly attractive for organic technology based on low-temperature printing or evaporation techniques [66].

Secondly, they can be made transparent: an essential prerequisite for applications where light has to either enter (e.g. photovoltaics and photodetection) or exit (displays, lighting) the device. Finally, these polymer foils inherently enable a high degree of mechanical flexibility and conformability [67].

Polyethylene terephthalate (PET) and polyethylene naphthalate (PEN) constitute the two main transparent flexible substrates used today in the development of flexible electronics. Not only they provide good resistance to solvents and a discrete tolerance to temperature, but also their intrinsic transparency makes them suitable as substrates for transparent electronics [66].

In Table 2.1 properties commercial PEN and PET organic substrates from Teijin DuPont Films are compared.

Table 2.1. Properties comparison of PEN and PET flexible substrates [68]

Property	Unit	PEN	PET
Tensile strength	MPa	280	230
Tensile elongation	%	90	120
Continuous use temperature (mechanical)	°C	160	105
Continuous use temperature (electrical)	°C	180	105
Glass transition temperature (film)	°C	155	110
Melting point	°C	269	258
Dielectric breakdown voltage	kV/mm	300	280
Dielectric constant	-	2.9	3.1
Water absorption	%	0.3	0.4
Density	g/cm^3	1.36	1.40

Based on low tensile strength and high tensile elongation both substrates can be used for flexible electronics. Since for our fabrication we use thermal treatment up to 130 °C, we have chosen PEN, as it has higher working temperature (160-180 °C).

Bottom electrode

With a piezoelectric film at least the bottom electrode is required to polarize first, then to actuate or pick up strain-induced generated voltage. Usually, the bottom electrode is realized directly onto the substrate for ease of fabrication. Classically, it is made with gold

metallization. Gold is suitable because it allows using very thin conductive electrodes and is semi-compliant. Low thickness is an important prerequisite for a suitable deposition of the piezoelectric film afterwards. Indeed, a thick electrode may create a topology below which is difficult to cover without defects such as incomplete step coverage, lateral cracks, residual stress etc.

For this reason, we routinely used 30 nm Au bottom electrodes deposited on PEN substrate by using PVD with shadow mask. It consists of a plurality of electrode designs which are not all useful, but some are generic including standardized lines and pads for tests (with connectors or tips).

When high compliance is an issue, carbon-based electrodes may be used [20], [31]. When transparency is another requirement, optically transparent indium tin oxide (ITO) electrodes can be used instead. However for highly flexible applications such as smart skin or wearable sensors recent conductive polymers can be preferred.

Piezoelectric material

Prior to screen printing of the piezoelectric layer, a necessary step is the formulation of its ink. Here, it is made of a 15 wt% cyclopentanone solution of P(VDF-TrFE) with a VDF:TrFE ratio of 75:25 wt%. It was prepared by mixing with a magnetic stirrer for 24 h at 80 °C. The great innovation of this work is that we use the latest electroactive polymer powder of Arkema/Piezotech, France.

Then the material was screen printed with Ekra Asys Group unit at room temperature. Deposition parameters were: squeegee speed of 200 mm/s, pressure of 8 N. The prepared ink was placed on the screen manually with a syringe, and then transmitted to the substrate by the machine-controlled squeegee (Figure 2.4).

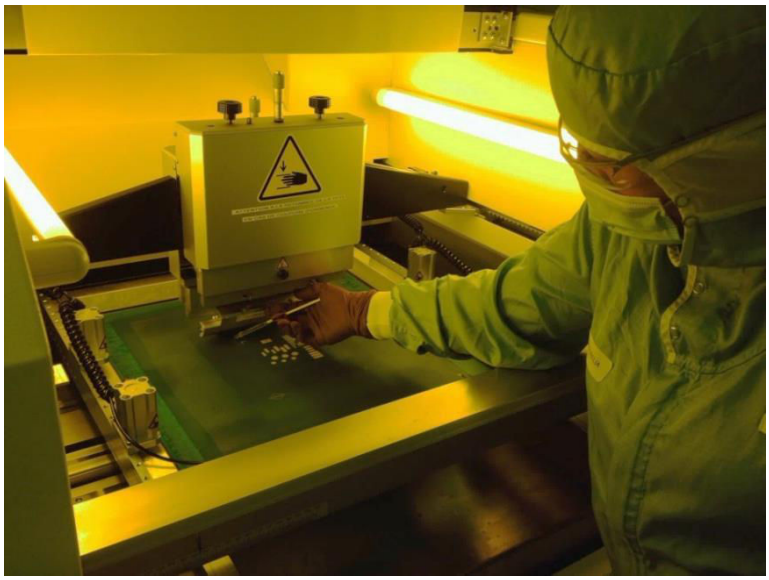

Figure 2.4. Screen printing deposition process with Ekra. The screen and the squeegee are visible.

The typical target of thickness was of few microns. The minimal thickness (1.3 µm) was limited by the printing technique. The maximal thickness (3.9 µm) was limited in our work by the polarization process. Typically, 100 V/m to polarize a film of P(VDF-TrFE) is required (will be discussed further in Chapter 3). Films of several microns thickness will be therefore difficult or impossible to polarize with existing equipment because of the high electrical voltage that would be required. That is why our target was 4 µm at a maximum to be sure they could be poled.

Top electrode

A set of top electrodes was deposited for polarization and charge collection. We have used a plate capacitor structure with metal-insulator-metal (MIM) assembly (Figure 2.5).

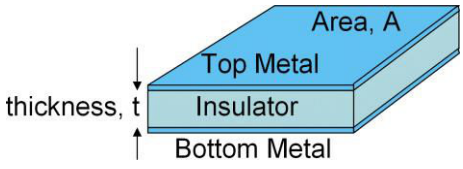

Figure 2.5. Plate capacitor (MIM-structure).

In this work, the top electrodes were deposited by screen printing. They consisted in different materials. We started with Ag paste specially formulated for screen printing (~ 5 µm thick) (Novacentrix HPS 021LV [69]). Then, we used a more advanced organic

electrode material i.e. an aqueous solution of PEDOT:PSS Clevios™ S V4, from Heraeus, Germany (~ 0.4 µm thick). Its viscosity ranges from 15-60 dPas, and resistivity is equal to 400 Ohm/sq [70]. After screen printing, PEDOT:PSS was dried the same way as the piezoelectric layers.

Protection layer

PEDOT:PSS electrodes have numerous advantages (electrical, optical and mechanical), however they are sensitive to the environment (i.e. moisture and oxygen) and are not stable over time without protection. Therefore, here we used a screen printable organic protective material (~ 1 µm thick). The protection layer consisted of simple large patterns (square or rectangles) covering all microgenerators area, except the test pads.

2.1.2 Sample fabrication: multilayer deposition of P(VDF-TrFE)

In screen printing technology the thickness of the deposited layer usually depends on ink viscosity and machine parameters (speed and pressure of squeegee etc.). With Arkema PVDF-based inks the minimal practical film thickness is ~ 1 µm. However, for energy harvesting applications the figure of merit is the density of energy which increases with capacitance and square voltage ($E = ½ CV^2$). The thickness of the piezoelectric material is a variable to adjust both the capacitance (in case of plate capacitor $C=\varepsilon\cdot\varepsilon_0\cdot S/t$) and the output voltage ($V=g_{ij}\cdot\sigma\cdot t$).

For this purpose, we developed a multilayer process used for the first time with ink-based P(VDF-TrFE) and P(VDF-TrFE-CTFE). The process consists in depositing each layer by screen printing on top of the previous one after drying. The number of alternations was comprised between 1 and 3. The total thicknesses varied from 1.1 to 3.9 µm depending on the number of layers deposited. The crystallization was done by annealing after each deposited layer.

Measuring the resulting total thickness of the multilayers and observing the interfaces between layers are important issues for the application, as the performances may depend on them. Therefore, this was done by a combination of surface profilometry, special cross-sectional microtomy and scanning electron microscopy (SEM).

Surface profilometry

Mono-, bi- and tri-layers of P(VDF-TrFE) films were measured on a Dektak stylus profilometer. Figure 2.6 shows a typical profile for a bilayer after drying and annealing. Repeatability was confirmed by testing five samples of each thickness and each sample was measured five times. The same measurements were done for P(VDF-TrFE-CTFE) films and multilayers. From these measurements total film thicknesses were obtained.

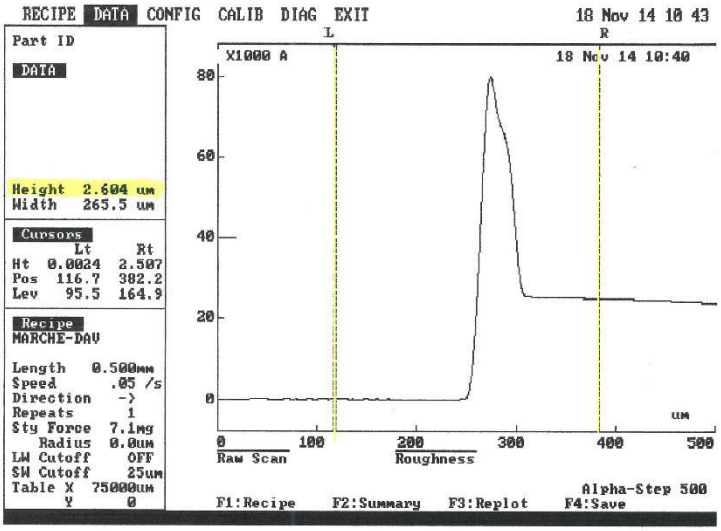

Figure 2.6. Typical profile of two deposited layers of P(VDF-TrFE).

As a result, we obtained a reproducible screen printing single layer of P(VDF-TrFE) of 1.3 µm ± 5% thick. Then, double and triple deposition lead to multilayers of 2.6 ± 5% and 3.9 µm ± 5% respectively. This indicates that successive screen depositions do not affect the targeted thickness which is the exact sum of the thickness of the previous layers. Considering the deposition of P(VDF-TrFE-CTFE), the thickness of the single layer was 1.1 µm ± 5% and that of multilayers is also the sum of the thickness of the previous layers of P(VDF-TrFE-CTFE). Also, we observed the same behavior for the deposition of heterostructures of P(VDF-TrFE) and P(VDF-TrFE-CTFE).

Although these results by profilometry look correct, additional direct observation of the layers by means of cross-sections of the film samples were performed.

SEM

SEM observation of polymers requires a special sample preparation. To see a cross-section of films and multilayers, small sections of them were prepared by microtomy. In this method, the sample is placed inside a hard rubber matrix and then cut with a diamond blade to obtain the cross-section specimen. Then, the samples were carbon-coated by electron beam evaporation to make the viewing surface conductive in order to avoid electrical charges to accumulate on the samples under beam exposure and therefore limit local melting of the polymer.

Figure 2.7 shows a SEM image after microtomy for the bilayer of P(VDF-TrFE) consisting of the successive deposition of two layers 1.3 µm thick. The whole structure of the microgenerator appears going from bottom to top with the PEN substrate, Au bottom electrode (30 nm), P(VDF-TrFE) layer (2.6 µm), PEDOT:PSS top electrode (0.4 µm) and the final protection layer (1 µm). The observations were done in a Zeiss Ultra SEM with 5 kV field and focal distance of 6.7 mm.

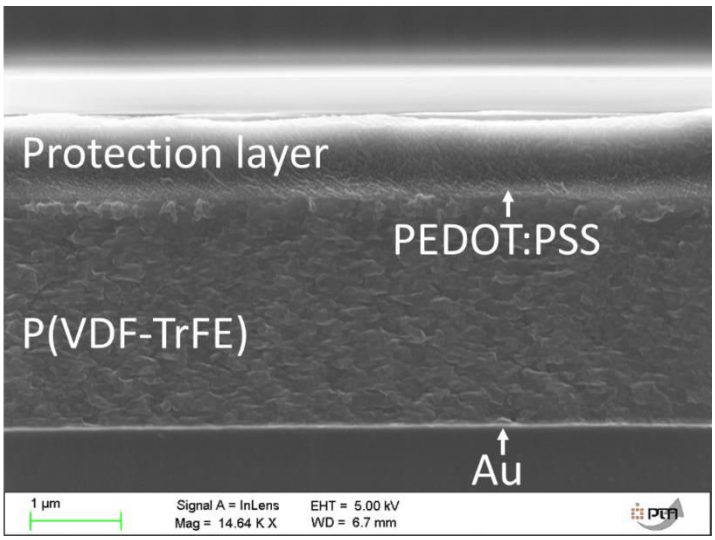

Figure 2.7. Microtomy cross-section SEM image of a bilayer of P(VDF-TrFE) after annealing. The whole structure of the microgenerator is also shown.

As a key outcome of the sample realization of this work, this image demonstrates that the whole microstructure of the multilayer is well-uniform with no residual trace of the two-time screen printing deposition and drying. Indeed, there is no visible interface or dead layer between the two layers.

Thus, we conclude that the screen printing multilayer deposition of P(VDF-TrFE) was able to produce homogeneously crystallized films with no cracks or other defects, which are suitable for applications.

2.1.3 Sample fabrication: top electrode materials

With the plate capacitor structure, the top electrode material deposition can be a technological issue. With screen printing, commercial silver paste is commonly used. It is a low cost material and it does not need to be protected from environment. This material was used in the early fabrication steps of this work.

Microtomy was pursued in order to study the upper interface of the piezoelectric and the top electrode materials. Figure 2.8 shows the whole structure for an Ag-based microgenerator. Note that the images are upside-down here going from top to bottom with the PEN substrate, Au bottom electrode (30 nm), P(VDF-TrFE) layer and the Ag-paste electrode. Figure 2.9 is an increased magnification, showing a penetrating Ag flake into the P(VDF-TrFE) layer.

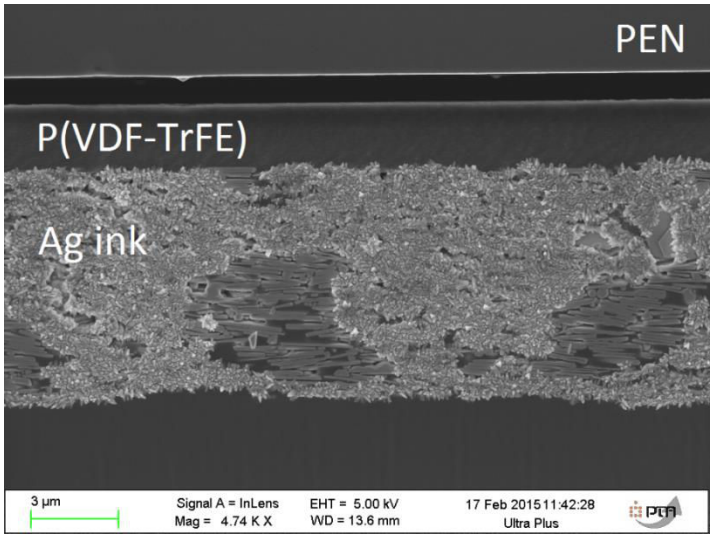

Figure 2.8. Cross-section SEM image of microgenerator with Ag top electrode.

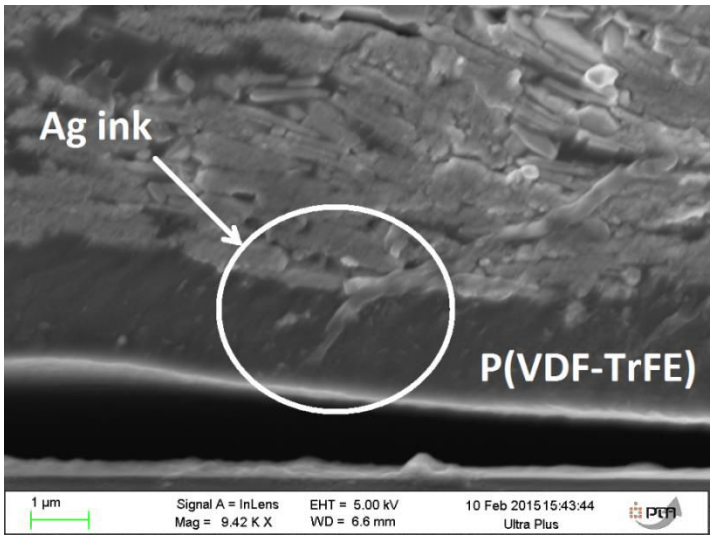

Figure 2.9. Cross-section SEM image of microgenerator with Ag top electrode (higher zoom). A flake of Ag ink is penetrating into P(VDF-TrFE).

From these pictures, it can be said that the commercial Ag-paste is not suitable for our applications. Indeed, the paste is very thick (~ 8 µm) and consists of big Ag-flakes (~ 2 µm). Thus the flakes can easily penetrate and perforate the polymer layer which is relatively thin in contrast, creating deep defects and even short cuts between the top and bottom electrodes.

If we now compare with the PEDOT:PSS top electrode sample, shown in Figure 2.7, we conclude that it is much better suited for the applications. That is why the final choice fell on PEDOT:PSS with organic protection.

2.2 Design and test structures

This section presents the design of the different structures used in this thesis. The design for the microgenerators used in this work targets principally the g_{31} piezoelectric mode, which is simpler to implement and use for applications. Thus, most of the test structures are regular plate capacitors with continuous films of piezoelectric polymers.. Additionally, we also explore the operation in g_{33} mode with nanostructured films of polymers. This requires another design based on interdigital electrodes (IDE) which will also be shortly described here.

2.2.1 Design-1: single capacitor

Functional dielectric materials, including piezoelectrics, require being associated with capacitive test structures to investigate their physical properties. There are two main schemes: plate capacitor (or metal-insulator-metal MIM) and interdigital structures (IDE). In this work, we mainly used single MIM structures for the overall material study on continuous films and multilayers and we retained an IDE scheme to explore nanostructured films of polymers. Later, for the purpose of the prototyping in the format of a credit card, single MIM capacitors will be extended to a network of capacitors connected in parallel .

The schematic of the MIM test structure is simple as shown in Figure 2.10. The particularity is that it is flexible to allow piezoelectric voltage characterization vs. applied strain. On the top view, one can see with transparency the juxtaposition of the four layers: bottom electrode, dielectric, top electrode and passivation. The indicative cross-section is given and corresponds to the technological layer stack that we just described.

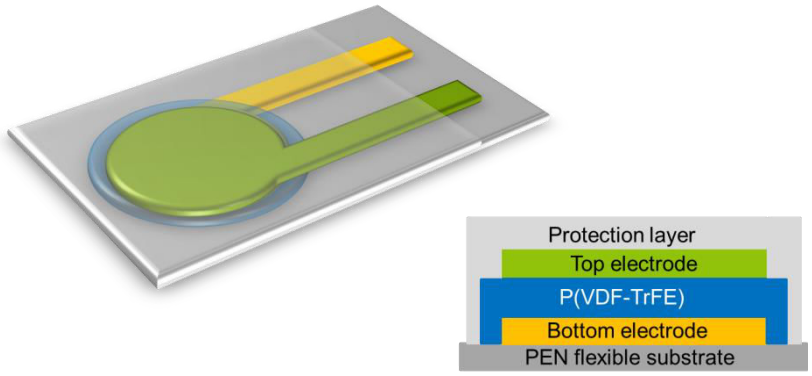

Figure 2.10. Design-1: single capacitor MIM structure.

Figure 2.11 is an illustration of the as-fabricated single MIM capacitor test structures on a flexible PEN substrate. The design consists in circular capacitors of two diameters of 5 mm and 7.5 mm. These dimensions had theoretical capacitance values of 1.6 nF/µm and 3.7 nF/µm, respectively, considering a value of 9.4 for dielectric constant of P(VDF-TrFE). Circular shape is preferred to square or rectangular as it avoids edge effects during screen printing. Then, each electrode is prolonged laterally by lines ending with pads (for connector or tip measurements).

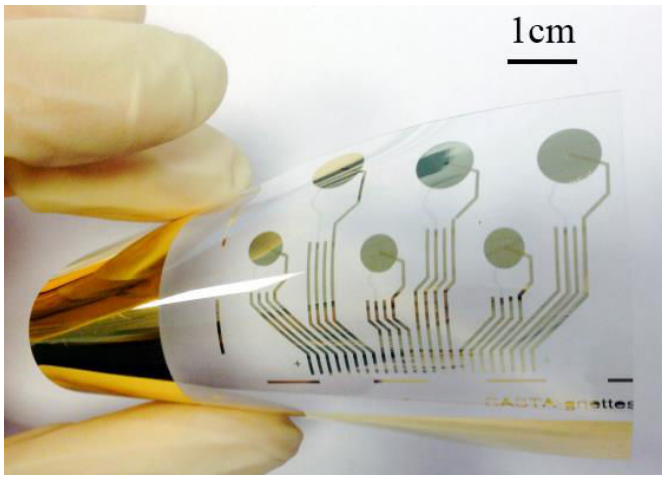

Figure 2.11. Screen printed P(VDF-TrFE) single MIM capacitor test structures for material study. Only Au at the bottom electrode can be seen on the picture as P(VDF-TrFE) and PEDOT:PSS are transparent.

2.2.2 Design-2: parallel connected capacitor network

We target applications based on a credit card format (8.5 cm x 5.5 cm) for our energy harvesting device. Theoretically, we have two options for the design of the piezoelectric generator: a single full-sheet area sized capacitor or small individual capacitors connected in network. The former is not suitable as we observe cracks developing after screen printing on large surfaces, typically above 2 cm^2. The reason for crack formation remains unclear, but we may assume internal stress and thermal expansion issues with the substrate. Thus, the practical size of capacitor/generator should be sub-cm. That is why we went in the direction of a network of parallel connected capacitors based on the single MIM structure. The four screens were redesigned for this purpose. All masks were drawn by us using CleWin 5 software and the designs are shown in Figure 2.12.

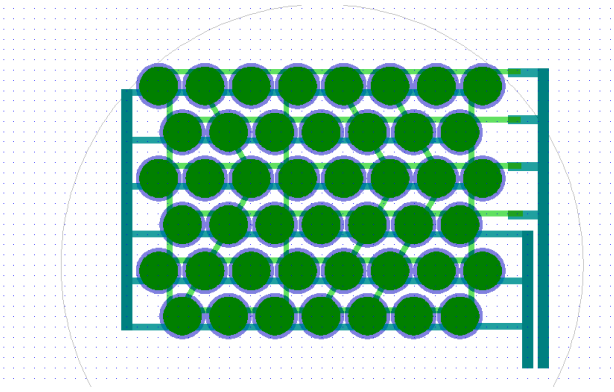

Figure 2.12. Design-2 in CleWin 5 software.

The final design consists in alternate lines of 8 and 7 circular capacitors (of diameter 7.5 mm) in staggered rows to maximize their surface density. The connection pads are situated on the right side and are made at the bottom electrode level (Au). The bottom electrodes (Au) are interconnected with horizontal lines terminated by a vertical line on the left and connect to the left pad. The top electrodes (PEDOT:PSS) are interconnected with horizontal lines shifted from those of the bottom electrodes and terminate by connecting laterally the right pad. Also, some redundancy of connections between the staggered rows was added at the top electrode level to ensure the electrical continuity of the network at the end. These extra lines can be seen by transparency in Figure 2.13.

Finally, the network design comprises 45 capacitors of diameter 7.5 mm, occupying 42.5% of the total surface. It results in a total theoretical capacitance of 165.3 nF/µm. Such original credit card design aims to fulfill the requirements of pocket-size applications such as payment display cards with integrated dynamic security [71].

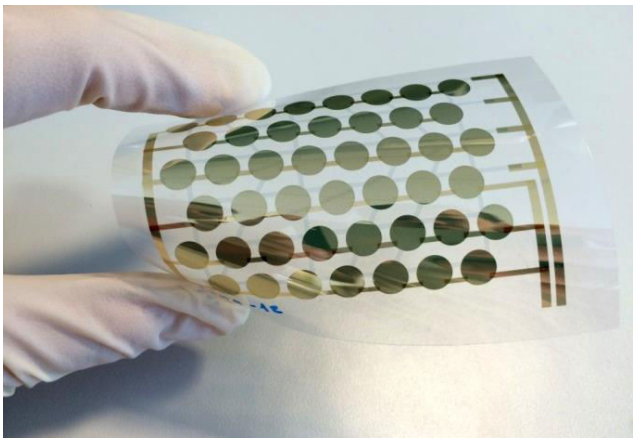

Figure 2.13. Network of 45 parallel connected capacitors of P(VDF-TrFE) in a credit card format.

2.2.3 Design-3: interdigital electrodes

Finally, the bottom interdigital electrodes (IDE) were designed and realized. Such kind of electrodes allows in-plane poling, actuation and sensing, making use of the higher g_{33} coefficient. The relevant example is the P1 type MFC actuators from Smart Materials (Figure 2.14) [72]. When implementing IDE structures, it is sufficient to deposit both electrodes only on one side of the piezoelectric material, thus leaving the other side available for additional

modifications. In our case we have used IDE to realize and test a new structure of P(VDF-TrFE) modified by nanoimprint lithography.

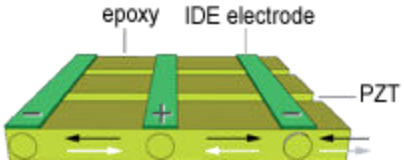

Figure 2.14. P1 type MFC actuator.

The IDE were designed in Clewin 5 software by us and fabricated on PEN substrate by lithography in the PICTIC platform. Two designs were realized: a first one with electrode width of 10 µm and gap of 10 µm, and a second one with width/gap of 5/5 µm. The overall area of the electrode was 1x1 cm^2 in both cases (Figure 2.15). The lithography mask contained five copies of each design.

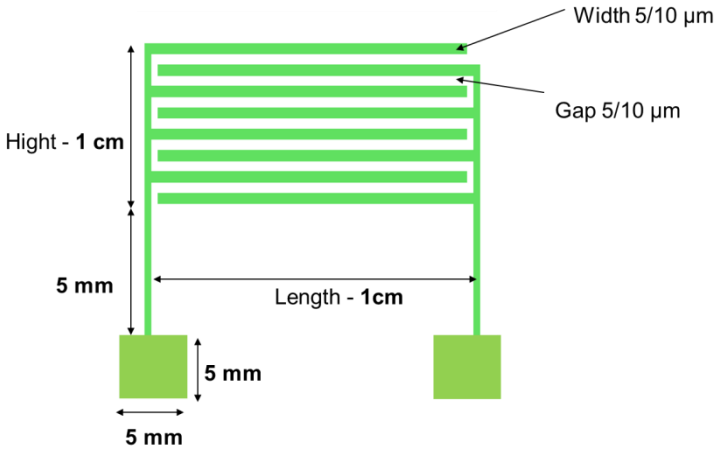

Figure 2.15. Design of IDE with corresponding geometrical parameters (not to scale).

The fabricated structures are shown in Figure 2.16. A 30 nm Au layer was used as electrode material.

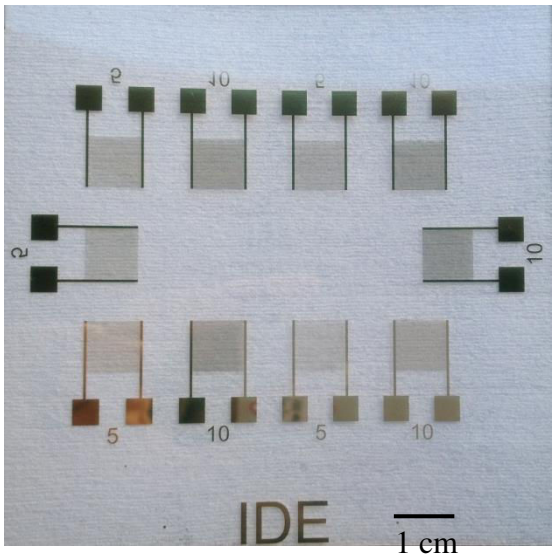

Figure 2.16. Fabricated IDE structures on PEN substrate.

Theoretical calculations by finite elements method (performed by N. Galopin, method described in [73] have given theoretical capacitance of 304 pF for 5/5 design and 92 pF for 10/10 design, both for 2.6 µm thick P(VDF-TrFE) layer. It was shown that to induce an electric field of 100 V/µm, necessary to polarize the piezoelectric, the application of 300 V is required for 5/5 design (Figure 2.17). For 10/10 design more than 400 V is required, which is not accessible with the experimental equipment used here.

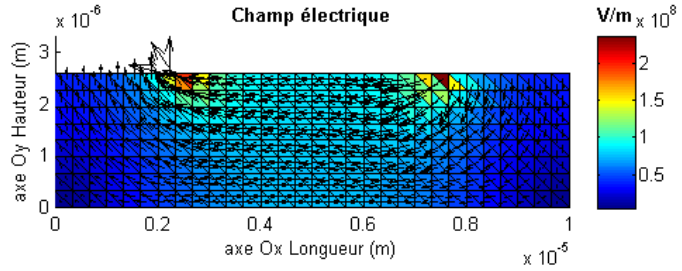

Figure 2.17. Visualization of theoretical electric field in 2.6 µm thick P(VDF-TrFE) with applied 300 V to 5/5 µm IDE design.

2.3 Exploratory: heterostructures

Motivations

Heterostructures, superlattices or multilayers of different natures are of great interest due to their potential for enhanced properties. In this section, we are going further in pushing

the previous multilayer screen printing process with the combination of different piezoelectric materials. The objective is mainly technological and exploratory and involves the use of very recent inks of co- and terpolymers of PVDF produced by Arkema/Piezotech, regardless of realistic applications. The idea behind this study is the hardening of ferroelectric materials to avoid depolarization.

The idea of multilayers with piezoelectrics comes from an analogy with magnetism where antiferromagnetic/ferromagnetic (AF/F) multilayers are used to make exchange biased pinned magnetic structures (hardening ferromagnetics), i.e. they behave like intermediate synthetic hard magnet materials with enhanced coercive field and shifted hysteresis loops. The reader may refer to Bernard Viala HDR report for a broader understanding and overview of applications [74]. Even if the physical origin of the phenomenon is fundamentally different (one is magnetic, the other is electric), we can expect expects similar results: shifted hysteresis loops and enhanced ferroelectric coercive fields (instead of magnetic) which makes the material less prone to depolarization when being used as a piezoelectric generator. However a strict analogy is limited here because antiferroelectric materials (AFE) do not exist in polymeric form. Only AFE ceramics are known, mainly $PbZrO_3$ (PZ), as the first identified compound in 1951 [75], and more recently Fe-doped $Pb(Zr_{0.58}Ti_{0.42})O_3$ (PZT) [76] and Sr-doped doped PZ [77]. They are particularly attractive for high energy storage capacitors due to their unique electric field induced AFE-FE phase transition. The reader may find more details on this topic in [78].

Thus, as the terpolymer of PVDF is a relaxor (and not antiferroelectric), this section is interested in the deposition of exploratory RE/FE (RElaxor/FerroElectric) heterostructures of P(VDF-TrFE) and P(VDF-TrFE-CTFE) by screen printing. A short state of art of RE/FE materials is summarized below.

Literature overview

There is existing literature concerning RE/FE epitaxial perovskite materials such as superlattices of $BaTiO_3/SrTiO_3$ [79], $PZT/PbZrO_3$ [80]–[82]. Also, there are reports of hysteresis-free piezoelectric complex RE/FE solid solutions of $Pb(Mn_{1/3}Nb_{2/3})$O3-PbTiO3, $Pb(Zn_{1/3}Nb_{2/3})O_3$-$PbTiO_3$ [83], [84] **.** These works target the enhancement of the piezoelectric response along nonpolar directions. When measured along a nonpolar direction, the domain walls are ferroelastic but their switching will not contribute to the strain, since in this configuration their displacement (reversal) preserves the shape of the crystal. Indeed, the

strain-electric field relationship for such a domain structure is anhysteretic. In these conditions, RE/FE systems may generate strain several times larger than classical PZT-based materials.

In contrast, very few works can be found about RE/FE polymer-based systems [85]–[87]. The common aim of these researches is to improve and tune electrical properties (dielectric, ferroelectric and piezoelectric). For example: increase the permittivity ε_r, reduce losses tan δ, increase the d_{ij} piezoelectric coefficients, increase the remanent polarization P_r, etc.

However, ferroelectric multilayers cannot be assumed as individual capacitors connected in series, which would be an erroneous oversimplification of the problem. There is a key role played by the interfaces between the various layers: interlayer strain (strain coupling) and interaction of the dipoles at the interfaces (electrical coupling). Various theoretical models explain the role of intrinsic coupling and interfacial coupling. Existence of strong long-range electrical interaction across the interfaces was demonstrated [88]–[90]. Also interfacial strain was identified as dominant mechanism [91].

Experimental

The previous multilayer screen printing process was used to produce different samples of multilayers of P(VDF-TrFE) and P(VDF-TrFE-CTFE) which will be electrically tested later. Samples of only copolymer or only terpolymer were also deposited as references. The different configurations are summarized in Figure 2.18.

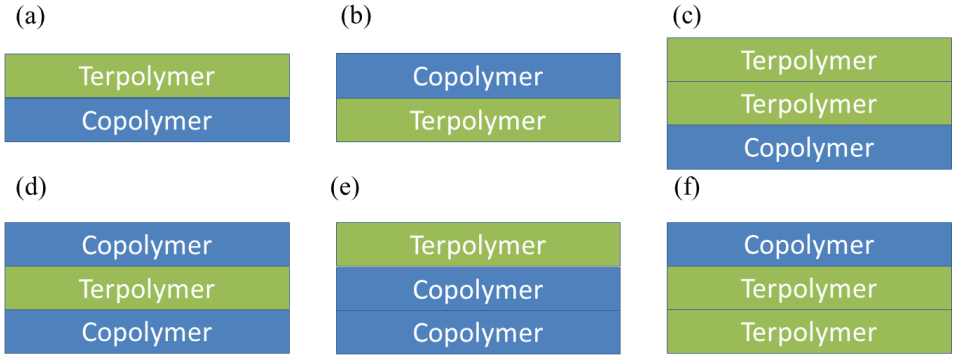

Figure 2.18. Schematic of the multilayer heterostructure configurations of screen printed P(VDF-TrFE) and P(VDF-TrFE-CTFE).

Prior to the deposition of heterostructures of P(VDF-TrFE) and P(VDF-TrFE-CTFE), the deposition of the terpolymer alone was studied. We used the same screen printing conditions as for the copolymer although there can be a slight difference in viscosity. The drying process was similar, only the annealing temperature was lower (120 ºC instead of 130 ºC). Thus, the whole process results in slightly thinner films of P(VDF-TrFE-CTFE) with 1.1 µm (instead of 1.3 µm for P(VDF-TrFE)).

It should be noted that heterostructures with a copolymer layer on top were dried also at 120ºC, which are not the optimal annealing conditions, since higher temperature is necessary for the copolymer. Table 2.2 gives an indication of the overall fabricated samples of this work.

Structural analysis

The process allowed depositing structures consisting of alternating layers of P(VDF-TrFE) and P(VDF-TrFE-CTFE) with success. As a result, an example of microtomy and SEM cross-section observation is shown in Figure 2.19. It corresponds to the multi-P-5 sample, which consists of two layers of P(VDF-TrFE) and one layer of P(VDF-TrFE-CTFE). Thus, we can conclude on a defectless and overall homogenous microstructure of the fabricated heterostructures. These experimental findings open others ways to investigate further for applications.

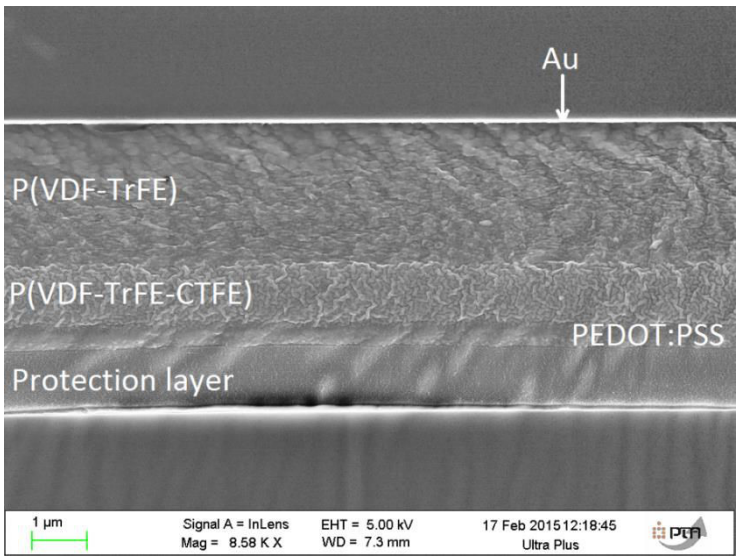

Figure 2.19 Cross-section SEM image of the 2-step deposited P(VDF-TrFE) and 1-step deposited P(VDF-TrFE-CTFE).

Table 2.2. Overview of the fabricated samples.

Name	Polymer thickness, µm	Top electrode
	P(VDF-TrFE)	
copo-Ag-1	1.3	Ag
copo-Ag-2	2.6	Ag
copo-Ag-3	3.9	Ag
copo-P-1	1.3	PEDOT:PSS
copo-P-2	2.6	PEDOT:PSS
copo-P-3	3.9	PEDOT:PSS
	P(VDF-TrFE-CTFE)	
terpo-Ag-1	1.1	Ag
terpo-Ag-2	2.2	Ag
terpo-Ag-3	3.3	Ag
terpo-P-2	2.2	PEDOT:PSS
	Multilayers	
multi-Ag-1 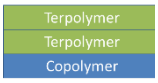	3.5	Ag
multi-Ag-2 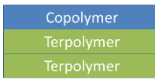	3.5	Ag
multi-P-1 	2.4	PEDOT:PSS
multi-P-2 	2.4	PEDOT:PSS
multi-P-3 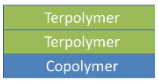	3.5	PEDOT:PSS
multi-P-4 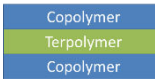	3.7	PEDOT:PSS
multi-P-5 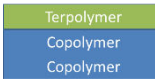	3.7	PEDOT:PSS

2.4 Summary of the fabrication

The key outcome of the experimental work is the achievement of a reproducible screen printing process with new ink-based P(VDF-TrFE) materials, including the deposition of multilayers. We report no evidence of dead layer, interfacial defect or inhomogeneity of the film microstructure. In contrast, we showed that the top electrode material is an issue as it can cause detrimental structural damages onto the piezoelectric film. Thus, a functional process flow was established for the fabrication of the flexible piezoelectric microgenerators of this work.

The design of test samples was described, mainly based on the plate capacitor model for the continuous films, but also an alternative interdigital scheme for the nanostructured films coming later. The design has evolved from single capacitor test structures for material investigation towards parallel connected capacitor network structures fitting on a credit card format for the applications. The fabrication of the prototypes was fully completed.

Finally, we opened new directions of investigation summarizing the exploration technological work on original heteterostructures of P(VDF-TrFE) and P(VDF-TrFE-CTFE) produced also by screen printing.

The full electrical characterization of the obtained samples will be presented in the following chapters, with some optimization of fabrication parameters.

Chapter 3. Ferroelectric properties

This chapter is mainly devoted to the ferroelectric properties of the screen printed P(VDF-TrFE) samples. The material test structures are the single MIM capacitors previously described. In addition, preliminary results for P(VDF-TrFE-CTFE) and heterostructures P(VDF-TrFE) and P(VDF-TrFE-CTFE) are also reported. The chapter starts with a brief review of the state of the art of recent measurement and polarization techniques used for piezoelectric polymers. The poling, required to establish stable ferroelectricity, is first introduced. The piezoelectric properties will be discussed further in Chapter 4.

PVDF and its copolymer P(VDF-TrFE) exhibit strong ferroelectric properties [92]. Since all ferroelectrics are also piezoelectrics (due to crystal symmetry), it is necessary to investigate both properties to give a complete analysis of the material. Ferroelectricity in PVDF is caused by the dipoles that spontaneously polarize and align with external electric field. The polarization of the dipoles can be switched to the opposite direction with the reversal of the electric field. Often the ferroelectric measurements are performed prior to the piezoelectric characterization in order to evaluate their early potential and further suitability for applications such as generators, sensors and actuators [32], [93]–[96].

3.1 State of the art

3.1.1 Poling methods for polymers

In order to obtain and stabilize ferroelectric properties, PVDF and its copolymers need to be poled. There are several methods of poling for polymers such as “electrode” poling (also called “thermal” poling), “corona” poling and “electron-beam” poling.

Electrode poling

Electrode poling (Figure 3.1) is performed by applying a high electric field (more than the coercive field) directly across electrodes either at room or elevated temperatures [32],

[94]. In the latter case it is called “thermal poling”. This method is easy to implement, requires application of intermediate voltage compared to the corona method and leads to higher polarization uniformity. But there are still some risks of electrical breakdown, especially for thin layers where thickness can be non-uniform due to imperfections, impurities or voids. This method is most frequently used for thin films and laboratory research.

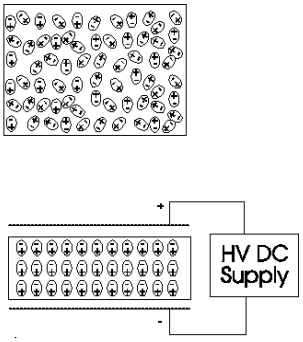

Figure 3.1. Simplified scheme of electrode (thermal) poling.

Corona poling

The corona poling method consists in exposing the bare surface of the polymer with positive or negative ions. Ions are produced by applying high voltage to an asymmetric pair of electrodes such as a point and a plate (see Figure 3.2). In the corona triode method a metal grid is introduced between the point and the sample to improve the uniformity of the surface potential [97]–[99]. Ions do not penetrate into the bulk, but transfer their charge and leave the surface as neutral atoms or molecules. The advantages of corona poling are:

- no need of deposited electrodes;
- higher fields compared to what electrode poling can achieve;
- electrical breakdown is limited only to a small sample area;
- compatible with large surfaces by moving the sample through the corona setup.

On the other hand, this method can chemically modify the surface of the polymer and thus its properties [100].

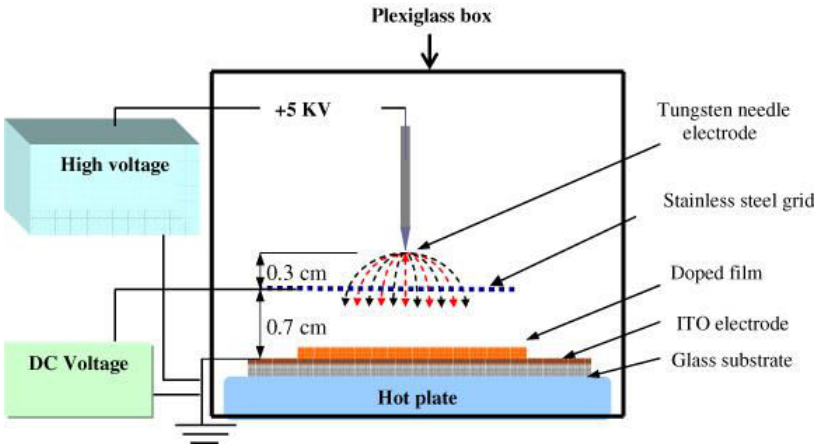

Figure 3.2. Schematic diagram of corona poling of polymers [98].

Electron-beam poling

In this method only one side of the sample is metallized and connected to the ground, while the other non-metallized side is subjected to irradiation of electrons [99], [101]. The electrons penetrate into the polymer and form a space-charge layer as shown in Figure 3.3. The space-charge region generates an electric field, which orients the dipoles towards the bottom electrode. By varying the energy of the electron beam it is possible to control the polarization depth. It is also possible to perform local polarization with a spatial resolution of a few microns by using a focused electron beam with a scanning electron microscope [102]. Nonetheless electron irradiation may lead to material degradations (chemical and structural).

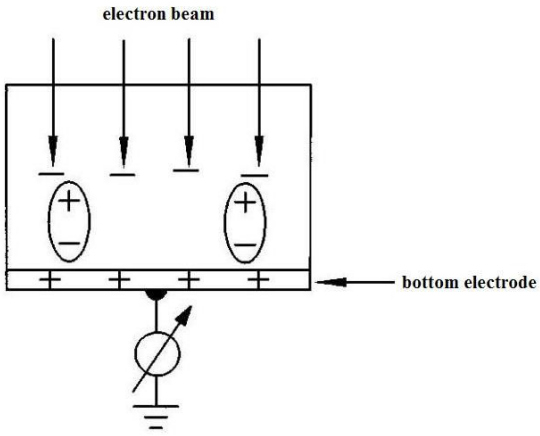

Figure 3.3. Schematic diagram of electron beam poling. The electrons penetrate into the polymer and form a space-charge layer [99].

3.1.2 Ferroelectric properties of P(VDF-TrFE)

Ferroelectric properties of P(VDF-TrFE) have been extensively studied. We will now present a selection of recent works on thin films of P(VDF-TrFE).

In 2007 Fujisaki et al. [103] presented MIM capacitors using 60 nm-thick P(VDF-TrFE) films for memory applications. The copolymer films were obtained by a spin coating process with annealing at 140 °C. A high remanent polarization P_r = 11.9 μC/cm^2 was reported with a coercive field E_c = 33 V/μm, measured at 1 kHz. As we will see further, 11.9 μC/cm^2 is the highest P_r value reported so far. It may be related to the very small thickness of the film which makes them easy to polarize.

In 2008 Asadi et al. [95] investigated a spin-coated P(VDF-TrFE) copolymer for non-volatile memories applications. Measurements with a Sawyer–Tower circuit showed a coercive field E_c = 50 V/μm and a remanent polarization P_r = 6 μC/cm^2. The dielectric constant ε was determined from C–V measurements and was approximately 10 at 0 V.

Pabst et al. [93] in 2013 fabricated and characterized an all inkjet-printed piezoelectric polymer actuator using P(VDF-TrFE) powder with a VDF:TrFE ratio of 70/30 wt%. The dielectric hysteresis loop was measured using a ferroelectric hysteresis measurement system (Easy Check 300, aixACCT). Measurements were run at a frequency of 0.05 Hz. A remanent polarization of $P_r \approx 6.5$ μC/cm^2 and a coercive field of $E_c \approx 30$ V/μm were obtained.

In 2014 a flexible nanogenerator using a spin-coated (PVDF-TrFE) 75/25 % mol thin film as functional layer on a polyimide substrate was fabricated by Pi et al. [32]. The relatively large remanent polarization of 7 μC/cm^2 and coercive field of 53.2 V/μm were measured for the 220-nm-thick copolymer film.

3.2 Materials and methods

Most of the tests were performed on the aixACCT TF 2000E analyzer probe station equipped with FE-Module (Figure 3.4). All measurements were realized at room temperature. The samples to be measured correspond to the MIM capacitors test structures presented above. They are connected with tips via the external pads which avoids damaging or perforating the intrinsic capacitor test structure.

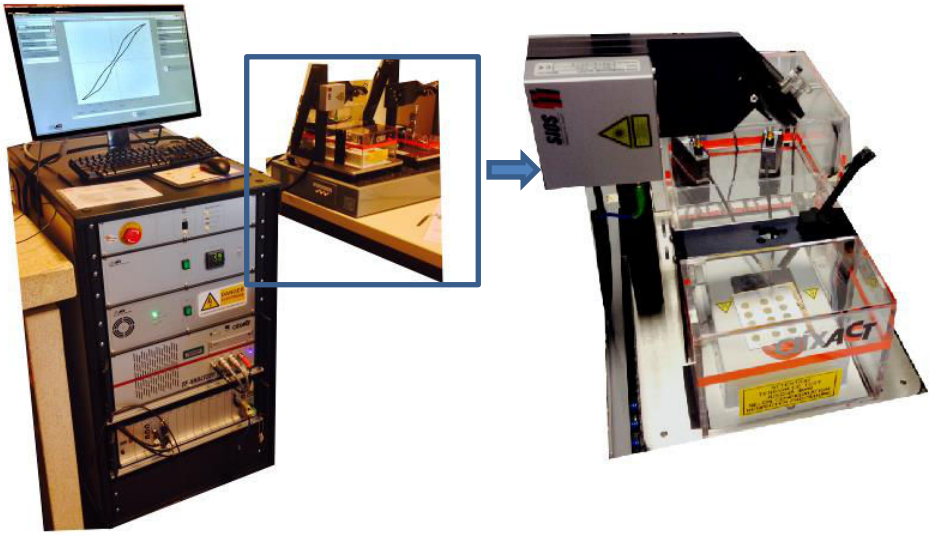

Figure 3.4. Pictures of the aixACCT TF Analyzer 2000E with FE-Module, and close up of the probe station.

3.2.1 Poling conditions

The poling of the samples was performed at room temperature based on the electrode poling method with using tips connecting to the pads. To do so, we use the maximum poling voltage (400 V) which generates the electric field uniformly and normal to the top and bottom electrodes. Considering the thickness of the samples, it corresponds to an electrical field exceeding 100 V/µm which is recommended to fully saturate P(VDF-TrFE) films [94]. Note that in the case of Ag electrodes the field was limited to lower values (~45 V/µm) due to hot spots associated with the structural defects previously identified and leading to early breakdown of the samples. The voltage was switched on and off instantly with no ramping. Various poling times from 1 s to 30 min were tested and practically no impact was found.

3.2.2 C-V measurement

Capacitance vs. voltage (C-V) was systematically measured as it provides further important parameters of ferroelectric capacitors. Especially it gives information about the reversible parts of polarization, and furthermore the switching process. During the measurements, the bias voltage starts at zero volts and increases up to the desired maximum excitation voltage $+V_{max}$, then goes down to $-V_{max}$ and then goes back to zero. This procedure ensures cycling through the whole hysteresis loop during the measurement. Capacitance and loss tangent (tan δ) are then derived from the current response of the sample.

C-V measurements are performed on the aixACCT TF 2000E with a bias voltage up to 400 V and in the frequency range of 10 Hz to 1 kHz. The measured capacitance values were then recalculated to the relative permittivity (ε_r) by the following formula of the plate capacitor:

$$\varepsilon_r = \frac{C \cdot t}{\varepsilon_0 \cdot S} \tag{3.1}$$

where C is the capacitance [F], t is the thickness of the sample [m], ε0 is the vacuum permittivity [$8.85 \cdot 10^{-12}$ F/m], and S is the area of the electrodes [m2].

To be complementary to FE-Module of aixACCT, capacitance versus frequency measurements were also performed on a manual probe station using the impedance analyzer HP 4191A to extend the achievable frequency range to 100 Hz - 1 MHz. The bias voltage was 100 mV. The measured capacitance, permittivity and loss tangent were extracted.

3.2.3 P-E measurement

P-E measurement is the key element for the understating of the ferroelectric properties. The FE-Module of aixACCT allows direct hysteresis loop measurement by setting the maximum saturation field. In our case it is fixed at 100 V/µm which exceeds the coercive field of P(VDF-TrFE) as seen from the literature. In more details, we used a triangular signal and the frequency was varied from 0.01 to 100 Hz. For repeatability (due to unknown initial remanent state), a single pre-polarization triangular pulse of the same amplitude as the measurement signal was applied to the samples prior to each measurement.

3.3 Results and discussion

The main results reported in this section concern the capacitor test structures of P(VDF-TrFE) with PEDOT:PSS top electrode. We start with the single capacitor design and go further with the parallel connected capacitors. Latter, we comment the effects of the top electrode materials (for instance with silver paste). Finally, we report preliminary electrical results about screen printed P(VDF-TrFE-CTFE) and heterostructures of P(VDF-TrFE) and P(VDF-TrFE-CTFE). For these results, when not specified, capacitance and permittivity values are reported for a constant voltage of 100 mV.

3.3.1 Capacitances of P(VDF-TrFE)

Design-1: single capacitors

The screen printed single capacitor test structures of P(VDF-TrFE) showed capacitance values between 1.2 nF and 400 pF (for 5 mm diameter) depending on the thickness of the dielectric. As a result the capacitance is proportional to the number of deposited layers of P(VDF-TrFE), as shown in Figure 3.5. This indicates once more that multi-step deposition does not induce major interfacial defects (i.e. dead layer, roughness etc.) or uncertainty on subsequent layer thickness, in accordance with SEM observations.

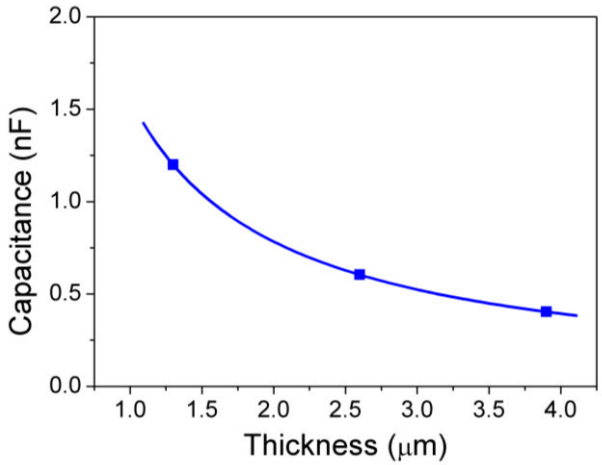

Figure 3.5. Capacitance thickness-dependence of screen printed P(VDF-TrFE) single capacitors.

Current leakage of the capacitors as function of voltage is a fingerprint of the dielectric quality. The corresponding results are shown in Figure 3.6. They reveal that the 1-step deposition results in increased leakage of the screen printed P(VDF-TrFE) capacitor in contrast to multi-step deposition. It may be explained by the formation of interfacial or structural defects (voids, cracks etc. or strain) since which the single layer of P(VDF-TrFE) is more exposed due to its relatively low thickness (1.3 μm). As a result, this is repaired by subsequent depositions.

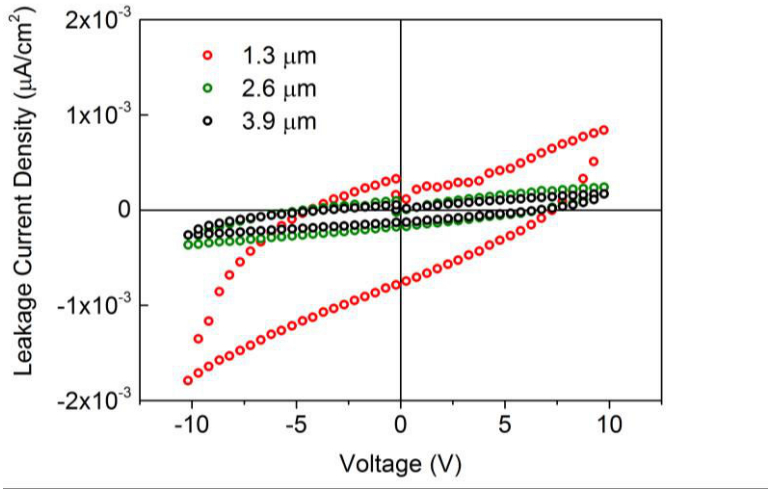

Figure 3.6. Leakage current density of screen printed P(VDF-TrFE) capacitors with PEDOT:PSS top electrode as function of thickness, measured at 1 kHz.

3.3.2 Hysteresis loops of P(VDF-TrFE)

Let us see the most important fingerprint of the screen printed P(VDF-TrFE) with an example of representative P-E hysteresis loops.

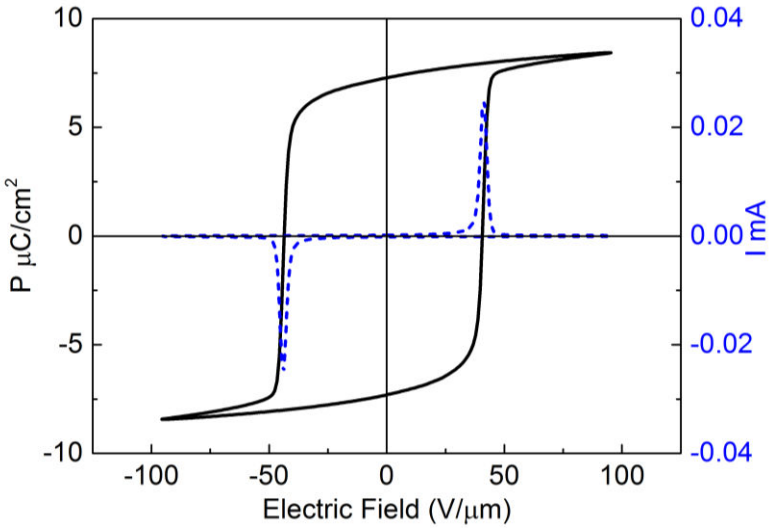

Figure 3.7. Typical P-E hysteresis loop at 0.1 Hz of 2.6 μm thick screen printed P(VDF-TrFE).

The values of polarization and polarization current were measured and recalculated automatically by the aixACCT FE-Module. For the P-E loops, measurement frequency of 0.1 Hz allowed obtaining the highest polarization and lowest coercive field values. From typical hysteresis loop (Figure 3.7) the average P_r and E_c values were found to be 7.5 μC/cm^2

and 40 V/μm respectively, which are among highest values found in literature. No significant thickness dependence is to report. The square shape of the hysteresis polarization loops is a positive indication of a high ferroelectric order with the poled copolymer samples. In addition to polarization hysteresis loops, the electric field dependences of permittivity (ε_r) and loss tangent ($\tan\delta$) are reported in Figure 3.8. The permittivity (ε_r) was recalculated from the capacitance values by using equation (3.1). The measurements were performed at 1 kHz. They are a complementary feature of ferroelectricity. Additionally, low $\tan\delta$ values suggest low dielectric leakage.

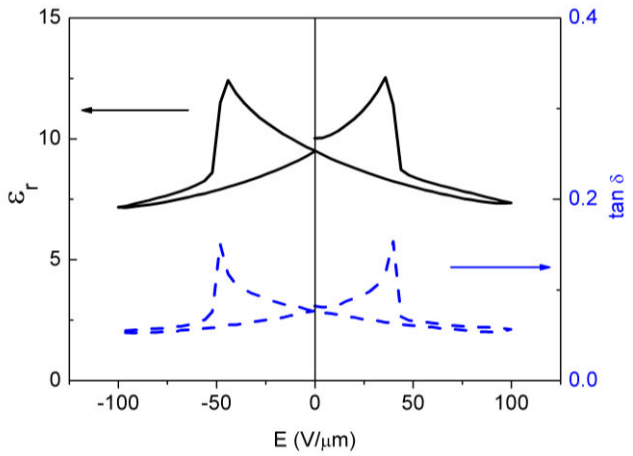

Figure 3.8**.** Typical ε_r-E and tanδ-E curves at 1 kHz of 2.6 μm thick screen printed P(VDF-TrFE).

To be complete, it is worth noticing that we observed a significant dependence of the shape of hysteresis polarization loop vs. the measurement frequency (Figure 3.9). Outside quasi-static conditions (>1 Hz) the coercive field increased significantly (almost by two times from 0.1 Hz to 100 Hz) and the polarization slightly diminished. Indeed, it was already demonstrated that for pure PVDF films that the remanent polarization decreases with frequency in the range of 0.01 to 1000 Hz, and in some cases it becomes negligible already at 10 Hz [104], [105].

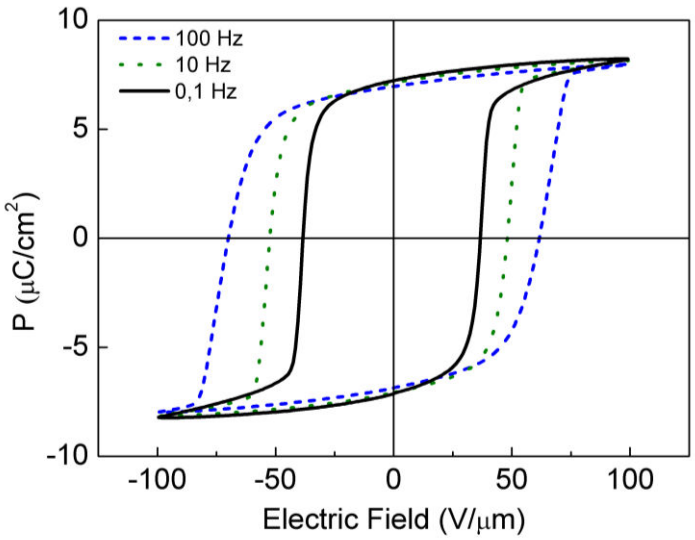

Figure 3.9. Typical frequency dependence of hysteresis loop of 2.6 μm thick screen printed P(VDF-TrFE).

Usually, this frequency dependence is much less pronounced for ceramic ferroelectrics, where the P_r and E_c values can stay nearly unchanged up to hundreds of kHz [106]. In the case of the screen printed P(VDF-TrFE) of this work, the behavior is in between. It is thus important to consider this frequency dependence when performing ferroelectric measurements of PVDF-based materials.

Nevertheless, back to our objectives, it is the static or quasi-static characteristics of the screen printed P(VDF-TrFE) which matters for the application, since those would be the operating conditions targeted for our microgenerators.

3.3.3 Aging with PEDOT:PSS

The test structures of this section, dedicated to material investigation, and latter those for prototyping are based on capacitors of P(VDF-TrFE) with a top electrode in PEDOT:PSS. This material is known to be sensitive to humidity and other environment factors that is why a protection layer was added. However, it is still worth considering aging of these structures even protected. This is the aim of this section.

In order to study the efficiency of this protection layer, we repeated electric measurements over time (17 months) on three sets of samples. The time dependence of the capacitance is shown in Figure 3.10.

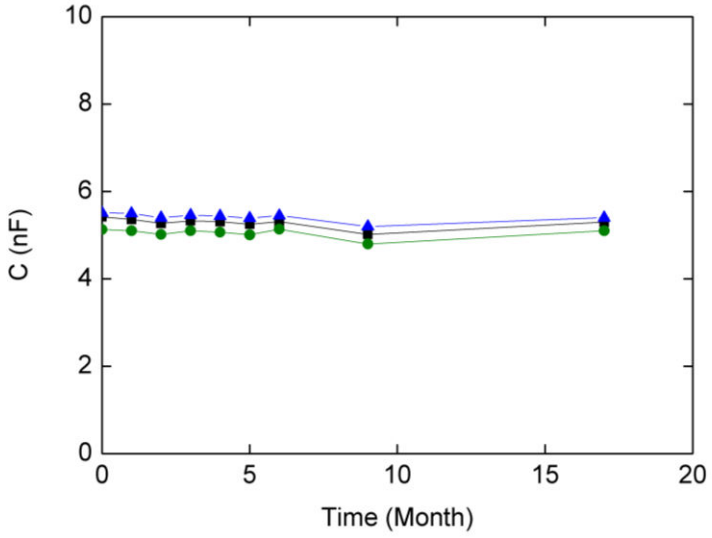

Figure 3.10. Time-dependence of the capacitance of PEDOT:PSS based capacitors.

As a good result, after 17 months no significant change was reported. Small isolated changes over time can be attributed to measurement error and not to aging. This leads to an intermediate status about negligible or weak aging of these almost entirely organic structures. However it is not enough to conclude. Further tests will be performed with electrical bias and heating.

3.3.4 Effects of top electrode materials

Since we accumulated samples with two different top electrode materials from the early fabrication time, we decided to devote this paragraph to report on their impact. Indeed, the nature of electrodes may strongly affect MIM ferroelectric capacitors. For this purpose, frequency dependent measurements of the capacitance or the permittivity ε_r were performed on the sidelines of this work. Consistently, we observed different experimental ε_r-f behaviors using with metallic (Ag) or organic (PEDOT:PSS) electrodes (Figure 3.11).

The impact of the use of Ag or PEDOT:PSS electrodes cannot be distinguished below 1 kHz. However at higher frequencies (~ 10 kHz), PEDOT:PSS samples exhibit higher dielectric losses, with lowered ε_r and enhanced tan δ. Ag-based capacitors seem to be more frequency-stable and the steep increase of dielectric losses appears latter at ~ 100 kHz. Therefore, one may conclude that Ag-based electrodes (i.e. metallic) would be preferred to PEDOT:PSS (i.e. organic) if high frequency use is a requirement.

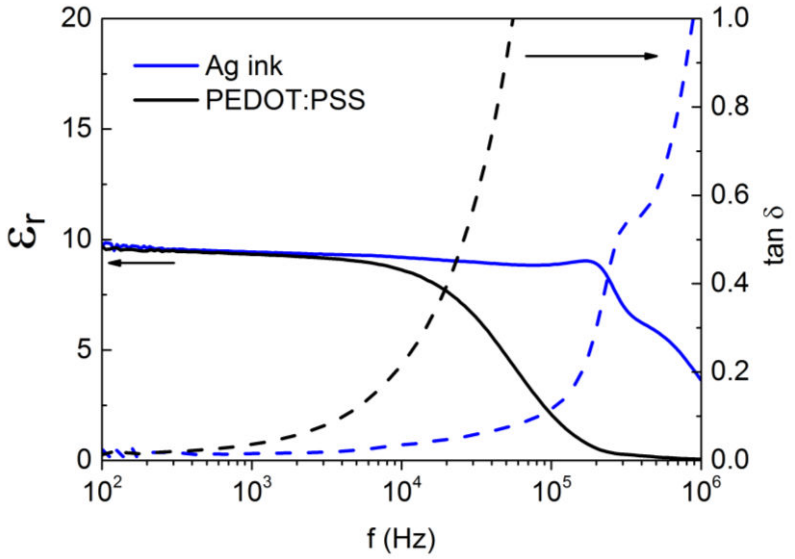

Figure 3.11. Frequency-dependences of permittivity and loss tangent of 2.6 µm thick screen printed P(VDF-TrFE) capacitors with Ag and PEDOT:PSS top electrodes.

Leakage current is another key sign of the impact of the electrode materials. The measurements were performed on two similar samples of P(VDF-TrFE) with Ag and PEDOT:PSS top electrodes, respectively (Figures 3.12 a and b). We can see that samples with Ag electrodes exhibit a leakage current density of two orders of magnitude higher than that of samples with PEDOT:PSS.

Thus, besides frequency characteristics (better with Ag) which are not on purpose for the targeted DC or quasi-static-based applications, the distinction between Ag and PEDOT:PSS is elsewhere. Indeed, leakage current and voltage breakdown are more decisive and this time, PEDOT:PSS electrode prevails over Ag. The latter consists of a paste of flakes responsible of promoting early electrical breakdown (~ 80 V/µm) due to hot spots or even shortcuts caused by the pinning of silver flakes into the polymer, as previously shown in Chapter 2, or at best strong leakage current. With PEDOT:PSS, we did not observe any breakdown below 400 V (or ~ 300 V/µm) and leakage current is almost negligible. Thus, PEDOT:PSS top electrode is better suited for screen printed P(VDF-TrFE) microgenerators as they will ultimately sustain higher piezoelectric voltage. Additionally, they are flexible.

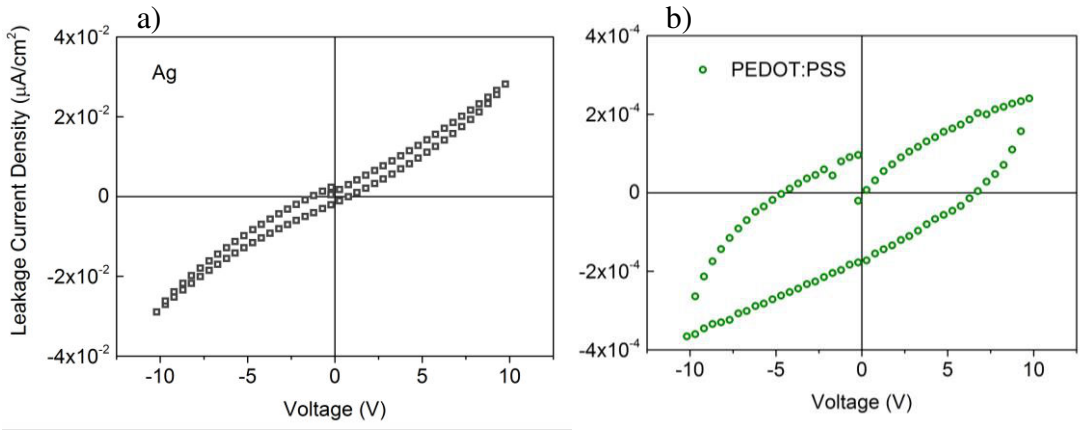

Figures 3.12. Leakage current density at 1 kHz vs. voltage of 2.6 μm thick screen printed P(VDF-TrFE) capacitors with Ag (a) and PEDOT:PSS (b) top electrodes. Note the different scales.

3.4 Exploratory: heterostructures

As shown in Chapter 2, the exploratory study of screen printed heterostructures starts with single deposition of P(VDF-TrFE-CTFE) and goes on with multilayer combinations of P(VDF-TrFE) and P(VDF-TrFE-CTFE). Here we follow the same progression.

Terpolymers: single layer

Again, let us see first the fingerprint of the screen printed P(VDF-TrFE-CTFE) with an example of a representative P-E hysteresis loop.

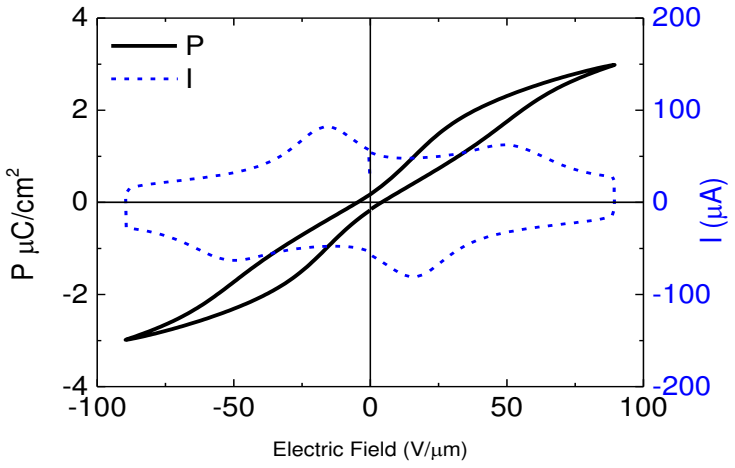

Figure 3.13. Typical P-E hysteresis loop at 10 Hz of 2.2 μm thick screen printed P(VDF-TrFE-CTFE).

Here, a special fingerprint at 10 Hz of the screen printed P(VDF-TrFE-CTFE) clearly appears in Figure 3.13 with "pinched loops". This particular feature is confirmed with ε_r-E and tanδ-E characteristics at 1 kHz as shown in Figure 3.14. This is an unusual observation for the PVDF terpolymers, as they are usually considered as relaxor [41], [42], [107], [108]. Indeed a relaxor should not have remanent polarization and hysteresis. C-V and I-V measurements are little or not provided in literature, and it is difficult to conclude on the nature of these rather new materials. However "pinched loops" are not unusual with ceramics.

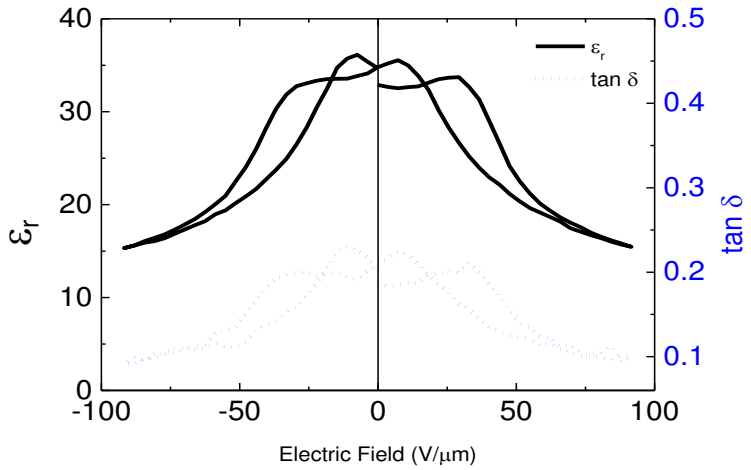

Figure 3.14. Typical ε_r-E and tanδ-E curves at 1 kHz of 2.2 μm thick screen printed P(VDF-TrFE-CTFE).

In literature about piezoelectric ceramics, atypical ferroelectric hysteresis loops are not unusual and they are associated with preferential orientation of the defect dipoles [109]. Hysteresis loops can be shifted or pinched in poled ceramics. A shift usually indicates the presence of an apparent internal bias field that originates from a perfect alignment of the dipoles along the macroscopic polarization direction. In unpoled ceramics, defect dipoles can have different orientations, for example along each side of every domain wall. This unparallel dipole configuration, which must not be confused with antiferroelectric order, leads to so called constricted or pinched loops. The pinching appears because some domains contain dipoles oriented along the positive directions of the measuring field and some along the negative ones. So, a pinched loop is composed of two partial loops, one with a negative and the other with a positive internal field. The pinching mechanisms in ceramics are now rather well understood [109]. However, to our knowledge, it is the first time that pinched loops are observed with P(VDF-TrFE-CTFE). No doubt they are the sign of uncompleted poling.

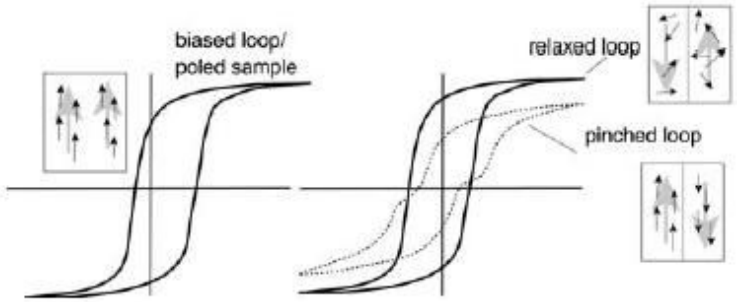

Figure 3.15. Schemes for biased, relaxed and pinched hysteresis loops. Defect dipoles are represented with black arrows and the macroscopic polarization directions with grey arrows. From [109].

To go further in the exploration, the frequency-dependence of hysteresis loops of P(VDF-TrFE-CTFE) was examined (Figure 3.16). At low frequencies (< 1 Hz), the pinched characteristic does not show up and measurements lead instead to round-shaped loops, typical of leaky structures [104]. In contrast, above 10 Hz (and up to 1 kHz), polarization and current measurements (Figure 3.17) clearly revealed the pinching. Also, it is worth noting that the frequency-dependence of the coercive field is inversed to that of the screen printed P(VDF-TrFE).

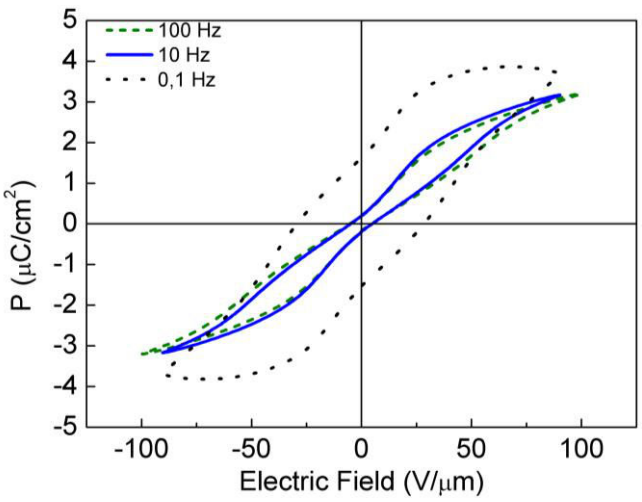

Figure 3.16. Frequency dependence of hysteresis loop of 2.2 μm screen printed P(VDF-TrFE-CTFE).

Usually, pinched loops with ceramics may persist up to high fields but they are usually relaxed by cycling the ceramic a large number of times (or by heating the sample). Here, the pinching continues to be observed even after repeated cycling. One may assume that the switching fields are not high enough to relax the defect dipoles of P(VDF-TrFE-CTFE),

confirming the assumption that it is indeed a poling problem. However at low frequencies, we think that it is the leaky characteristic of the capacitor samples which masks the pinching on the P-E loops.

Corresponding leakage current measurements are shown in Figure 3.17. It seems to reveal the pinching even at low frequencies (i.e. 0.1 Hz). One may notice that the leakage current is very large (~ 10^{-3} A) at 0.1 Hz which confirms that the structures are leaky. In contrast, leakage current at 100 Hz is much lower (~ 10^{-6} A). This can be a feature of screen printed P(VDF-TrFE-CTFE) in contrast to P(VDF-TrFE) which exhibits larger leakage current of the order of 10^{-4} A even at higher frequency (1 kHz).

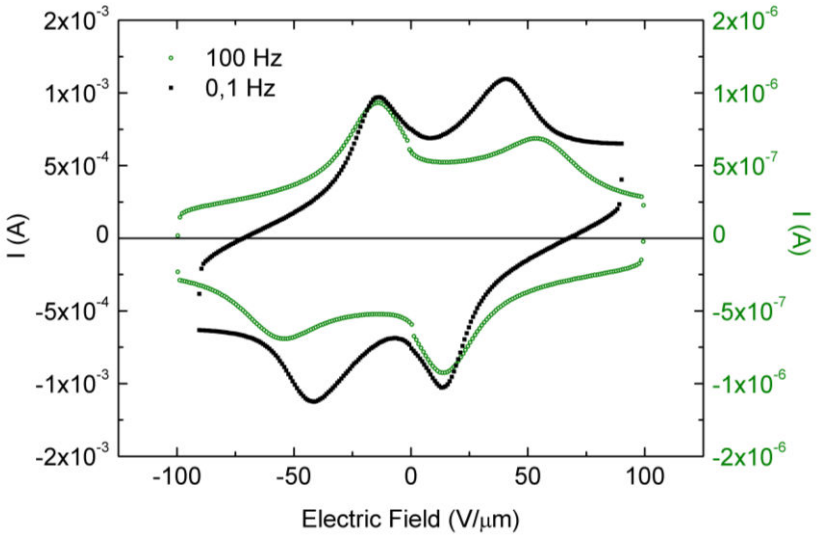

Figure 3.17. Leakage current densities at 0.1 Hz and 100 Hz vs. electric field of 2.2 μm screen printed P(VDF-TrFE-CTFE).

RE/FE heterostructures

Hysteresis loop measurements have to be undertaken carefully in order to avoid missing key features of such original multilayers. Indeed, classical ferroelectricity of screen printed P(VDF-TrFE) samples goes one way with frequency and pinched hysteresis of the P(VDF-TrFE-CTFE) capacitors goes the opposite way. Namely, it means that increasing frequency to observe RE pinched loops characteristics broaden those of FE because the coercive field increases. This is illustrated in Figure 3.18.

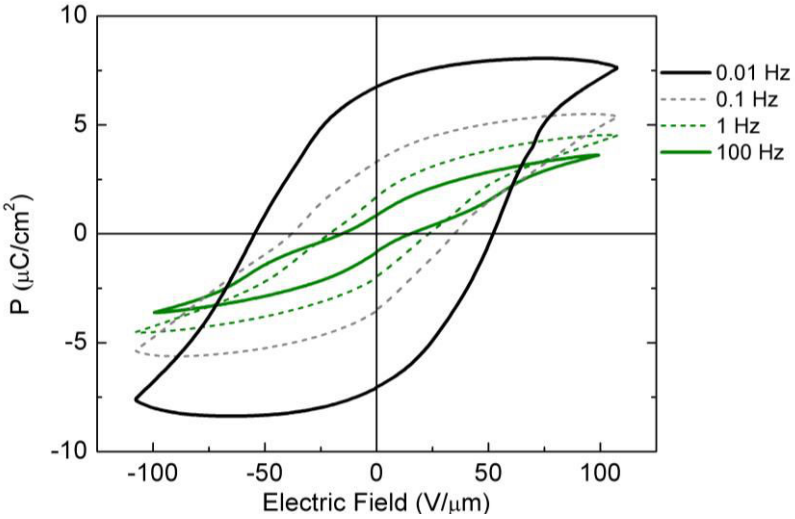

Figure 3.18. P-E hysteresis loop of screen printed heterostructure of P(VDF-TrFE) and P(VDF-TrFE-CTFE) for different frequencies (sample multi-P-1).

As expected, the heterostructure goes from leaky ferroelectric at low frequency (0.01 Hz) to pinched relaxor at high frequency (100 Hz), with visible decreases of P_r and E_c. At 0.01 Hz, P_r and E_c are equal to 6.7 μC/cm^2 and 50 V/μm respectively, which are close to those of copolymer samples. In particular, based on averaged measurements we may assume enhanced coercive field of ~ 25 to 30% compared to single layer of P(VDF-TrFE). At 100 Hz, these values approach those of single layers of P(VDF-TrFE-CTFE). It is an original feature with polymers. In addition, leakage current measurements are shown in Figure 3.19.

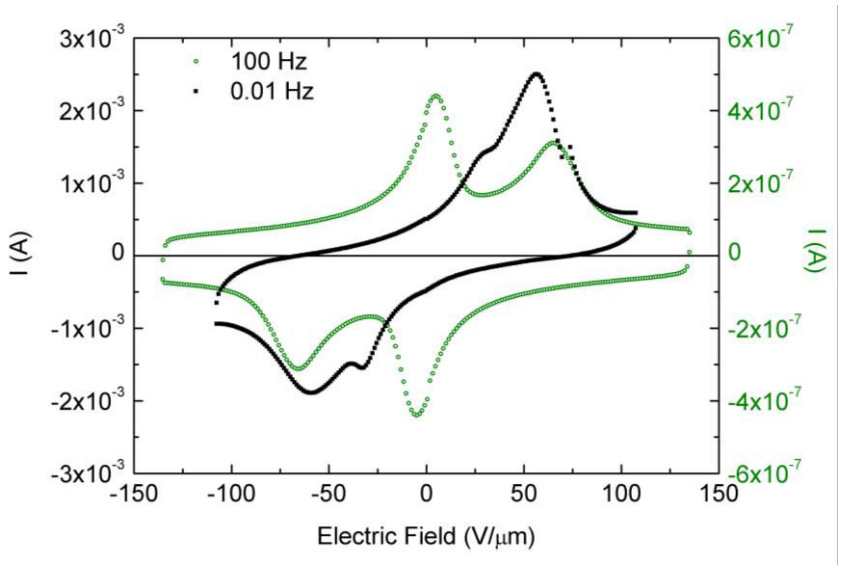

Figure 3.19. Leakage current densities of screen printed heterostructure of P(VDF-TrFE) and P(VDF-TrFE-CTFE) for different frequencies (sample multi-P-1).

The results presented here are the first experimental observations of such behavior with ink-based RE/FE polymer heterostructures, and further studies are necessary for a better understanding of this phenomenon.

3.5 Summary of electrical results

Table 3.1 summarizes the main ferroelectric characteristics of this work with relative permittivity ε_r, loss tangent tan δ, remanent polarization P_r and ferroelectric FE or antiferroelectric AFE order, valid for all samples with PEDOT:PSS. Average values are given, based on at least 5 samples.

As can be seen from the table, the achieved ε_r values for P(VDF-TrFE) and P(VDF-TrFE-CTFE) are consistent with literature data [111]. Higher values of ε_r and *tan* δ are confirmed with terpolymers. Heterostructures combining P(VDF-TrFE) and P(VDF-TrFE-CTFE) show intermediate values. Other elements are notable, among them: remarkable high P_r with P(VDF-TrFE) and pinched loops with P(VDF-TrFE-CTFE). In their case, remanent polarization and coercive field tend to zero.

Table 3.1. Summary of the ferroelectric properties of the screen printed materials of this work (with PEDOT:PSS). Relative permittivity and loss tangent values measured at 1 kHz.

Material	**ε_r**	**tan δ**	**P_r max [μC/cm^2]**	**Order**
P(VDF-TrFE)	9.3	0.03	7.5 @ 0.1 Hz	FE
P(VDF-TrFE-CTFE)	26.6	0.12	0.2 @ 10 Hz	RE pinched
Multilayers				
multi-P-1	15.5	0.05	-	RE pinched → FE
multi-P-2	15.1	0.09	-	RE pinched → FE
multi-P-3	20.0	0.06	-	RE pinched → FE
multi-P-4	11.0	0.07	-	RE pinched → FE
multi-P-5	12.3	0.04	-	RE pinched → FE

Special case of heterostructure capacitances

We have compared theoretical values of capacitance with experimental ones for heterostructure samples. Their multilayer structure can be electrically presented by capacitors connected in series (Figure 3.20). The total capacitance C_{total} can be calculated by serial capacitance equation (3.2), with C_{terpo} the capacitance of a single layer of P(VDF-TrFE-CTFE) and C_{copo} that of a single layer of P(VDF-TrFE). The interface capacitances $C_{interface}$ are also included.

$$\frac{1}{C_{total}} = \left(\frac{1}{C_{terpo}}\right) \cdot n + \frac{1}{C_{copo}} \cdot m + \frac{1}{C_{interface}} \cdot p \qquad (3.2)$$

where n is the number of terpolymer layers, m is the number of copolymer layers and p is the number of interfaces.

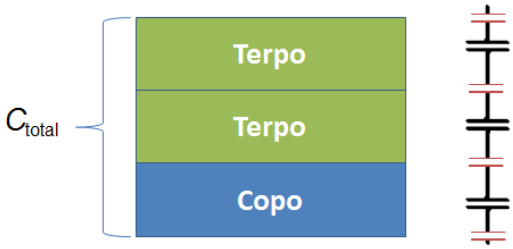

Figure 3.20. Electrical schematic representation of multilayer (sample multi-P-3) with material capacitors connected in series including interface capacitance (in red).

The calculation results are presented in Table 3.2. Theoretical and experimental values are in overall agreement. With regards to the accuracy of thickness measurement, which is better than 10%, we may note positive deviations between both values which are significant. First, this confirms the ability of the multilayer screen process to avoid dead layers or defective interfaces otherwise the deviations would be negative. Second, deviations of + 20% may be considered as an indication of subsidiary coupling between P(VDF-TrFE-CTFE) and P(VDF-TrFE), whose origin remains uncertain.

Table 3.2. Comparison of theoretical multilayer heterostructure capacitances (calculated without consideration of interface capacitance) with experimental values.

Sample	C_{total} theoretical, nF	C_{total} experimental, nF
multi-P-1	0.9	1.1
multi-P-2	0.9	1.0
multi-P-3	0.7	0.9
multi-P-4	0.5	0.5
multi-P-5	0.5	0.5

3.6 Conclusions

This chapter was devoted to the ferroelectric properties of the screen printed samples of P(VDF-TrFE) and, more exploratory, to those of P(VDF-TrFE-CTFE) and heterostructures of P(VDF-TrFE) and P(VDF-TrFE-CTFE). We first conclude on the successful fabrication of the capacitor test structures, including simple design for material study and more complete design with parallel connected capacitors for prototyping.

Two type of top electrode materials (Ag ink and PEDOT:PSS) were compared. Capacitors with PEDOT:PSS top electrode showed lower leakage current density and no electrical breakdown up to 400 V. In contrast, capacitor samples with Ag top electrode were leaky and deficient from 100 V. Therefore, it was concluded that PEDOT:PSS is the most suitable electrode material to continue this work.

Optimal polarization conditions were found for screen printed P(VDF-TrFE) copolymer leading to remarkable high P_r with 7.5 $\mu C/cm^2$ indicating high ferroelectric order (FE). At the opposite, screen printed P(VDF-TrFE-CTFE) terpolymer behaves as a relaxor (RE) showed weak P_r and pinched hysteresis.

A key result was the electrical confirmation of the achievement of multilayers by screen printing with no dead layer or deficient interfaces. Considering the exploration of RE/FE heterostructures of P(VDF-TrFE-CTFE) and P(VDF-TrFE), first time produced multilayers by screen printing were measured, showing good agreement with theoretical serial capacitance calculations. However, their ferroelectric behavior was complex due to the pinched loop characteristics of P(VDF-TrFE-CTFE) and a finer understanding of the phenomena involved in this RE/FE system is beyond the scope of this study.

Chapter 4. Piezoelectric properties

In order to choose the suitable piezoelectric material for energy harvesting applications, it's important to perform piezoelectric characterizations as close as possible to actual usage cases. Since the use of electroactive polymers has started recently in this field with the tremendous advantage of flexibility (also transparency), it's necessary to develop new technics suitable for highly flexible piezoelectric materials, which may differ from conventional methods used for ceramics. Thus, this chapter is devoted to the transition from screen printed ferroelectric capacitor test structures (Chapter 3) to true flexible piezoelectric (also pyro) microgenerators for mechanical/thermal energy harvesting (Chapter 5).

We have previously seen in Chapter 1, section 1.2 the state of the art of characterization techniques for polymers, focusing on the direct piezoelectric voltage and energy measurements. In this chapter we will report optimized characterization methods which were previously validated by us on commercial PVDF bulk films. Parallel to experimental measurements it is essential to perform theoretical estimations of the direct output voltage in order to compare it with the obtained results. Then, we will present the overall piezoelectric characteristics of our screen printed flexible microgenerators by these methods. Simple pyroelectric measurements will be also presented.

4.1 Materials and methods

We will first present two improved methods of measuring the direct piezoelectric voltage under applied mechanical stress. The first one uses a conventional oscilloscope and mechanical switch. The second one uses a non-contacting electrostatic voltmeter. Both methods allow open-circuit conditions avoiding external leakages into the measurement system not to affect evaluation piezoelectric voltage and energy. We will then describe the experimental methods to apply mechanical stress, such as water drop, tube bending and four-point bending. First, commercial grade, poled and metalized PVDF from Piezotech, with a thickness of 40 µm, was used for validation based on known piezoelectric coefficients.

4.1.1 Direct piezoelectric voltage measurements

Direct piezoelectric voltage measurement is realized by introducing a mechanical switch into the measurement circuit, which separates charge generation (when strain applies) from charge collection (when strain stops). The switch is kept in open state during the mechanical deformation while the produced charges accumulate in the capacitor structure. When the deformation is completed, the switch is closed and all the collected charges are transferred at once into the measurement circuit. A schematic representation of the used circuit is shown on Figure 4.1.

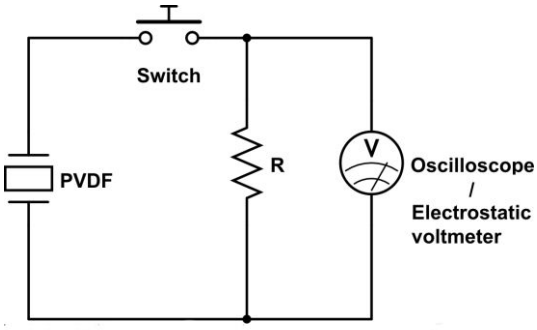

Figure 4.1. Schematic presentation of the switch measurement circuits with oscilloscope or non-contacting electrostatic voltmeter.

The output voltage was measured either with the oscilloscope Agilent Technologies DSO1014A (first method), or with the electrostatic voltmeter TREK 370 (second method). The latter measures the electrostatic surface potential of the sample without physical contact, making the impedance of such a system virtually infinite, thus eliminating the problem of load adaptation to the voltage measurement. Indeed, potential electrical leakage can and does take place at the oscilloscope load input. The measurement equipment is shown in Figure 4.2.

(a)

(b)

Figure 4.2. (a) oscilloscope Agilent Technologies DSO1014A, (b) non-contacting electrostatic voltmeter TREK 370.

Once the switch is closed (A) the sample discharges and one can observe the voltage rising from zero to a maximum value and then decay back to zero. The discharge takes place over a few tens of milliseconds (B) with PVDF as shown in Figure 4.3 with both the oscilloscope and the electrostatic voltmeter. The corresponding electrical energy U_{piezo} can be calculated from the time-dependent voltage across the load resistance R using equation (4.1) with integration limits from A (start of discharge) to B (end of discharge) :

$$U_{piezo} = \frac{1}{R}\int_{A}^{B} V^2 dt \tag{4.1}$$

Note that in case of the electrostatic voltmeter, the switch is not needed to realize the open-circuit condition. It is however used to discharge the generated voltage from the sample into the external load in order to calculate at the same time the produced electric energy.

The peak voltages measured with the proposed methods are 8 times higher compared to conventional oscilloscope measurements without a switch. The implications of this, and the results of the proposed methods will be discussed further in section 4.2.

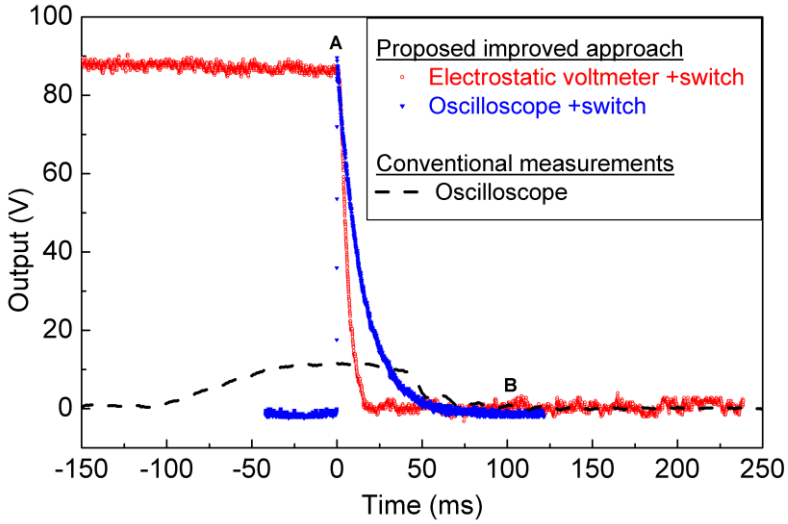

Figure 4.3. Examples of piezoelectric discharge of commercial grade PVDF using oscilloscope with switch, electrostatic voltmeter with switch, and comparison with conventional measurement (oscilloscope only).

4.1.2 Strain application

To perform direct piezoelectric characterization of new materials and structures it is necessary to apply well-controlled strain with great precision. For this purpose, three mechanical methods have been investigated and specially adapted for polymers.

Water drop experiment (3-3 mode)

As mentioned in the state of the art, one of the possibilities to apply repeatable strain to samples is to impact them with droplets of water (or fluids) equal in size and with known weight. To realize this set-up we have used a syringe pump from "kd Scientific". The syringe pump produces controlled drops which fell from a controlled height onto the sample surface which is clutched between two clamps. The transferred mechanical energy is equal to the kinetic energy of the drop (Figure 4.4). The weight of each drop m_d was $27.8 \cdot 10^{-6}$ kg ± 3%, estimated from drop rate, volume and water density. The distance (h) from the syringe to the sample was 9.3 cm. The kinetic energy of the drop at the impact (E_K) can be calculated as the potential energy of the drop when it leaves the syringe:

$$E_K = m_d \cdot g \cdot h \tag{4.2}$$

where g is the gravitational acceleration (9.8 [m/s^2]).

Figure 4.4. Schematic representation of water drop experiment (not to scale).

This simple experimental set-up allows measuring the produced piezoelectric voltage in 3-3 mode. Here, the PVDF sample was directly connected to the oscilloscope. Therefore the corresponding produced electric energy was calculated by the capacitor equation:

$$U_{piezo} = \frac{1}{2} \cdot C \cdot V^2 \tag{4.3}$$

Additionally, the electromechanical coupling coefficient (k_T^2) can be determined by dividing the produced electric energy by the input mechanical energy:

$$k_T^2 = \frac{U_{el}}{E_k} \tag{4.4}$$

Four-point bending (3-1 mode)

Next method was the conventional four-point bending system. This method allows to apply stress in 3-1 mode to the samples. In our work we used a tensile machine MTS RT5 Alliance with adapted 4-point bending set-up (Figure 4.5). To increase the induced strain in the PVDF samples, they were glued to a 1.1 mm thick Plexiglas substrate. The bending-induced stress is uniform between point a and b and can be calculated by following equation [112]:

$$\sigma = \frac{3 \cdot F(L - L_i)}{2 \cdot b \cdot d^2} \tag{4.5}$$

where F is the load [N], L is the length of the support span [m], L_i is the length of the loading span [m], b is the width [m], d is the substrate thickness [m].

It is a high precision repeatable method, but the deformation range was limited to 0.6% by set-up. Forces from 1 to 6 N were applied, measured by internal force sensor.

(a) (b)

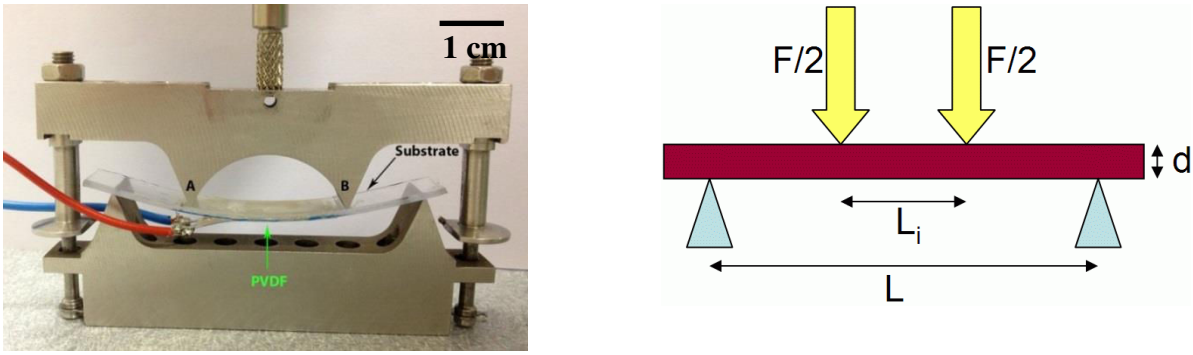

Figure 4.5. Four-point bending system: (a) experimental set-up, (b) schematic representation.

Tube bending (3-1 mode)

Another simple method of applying mechanical stress in 3-1 mode to flexible materials consists in tube bending, i.e. It is to bend manually the sample around a tube with known diameter. When using a substrate (much thicker than the piezoelectric layer), the induced linear strain away from the neutral fiber can be calculated by the equation (4.6) [29].

$$\varepsilon = \frac{h/2}{R + h/2} \tag{4.6}$$

where h is the substrate thickness, R is the tube radius [m].

This method is similar to four-point bending as it applies mechanical stress to the sample in 3-1 mode. But it can produce higher strain values, up to 1%, by decreasing the tube diameter. In this work we used tubes with diameters of 84, 50, 33.5, 29 and 22 mm.

4.1.3 Sample preparation

Two types of samples were used. For comparison with theoretical values, the first sample is based on the 40 µm-thick commercial grade PVDF from Piezotech. The four-point bending sample consists in small PVDF pieces of 1 x 1,5 cm^2 glued with Scotch-Weld™ Epoxy Adhesives glue on top of a 1.1 mm-thick Plexiglas plate. These samples will be further referred as “Piezo-40”. The second sample is based on the screen printed single capacitors (Design-1) of this work, prepared in a similar way. The back side of the PEN substrate was glued on the Plexiglas plate, and the connection between electrode pads and external wires was realized on the top side by means of silver paste and copper tape. A picture of a prepared sample is presented on Figure 4.6.

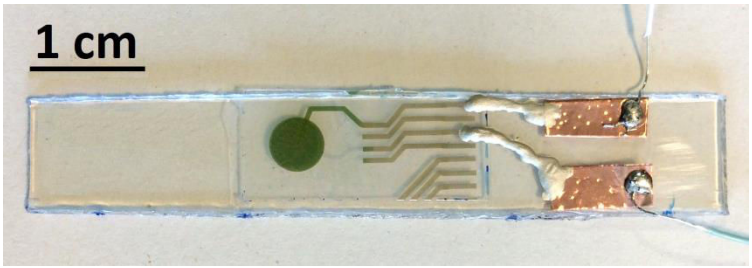

Figure 4.6. Single screen printed capacitor structures mounted on Plexiglas for four-point bending experiment.

The parallel connected capacitor structures (Design-2) could not be tested by four-point bending, due to size limitation. They were tested by tube bending without additional substrate in this case (Figure 4.7).

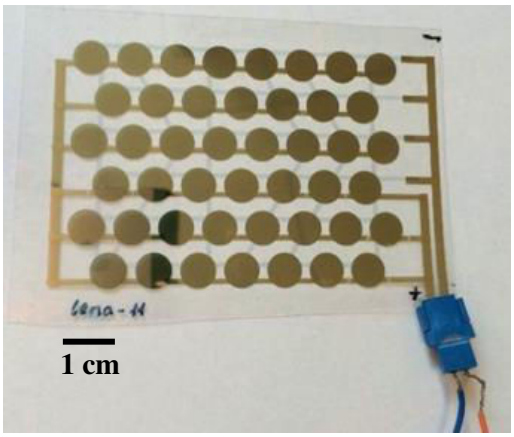

Figure 4.7. Screen printed parallel connected capacitor structures used for tube bending experiment (no additional substrate).

4.2 Results and discussion

4.2.1 Piezoelectric voltage

Commercial grade PVDF

Sample Piezo-40 was tested by water-drop, tube and 4-point bending in order to determine output voltage, g_{31} coefficient, and energy density in open-circuit conditions. These methods were compared in terms of piezoelectric response, repeatability of results and ease of use. Parallel to experimental measurements it is essential to perform theoretical estimations of the direct output voltage in order to compare it with the obtained results.

In the water-drop experiment the voltage produced per drop was 600 mV. Based on this, the coupling coefficient k_T was estimated at 0.26% with equation (4.4). Compared to data sheet value (10%) this result is very low, which can be due to difficulty in estimating the actual mechanical energy which is transferred to the sample (due to wetting phenomena, non-uniform shape of the drop). Also, it may be due to charge leakages in the measurement set-up as the "switch" method was not yet used. Therefore we turned to more appropriate

methods. However, the water-drop method can be used for real energy harvesting simulations with fluids such as rain.

Results of four-point bending and tube experiment with the Piezo-40 sample are shown in Figure 4.8, where the piezoelectric output voltage is reported as a function of strain. Experimental results are compared with theoretical ones calculated by equation (1.6) based on Piezotech data sheet. As can be seen from this graph, both methods are complementary and have a good match with repeatable results.

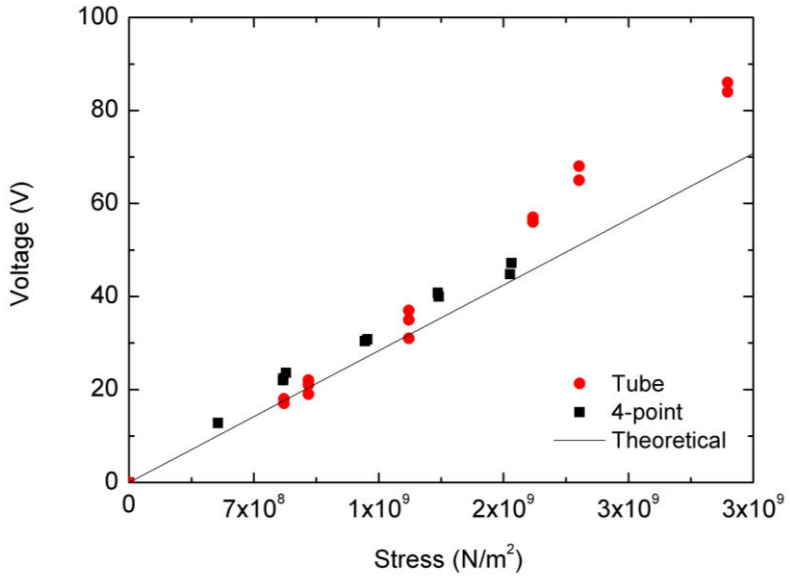

Figure 4.8. Piezoelectric output voltage of commercial grade PVDF (40 µm) from Piezotech based on four-point bending and tube bending in open-circuit condition. Solid line is theoretical from data sheet characteristics.

The tube method is simpler to realize and leads to larger strain (1%) and it is possible to characterize samples of various sizes, but it is less precise and reproducible. On the other hand, the four-point bending method is automatized, shows higher repeatability, and applies deformation more uniformly, but strain is limited here to 0.5%. Whatever the method, we achieved in open-circuit conditions superior results than those of the literature. For instance, with the Piezo-40 sample, we report a record value of 80 V at 1% of strain, which is the highest observed piezoelectric voltage in the literature with PVDF-based material.

To pursue it is more practical to switch for stress, thereby calculate g_{31}. One switches from strain to stress by multiplying the former by the Young's modulus.

The experimental results present a good match with theoretical calculations which means that both methods are suitable for piezoelectric characterization and therefore can be used for accurate estimation of g_{31} coefficient. There is a slight difference of the voltage around few volts, which can be explained by the precision of strain calculation and precision of values in the data sheet (± 20%).

Screen printed P(VDF-TrFE): single capacitors (Design-1)

The screen printed P(VDF-TrFE) single capacitors samples (Design-1) were extensively tested in their turn with the four-point bending method. Various thicknesses of P(VDF-TrFE) layers were characterized, between 1.3 and 3.9 µm. Figure 4.9 shows the open-circuit piezoelectric voltage as a function of stress.

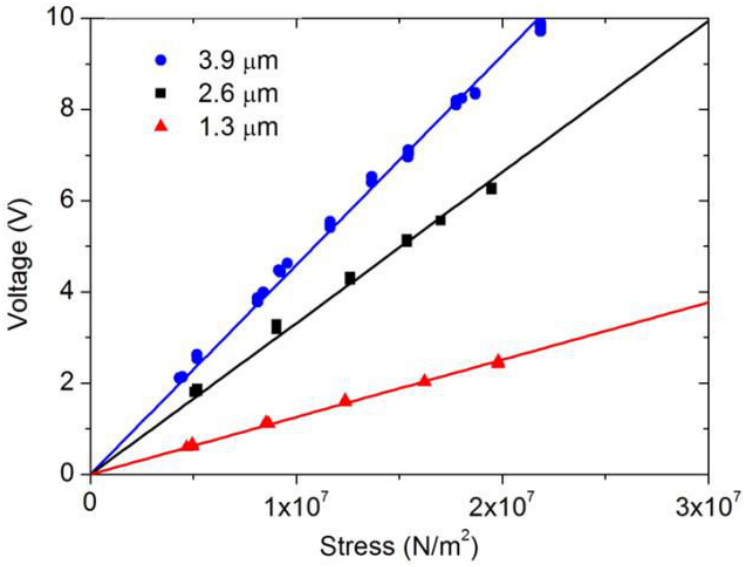

Figure 4.9. Piezoelectric output voltage of the screen printed P(VDF-TrFE) single capacitor, obtained by four-point bending in open-circuit condition for various thicknesses.

These dependences present linear behaviors. Thicker films produce higher voltage in agreement with equation (1.5), which presents theoretical output voltage for piezoelectric materials. The corresponding g_{31} voltage coefficients were further calculated

Screen printed P(VDF-TrFE): parallel connected capacitors (Design-2)

The experiment was pursued using tube bending with full screen printed P(VDF-TrFE) parallel connected capacitors samples (Design-2), because their size was too big for the

four-point bending system. The stress-voltage dependence for the 2.6 µm-thick sample is shown in Figure 4.10. As a result, the parallel connected capacitors still present a linear behavior similar to single capacitor structures which is an indication of the mastery of the deposition process at larger scale.

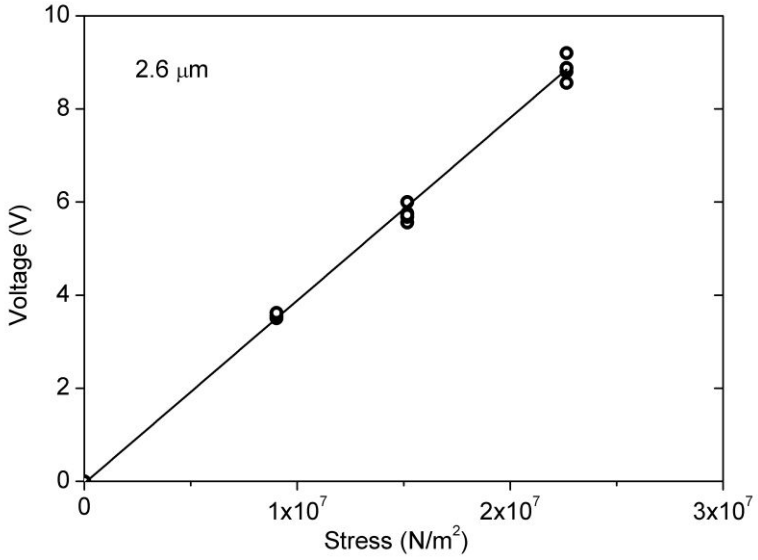

Figure 4.10. Piezoelectric voltage as a function of applied stress for the screen printed P(VDF-TrFE) parallel connected microgenerators with 2.6 µm thickness.

Similar to single microgenerators, the voltage presents linear behavior for the parallel connected structure. Voltages up to 9 V were obtained, which is remarkably high value for thin film P(VDF-TrFE).

4.2.2 Piezoelectric coefficient (g_{31})

The stress-voltage dependences are linear in agreement with the piezoelectric equation (1.5). The piezoelectric voltage coefficient g_{31} can then be calculated from this dependence by the following equation:

$$g_{31} = \frac{V}{\sigma \cdot t} \tag{4.7}$$

where V is the piezoelectric voltage, σ is the applied stress and t is the P(VDF-TrFE) thickness.

The direct g_{31} coefficient is given for screen printed P(VDF-TrFE) films in Table 4.1. To our knowledge, this has never been reported yet. Here we find g_{31} value of 0.12 V·m/N, which is markedly superior to that of commercial "bulk" films, which show 0.06 V·m/N [111]. This confirms that the proposed fabrication method and polarization conditions are beneficial for producing high-performance P(VDF-TrFE) thin film microgenerators. One should however mention that single layers of P(VDF-TrFE) exhibit a slightly lower value of g_{31} than thicker films. We believe this is due to minor fabrication defects noticeable at 1.3 µm thickness (discussed in Chapter 3). As neither dielectric nor ferroelectric properties show a significant change with film thickness, we assume these defects may mainly affect mechanical properties (i.e. Young's modulus) and indirectly piezoelectric characteristics according to equation (4.7). Equivalent values of g_{31} for thicker films indicate that the problem of single layer deposition is solved with the multilayer process. Network structures reached g_{31} value of 0.15 V·m/N, which is slightly higher than for single films, possible due to increased capacitance thus lower leakage.

Table 4.1. Experimental g_{31} voltage coefficient of screen printed P(VDF-TrFE) thin films, and *extrapolated datasheet value for 12 µm*-thick P(VDF-TrFE) 75/25 film for comparison.

Sample	**1.3 µm**	**2.6 µm**	**3.9 µm**	**Network 2.6 µm**	**Datasheet**
g_{31} (V·m/N)	0.10	0.12	0.12	0.15	0.06 [111]

4.2.3 Piezoelectric energy density

Based on experimentally obtained voltage, energy density values were calculated by dividing the energy values (from equation (4.1)) by the microgenerator piezoelectric layer volume. The piezoelectric energy density as a function of applied strain for single microgenerators is presented in Figure 4.11. All experimental values are in good agreement with a square law (i.e. $\propto V^2$) over a broad range of strains. The energy density reaches a high value of 275 µJ/cm^3 at 0.75% strain, which is in our case only an experimental limitation of the four-point bending equipment. Higher energy densities will be possible with larger strain within the elastic domain. Consistently with reported voltages, the single layer sample shows slightly lower values of energy density (~ 150 µJ/cm^3 at 0.7% strain), certainly due to different mechanical characteristics.

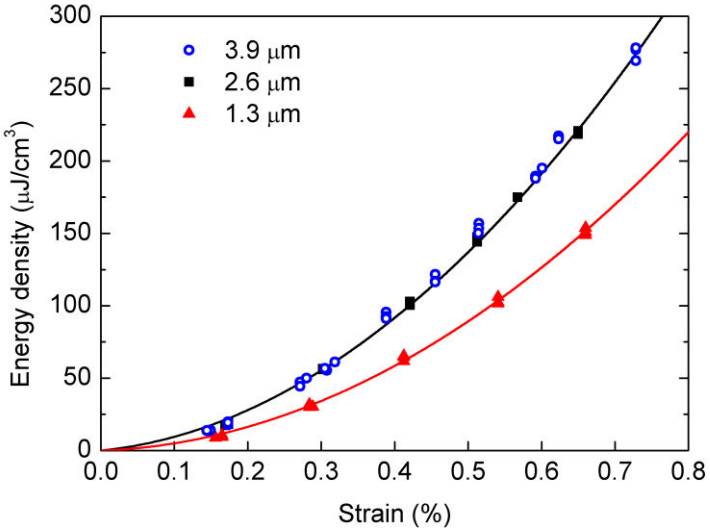

Figure 4.11. Energy density values under applied strain for screen printed P(VDF-TrFE) single microgenerators with various thicknesses.

Even though single microgenerators are able to produce quite high energy density values, the produced energy is rather small (maximum 50 nJ) because of their small volume. That is why for actual applications we will use microgenerator networks, which can produce up to 2.5 μJ at 0.4% of strain (Figure 4.12). The strain was limited here by the experimental set-up of tube bending, as it was not possible to bend such a big structure on smaller diameters. The obtained energy corresponded to the remarkably high value of energy density of 480 μJ/cm^3.

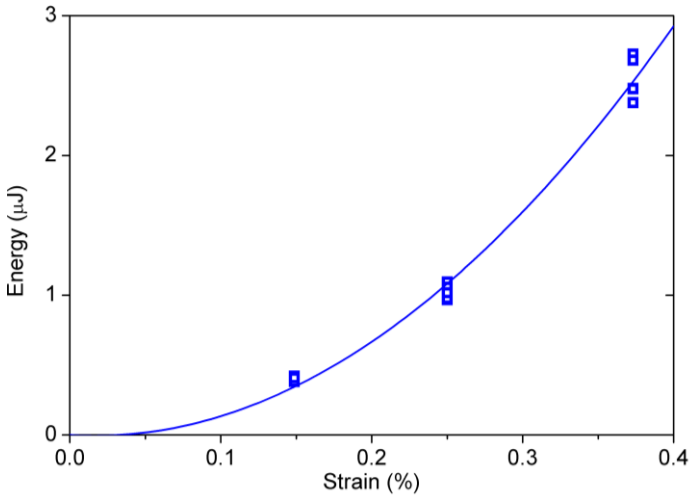

Figure 4.12. Energy as a function of strain for the screen printed P(VDF-TrFE) parallel connected microgenerators.

The obtained results demonstrate that flexible screen printed P(VDF-TrFE) microgenerators are competitive with other generators [113]. They can potentially produce hundreds of μJ when extended to letter-sized substrate, which is possible with industrial screen printing processes. These values are compatible with numerous wireless applications, such as IoT (Internet of Things) requiring indicative power of 10 to 100 μW (or μJ/s). This makes screen printed P(VDF-TrFE) microgenerators a promising solution for bendable or stretchable energy harvesters with high-deformation functional materials such as giant magnetostrictive [114] or shape memory alloys [34], [57].

4.2.4 Pyroelectric measurements

The final objective is to harvest thermal energy on heating (and cooling). It is therefore important to investigate the intrinsic pyroelectric behavior of the screen printed P(VDF-TrFE) parallel connected microgenerators as pyroelectricity will participate to the voltage at the end. To do so we have heated the samples at different temperatures and measured the produced pyroelectric voltage. Heating was realized in air in a conventional oven, and voltage was measured in open-circuit with the electrostatic voltmeter. The results are presented in Figure 4.13.

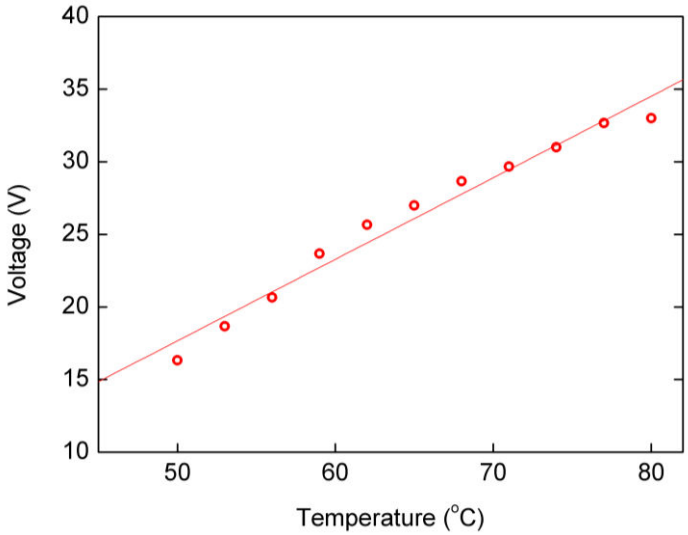

Figure 4.13. Pyroelectric voltage as a function of temperature for the screen printed P(VDF-TrFE) parallel connected microgenerators of 2.6 μm thickness.

According to the theory all measured pyroelectric voltage was negative, but for easier reading and interpretation it was plotted in positive values.

From the measured voltage the pyroelectric charge coefficient ρ_Q was calculated to be -25 μC/K·m^2 using the following equation:

$$\rho_Q = \frac{V \cdot \varepsilon}{\Delta T \cdot t} \tag{4.8}$$

where V is the pyroelectric voltage [V], ε is the permittivity [$C/V \cdot m$], ΔT is the temperature change [K] and t is the thickness [m].

This experimental value is in a good agreement with datasheet value for P(VDF-TrFE) (-20 ± 25% μC/K·m^2 [111]).

The importance of these measurements will come further in Chapter 5, where our composites will be tested under 65 ºC, which is the working temperature of the shape memory alloy element used. At this temperature a produced pyroelectric voltage of 25 V will be considered for overall output of the composite.

4.3 Conclusion

Based on original piezoelectric measurements, backed by calculations, we can conclude this chapter with key results for the screen printed P(VDF-TrFE) microgenerators of this work.

First, different methods of strain application for highly flexible materials were proposed and tested. The four-point and tube bending methods were chosen as the most appropriate. The validation was achieved with known commercial grade PVDF leading to good repeatability, and agreement with theoretical values.

Second, improved methods for direct piezoelectric voltage measurements in open-circuit conditions were proposed using non-contacting electrostatic voltmeter and/or mechanical switch (and oscilloscope). The methods were proven to give reliable results. As a result we report an outstanding value of the maximum piezoelectric voltage for PVDF commercial grade material with 80 V at 1% of strain. The methods also allow direct evaluation of the piezoelectric g_{31} coefficient which can be calculated from the observed strain-voltage dependence. The value was established at 0.07 V·m/N ± 15% for PVDF commercial grade material while datasheet indicates 0.06 ± 20% V·m/N (indirect method).

Another major key income of this chapter was the evaluation of g_{31} for screen printed P(VDF-TrFE) thin films, what is shown for the first time. The reported value is 0.15 V·m/N. It is twice the value of commercial grade P(VDF-TrFE) materials. Thanks to this high coefficient, the screen printed P(VDF-TrFE) microgenerators were able to produce strain-induced voltage up to 10 V at 0.4% strain which corresponds to an energy density of 480 μJ/cm^3, limited here by experimental conditions only. Higher energy densities are possible with applying larger strains.

Additionally, direct pyroelectric characterization of the screen printed P(VDF-TrFE) microgenerators was performed. A pyroelectric coefficient ρ_Q of -25 μC/K·m^2 was measured, in good agreement with datasheet.

Therefore, this important chapter ends with positive elements of decision for the targeted application of thermal energy harvesting based on the successful fabrication of high efficiency flexible screen printed P(VDF-TrFE) piezo- and pyro- microgenerators.

Chapter 5. Prospective works

Chapter 5 is a forward-looking approach of the application purpose of this work. The aim is to propose and discuss two aspects for the manufacture of a complete IoT sensor later and optimizing its performances. The first aspect relates to the composite approach with thermal shape memory alloy (SMA), originally proposed by our group [56], to achieve a high-efficiency thermal piezoelectric flexible harvester. Energy collected by the harvester and energy consumed by the indispensable radio system are then discussed in this context. The second aspect relates to the enhancement of the piezoelectric properties of screen printed P(VDF-TrFE) by nanoimprint. The technological part is challenging and only preliminary results will be shown. They establish the direction to follow later.

We present below the detailed composite prototype structure using the credit card format parallel connected microgenerators and with a commercial sheet of SMA. The functional tests validated the relevance of this concept. They show higher voltage and energy outputs than those of the single piezo- or pyroelectric microgenerators. Therefore, it results in enhanced properties by means of a multi-physical principle behind the composite scheme.

5.1 Flexible composite thermal harvester

5.1.1 Principle (multi-physical)

In this part we present the electrical results of the very first fully-flexible composite thermal energy harvester. The composite structure consists of screen printed P(VDF-TrFE) and thermal shape memory alloy (SMA). The mechanical coupling with the SMA element allows promoting crossed pyro and piezoelectric response from a unique thermal source. This contrasts with the single piezo- or pyroelectric microgenerators which can benefit from additional effects (pyro + piezo) only when the two appropriate sources are present (thermal + mechanical). The principle of crossed properties is illustrated on Figure 5.1 in analogy with that of multiferroic composite materials [115]. In this way, we may say that the composite of

this work belongs to the classification of multiferroics as it involves a double ferroic character, namely: ferroelectric and shape memory effects.

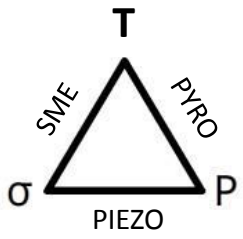

Figure 5.1. Schematic illustrating different types of coupling present in the composite.

5.1.2 SMA (short reminder)

Before we proceed, we remind practical SMA working principle. An excellent introduction is given in [116] and we will provide some citation from this work.

SMA are known to recover permanent strains when they are heated above a certain temperature going from two stable phases - the high-temperature phase, called austenite and the low-temperature phase, called martensite.

However pre-strain is essential. Indeed, martensite can be in one of two forms: twinned (self-accommodated) when unstrained and detwinned when pre-strained in the cold state. Without loading no observable macroscopic shape change occurs. The two cases are illustrated in Figure 5.2. where the characteristic starting and finishing temperatures for both phases are reminded.

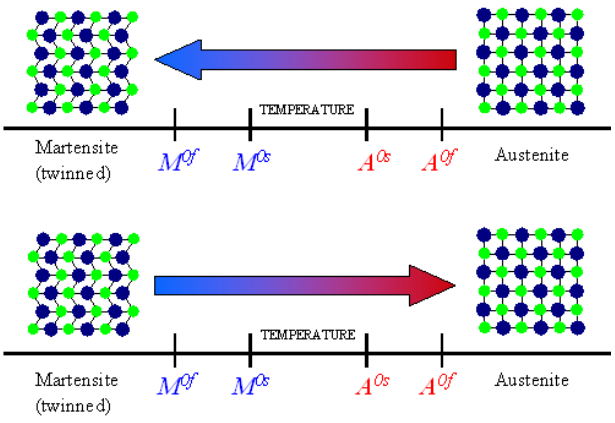

Figure 5.2. Temperature-induced phase transformation of an SMA without mechanical loading [116].

Therefore a mechanical load is required to detwin the martensite phase. When the load is released, the material remains deformed (pre-strained) and can undergo complete shape recovery when heating above A0f. Besides composition, the transformation temperatures can be changed by adjusting the applied load, as shown in Figure 5.3.

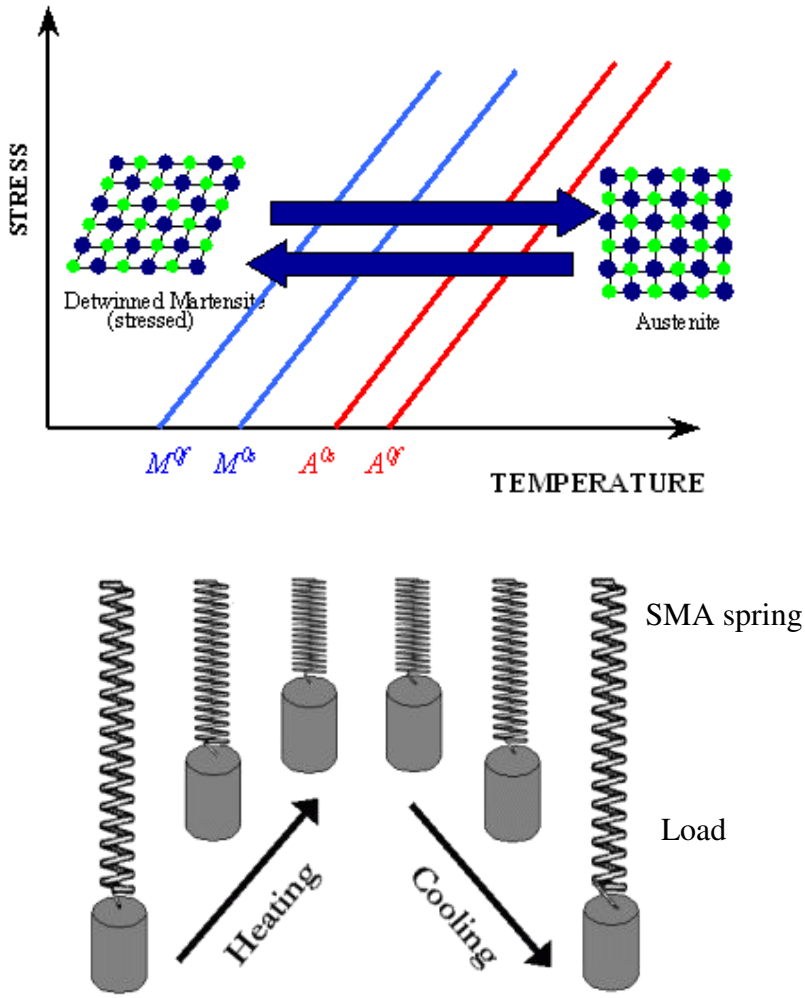

Figure 5.3. Temperature-induced phase transformation with applied load [116].

Among SMA alloys, mainly copper-aluminium-nickel and nickel-titanium (NiTi) alloys are used. Nitinol is preferable for most applications due to its stability, practicability and superior thermo-mechanic performance. Also, it offers a broad range of working temperatures from -20 °C to more than +100 °C, adjustable by composition and loading.

Table 5.1.Typical Properties of Nitinol [117].

Common Name	A^{0s} [°C]	A^{0f} [°C]	Description
N	-20 to -5	0 to 20	High Nickel Super Elastic Nitinol
S	-5 to 15	10 to 20	Super Elastic Nitinol
C	-20 to -5	0 to 10	Chromium Doped Super Elastic Nitinol
B	15 to 45	20 to 40	Body Temperature Nitinol
M	45 to 95	45 to 95	Mid Temperature Range Nitinol
H	>95	95 to 115	High Temperature Range Nitinol

5.1.3 Materials and methods

Materials

Two main SMA materials suppliers were identified in the context of this work. One is NIMESIS, France [118]. This company mainly provides NiTi-based wires with different diameters (0.1 to 2 mm). With regards to our demonstration purpose, larger SMA elements were preferred. They were provided by MEMRY, Germany [119] in the form of sheets (100 µm thick), from which credit card format elements can be easily cut.

The flexible composite prototype was made by assembling the two elements on the basis of the credit card format. The first element is the screen printed parallel connected microgenerator with 2.6 µm thick P(VDF-TrFE) layer. The second element is a MEMRY commercial grade 100 µm thick NiTi sheet with working temperature of 65 ºC. It was glued on the back side of the PEN substrate of the microgenerator with epoxy glue. This glue was chosen because it exhibits a high maximum shear strain which is compatible with our application [120]. Additionally, it can dry at room temperature which is an important requisite to stay below that of the hot state of the SMA (65°C). Prior to gluing, both elements were wiped and cleaned with isopropanol. Then the glue was applied on both surfaces, followed by pressing the surfaces together. In order to dry the glue completely, the composite was kept inside the press for at least 24 hours at room temperature. The final composite is shown in Figure 5.4.

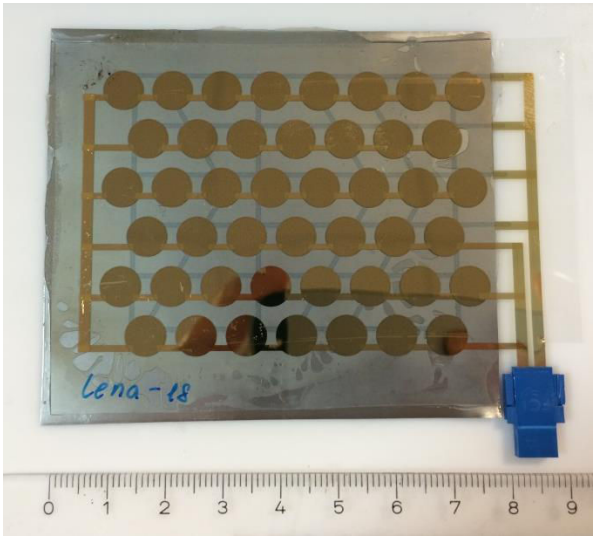

Figure 5.4. Photo of the flexible thermal composite (credit card format). Screen printed P(VDF-TrFE) microgenerators are visible on top, and NiTi sheet is visible by transparency.

Controlled heating

To evaluate the prepared composites and observe the impact of the addition of the SMA layer, it was necessary to heat the samples at the working temperature of the SMA, in a well-controlled and measurable manner. Several methods were experienced by our group, including electric current heating [121], water/oil thermostatic bath heating [122] and airflow heating [123]. Each method has its own benefits and disadvantages, and may be used depending on the working conditions and composite configuration. Here we used the airflow method in order to be closer to real application environment (heat flux). It produced reproducible results.

To generate airflow of 65 ºC, a conventional hairdryer was used. It was initially preheated during 5 seconds, and then placed over the sample at the distance of 20 cm and hold for 10 seconds to reach homogenous temperature distribution. The airflow was applied to the microgenerator side of the composite.

Pre-strain of SMA

As reminded, SMA requires to be pre-strained in the cold state (martensite) to experience the thermally-induced transformation. Here, to induce the pre-strain the tube bending method was used (as described in Chapter 4). We used tubes of 84 mm and 50 mm

diameters around which the composite was bent (SMA faced-down). Then, upon heating, it would return into its initial state (flat), thus producing enhanced piezo/pyroelectric voltage (

Figure 5.5). For the purpose of the simplicity of the electrical demonstration, the composite would experience here only one way transformation. This situation applies for thermal safety applications (temperature threshold indicator) where the safety element must be used once. To use reversible thermally-induced transformations and further to go towards thermal cycling energy harvesting (heating and cooling), the composite needs a restoring force (spring effect) to bring it back to the pre-strained cold state. This was demonstrated in [61]. Respective stiffness and thicknesses of the SMA and microgenerator substrate can be optimized to favor the spring effect of the substrate. When in-plane deformations are preferred, pre-strain can be applied using a tensile strain e.g. a tensile machine, but special clamps and procedure would be required with the large samples of this work. Alternatively, two-way SMA can be used, which does not need an external restoring force to return to the pre-strained cold state.

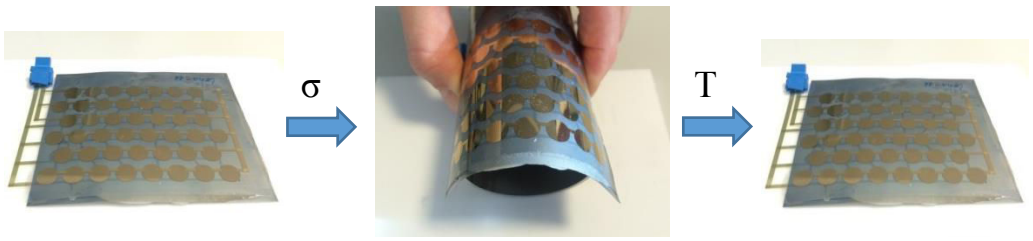

Figure 5.5. Flexible thermal composite operation scheme. Composite is pre-strained by tube bending at room temperature, then heated and recovered its initial state.

Voltage measurement

To measure the produced crossed-voltage with the composite structure, we used the oscilloscope with the switch, as described in Chapter 4. However, different contributions to voltage had to be separated:

- pyroelectric voltage is measured with the unstrained composite by simply heating the sample with airflow, while keeping the switch open. Upon 10 s of heating, the switch is closed and voltage peak is recorded.

- piezoelectric voltage is measured by tube bending of the composite at room temperature. The switch is kept open during the bending, and closed once the bending is completed.

- combined pyro/piezoelectric voltage: to benefit from the thermally-induced transformation of the SMA element, the composite is pre-strained (tensile) by tube bending and discharged. Then the exact procedure for the pyroelectric case is repeated. During heating the composite undergoes combined effects from piezoelectric (shape recovering, compressive) and pyroelectric properties and produces enhanced voltage. It is worth mentioning that both voltages are negative in the experiment and sum up. A schematic is shown in Figure 5.6.

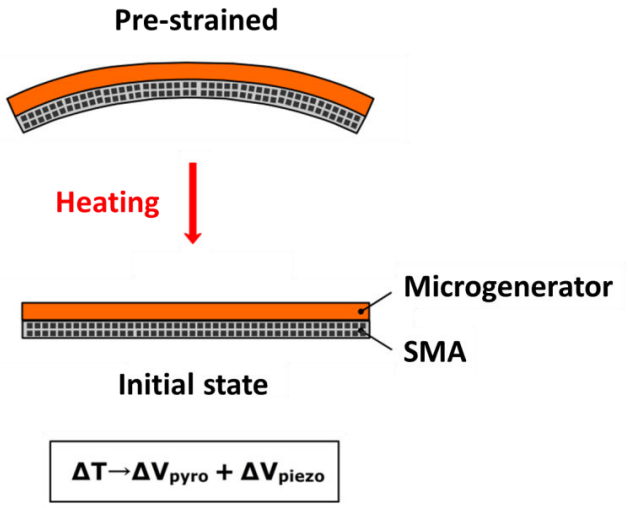

Figure 5.6. Schematic of SMA + piezoelectric composite functioning.

5.1.4 Electrical results

The measured voltage peaks of piezoelectric, pyroelectric and composite output are shown Figure 5.7 (drawn in positive values for easy reading). Maximum piezoelectric voltage was measured at 12 V at 0.56% strain (9 V at 0.33%). In its turn, the pyroelectric maximum voltage was evaluated at 26 V at 65 ºC. Finally, the composite voltage output reached up to 37 V with 0.56% and 65 ºC, which is almost a sum of both piezo- and pyro effect (the difference lies inside the measurement error interval which is ±10% here). This clearly illustrates the combination of two effects.

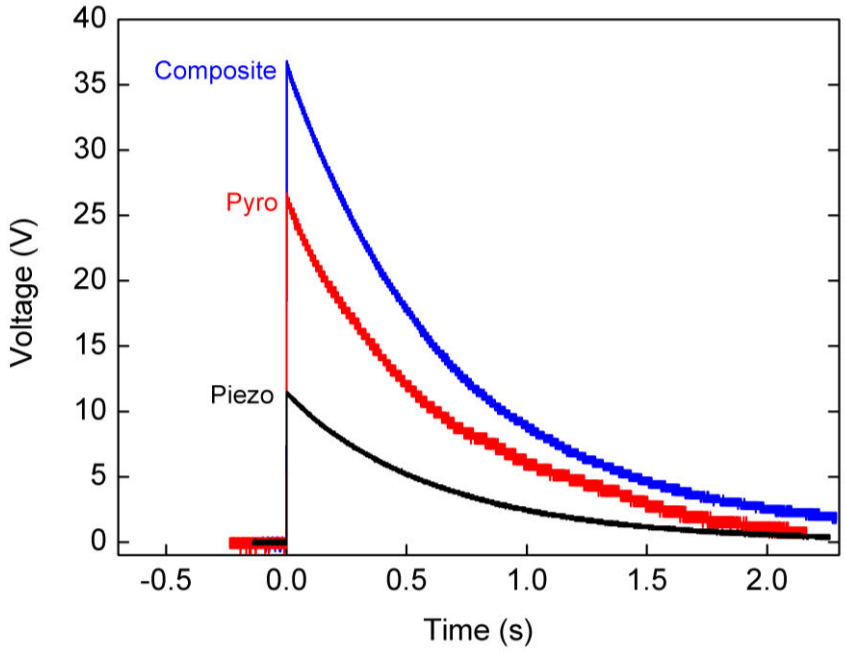

Figure 5.7. Piezoelectric, pyroelectric and combined voltages vs. time of the flexible thermal composite. Piezoelectric measurement performed at room temperature with 0.56% strain, pyroelectric measurement performed at 65 ºC unstrained and crossed piezo/pyro measurement performed at 65 ºC pre-strained (equivalent 0.56% strain).

As mentioned in our previous work [61], in order to be effective the composite must be designed in such way as to provide the same sign of output voltage according to pyroelectric (negative for ceramics and polymers) and piezoelectric (opposite sign for ceramics and polymers) material coefficients.

In Figure 5.8 the voltage output of three effects is shown as a function of applied strain. The pyroelectric voltage does not depend on the strain, so it is represented by a horizontal line at 26 V corresponding to 65 ºC. In turn, the piezoelectric voltage linearly increases with strain, in accordance with theory. Finally, the composite voltage increases with strain parallel to piezoelectric voltage with a positive shift equal to the pyroelectric contribution.

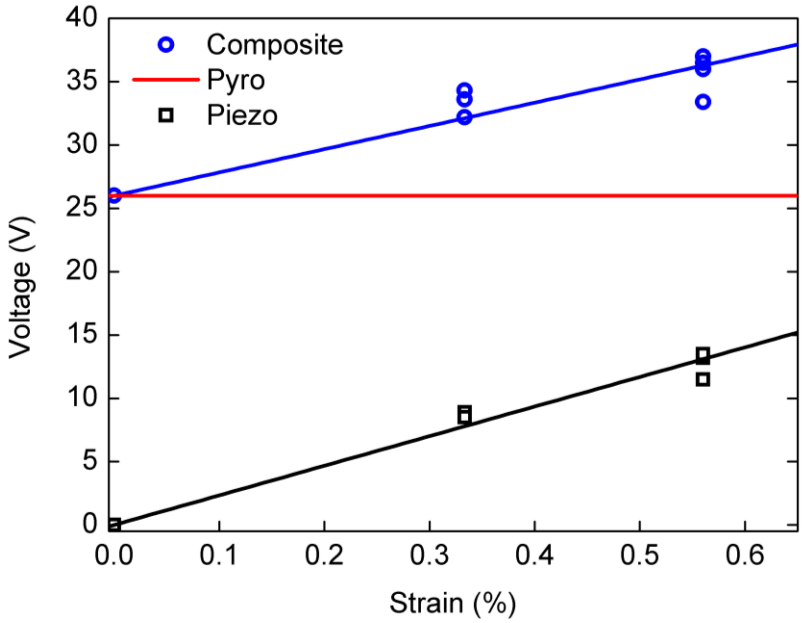

Figure 5.8. Piezoelectric, pyroelectric and combined voltages vs. strain of the flexible thermal composite. Piezoelectric measurement performed at room temperature with 0.56% strain, pyroelectric measurement performed at 65 ºC unstrained and crossed piezo/pyro measurement performed at 65 ºC pre-strained (equivalent 0.56% strain).

These results validate the concept of the proposed flexible composite prototype for easy thermal energy harvesting (no need of cold source management or radiator) made by assembling screen printed P(VDF-TrFE) microgenerators and NiTi on a credit card format. Now, to complement voltage, energy must be considered.

5.1.5 IoT Energy issues

IoT power requirements

Figure 5.9 gives an overview of typical power consumed by modern CMOS electronic devices. GSM has typically 1 W power consumption while at the opposite end RFID tags consume around 10 µW. These numbers are approximate and it is difficult to give average energy values to compare, since they are very different and depend on the system design and communication protocols.

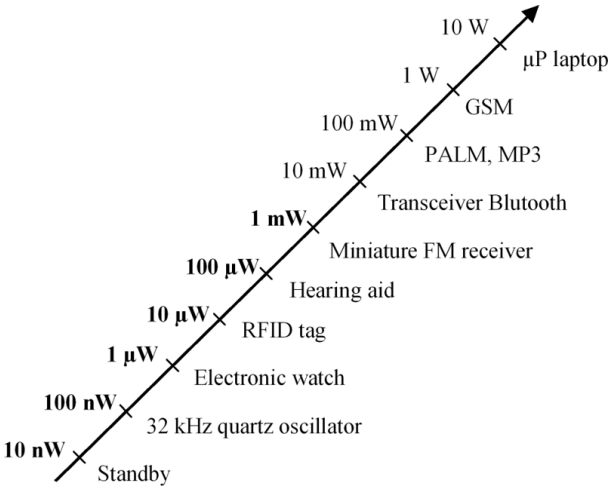

Figure 5.9. Powers consumed by CMOS electronic devices [59].

In [124], the picture for IoT wireless connectivity technologies was recently drawn from the three major operators today: the Wi-Fi Alliance, the Bluetooth Special Interest Group (SIG) and the ZigBee Alliance.

- Wi-Fi is present in all laptops, tablets, smartphones, and operates at 2.4 GHz or 5 GHz. It is high power consuming and remains mainly battery-operated.

- Bluetooth is also very popular with mobile phones and their equipment (headsets, car kits, speakers etc.). It operates at 2.4 GHz, often at short distances. It is fairly low power and can be powered by small rechargeable batteries or alkaline batteries. The recent Bluetooth Low Energy protocol was developed for low data throughput applications such as sensors. Its power consumption is significantly reduced and can be powered with small coin cell batteries or energy harvesting systems today. It enables new applications for health and fitness, toys, automotive and working spaces.

- ZigBee is in contrast a low-throughput, low-power and low-cost technology. It operates at 868 MHz, 915 MHz or 2.4 GHz. A very popular example is smart lighting where multiple lights form a mesh network in large buildings, called ZigBee® Light (Figure 5.10).

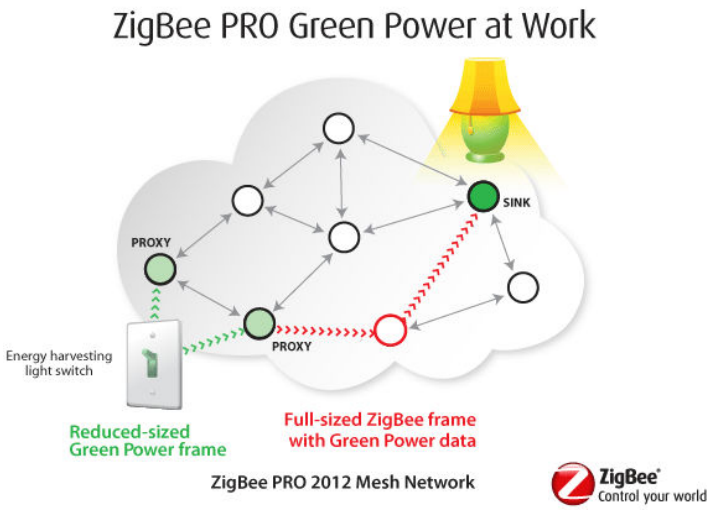

Figure 5.10. ZigBee® Light smart mesh schematic [125]

Today, ZigBee Alliance with 2012 ZigBee PRO Green Power has strengthened its leadership position as the global standard for wireless sensor and control networks and the Internet of Things with the IEEE 802.15.4 standard. It is particularly suitable for battery-less devices such as sensors, switches, dimmers and many other devices. It will help to connect energy harvesters with self-powered devices for industrial, lightning or home network applications which may comprise thousands of devices. According to ZigBee Alliance, we may compare two significant numbers for energy: Wi-Fi in a laptop consumes 2 kJ/hour while the Green Power in a light switch only consumes 200 µJ/hour. Always according to ZigBee Alliance, the smallest power constraint is 10 mJ with always powered, low duty cycle, deep sleep sensors, while it is 200 µJ when only powered upon user action (switch). The switch-based operating harvesters developed by our group were shown efficient to power ZigBee PRO Green Power from 100 µJ to 300 µJ, with Enerbee harvesters as a best example [126]. Figure 5.11 summarizes the main wireless characteristics for IoT.

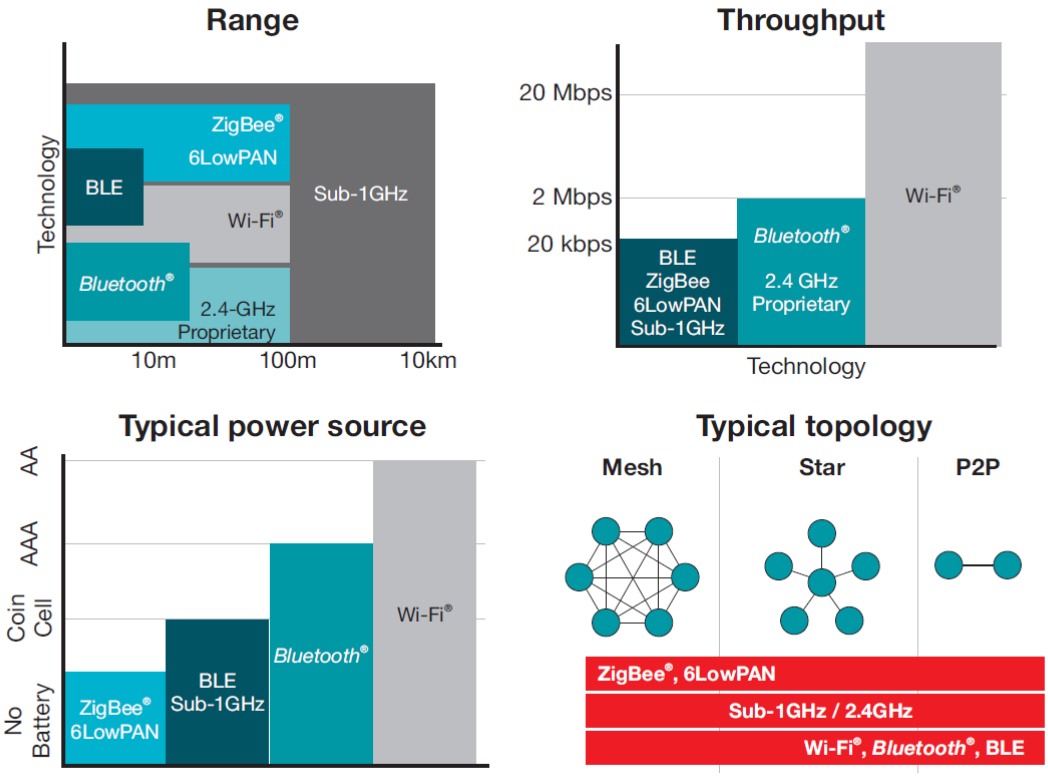

Figure 5.11. Summary of wireless technology parameters [124].

Facing requirements

We can now evaluate the energy collected by our composite harvester and matching these requirements according to size. Energy was calculated by integrating the voltage discharge peaks (equation (4.1)). The energy from pure pyroelectric effect was of 45 µJ at 65°C ; the energy from pure piezoelectric effect was of 10 µJ at 0.56% strain; the composite produced almost 10 times higher energy and reached 95 µJ with the same strain and heating at 65 ºC. This corresponds to composite energy density of 19 mJ/cm^3, which is a remarkably high value. Therefore, we are able to conclude that the credit-card format (8.5 x 5.5 cm^2) of this work is situated at the lower limit of power requirement for ZigBee Green Power with ~ 100µJ which is a decisive result, while optimizations have not been performed yet. For example, the same composite using two "head-to-tail" layers of screen printed microgenerators on either side of the SMA element [127] can produce ~ 200 µJ. Now, moving up to A4 format (21 x 29.7 cm^2) fabrication, these numbers can be multiplied by 13 which means that mJ-range energy can be generated, enabling the use of Bluetooth Low Energy protocol.

5.2 Building blocks for a thermal IoT sensor

A thermal IoT sensor would be able to detect and send encoded information that a thermal event took place, for examples: a critical high temperature threshold in an electrical box or the storage temperature of frozen or fresh products. To add the communicating sensor function to the thermal composite harvester we need to power a wireless transceiver.

Here, we base this analysis on the use of Texas Instrument Ultra Low Power electronics (ULPE) especially designed for energy harvesting systems. It is the solution consuming less energy today with 60 μJ and that is most likely to succeed with our current prototype.

Thus, our thermal energy harvesting device is expected to be able, at a given temperature variation, to power a low consumption electronic system with a stable DC voltage of around 1.5–5 V. Since our composite harvester produces higher voltage which changes its sign depending on heating or cooling, the management circuit is necessary to rectify and lower the generated voltage. In this section we will provide the essential building blocks for such a management circuit.

The core of the prototype is the P(VDF-TrFE) microgenerator, producing useful charges upon heating and/or cooling. In order to harvest these charges, several elements are needed, as schematically illustrated Figure 5.12. First, a thermal switch is necessary, which would control the transfer of charges from P(VDF-TrFE) to management circuit in a suitable way. Second, the power management circuit needs to rectify and lower the generated high voltages.

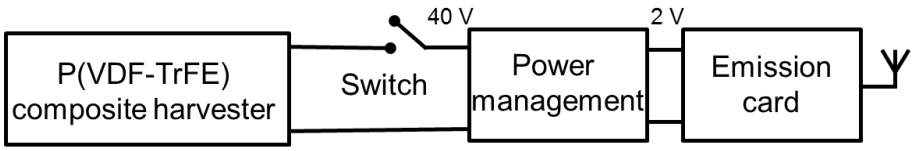

Figure 5.12. Complete conversion power management circuit. The input P(VDF-TrFE) composite is on the left side, and the output is on the right, supplying RF transmitter with antenna.

Power management

The role of the power management circuit is to convert the voltage, generated by the P(VDF-TrFE) (~40 V in our case), into a practical voltage of 1–5 V. When the ratio of input to output voltage is high (>100), one-step conversion would result in high losses [122]. Since in our case this ratio is relatively low, one-step conversion would be sufficient. As shown in [128] the simplest solution is to lower the voltage using a sufficiently big capacitor connected directly in parallel. Otherwise, commercial step-down buck converters can be used, which is preferential since they can provide regulated stable output.

The conception of the conversion circuit will depend on the usage case and the microgenerator composite configuration. If multiple-detect applications are targeted (with two-way transformation SMA), the diode bridge is required to rectify the voltage (Figure 5.13). On the other hand, if detect-once applications are of interest (with one-way transformation SMA) the circuit can be simplified since the diode bridge will no longer be necessary.

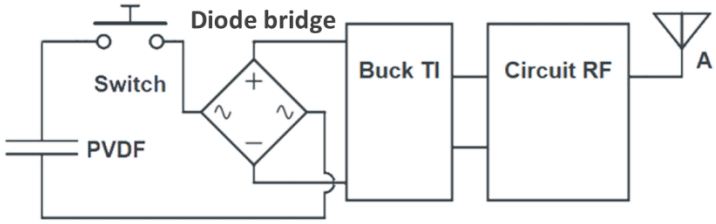

Figure 5.13. Complete conversion switch power management circuit with diode bridge (optional) and buck converter [129].

The efficiency of power conversion will depend on individual efficiencies of diodes and the buck converter. As shown in [128], most of electric losses will appear on diodes and they will increase with increased input voltage (i.e. composite generated voltage). It is therefore of interest to keep the generated voltage as low as possible, while keeping the energy as high as possible.

Concerning commercial buck converters, their efficiency can be more than 90%. In our previous work [34] we have used a buck converter from Texas Instruments (TPS62122) which can have up to 96% efficiency. The advantage of this converter is that it can convert

input voltages between 2–15 V to stable voltages of 1.5–5 V, regulated by two resistances R1 and R2 (Figure 5.14). However, in our case, the input voltage will be ~40 V, so another model of buck will be necessary. For example, TPS54062 which supports up to 60 V can be used; the price to pay is the decreased efficiency to < 90%.

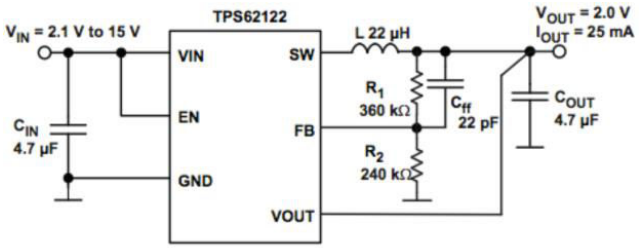

Figure 5.14. Electric diagram of the TPS62122 buck converter.

Emission card

After the voltage conversion step is succeeded, the emission card can be powered for wireless data transmission. During our previous work [122] low-consumption emission/reception cards were developed in collaboration with CEA-Grenoble Showroom (Figure 5.15).

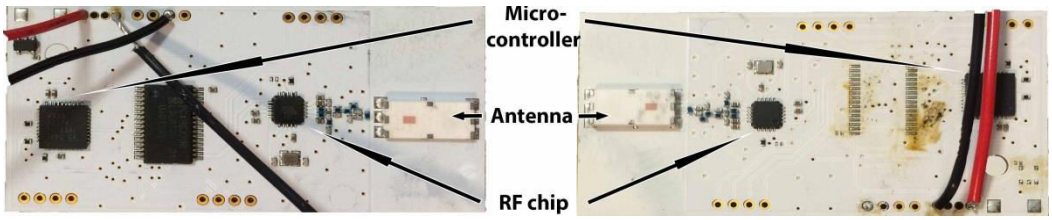

Figure 5.15. Emission (left) and reception (right) wireless cards (CEA Showroom).

To power the emission card, pulses of at least 60 µJ are necessary. It was composed of a Texas Instrument RF chip (CC110L) with a Texas Instruments micro-controller. The important point is the embedded code on the micro-controller that handles the energy consumption. When the micro-controller is supplied with energy and wakes up, the code limits the energy consumption to program the RF chip, which then sends two signals of one byte each. Then the system goes back to sleep until the next energy input. The RF chip is programmed to emit at a frequency of 868 MHz, with a rate of 250 kBits/s. This emission card can transmit signals to up to 40 meters, which is reasonably far for most wireless IoT applications.

If we now consider our composite harvester that currently produces 95 µJ and a buck TI converter with 90% efficiency, we can expect to have 85 µJ energy to supply the emission card. This energy is sufficient for such kind of low consumption emission cards. This allows us to conclude that our smart composite is promising for IoT applications. It can open a new market for smart packaging with highly flexible autonomous wireless temperature sensors, for food survey, health products control etc. (Figure 5.16). It can also meet the needs for self-powered secure cards which will become an ultra-mass market soon.

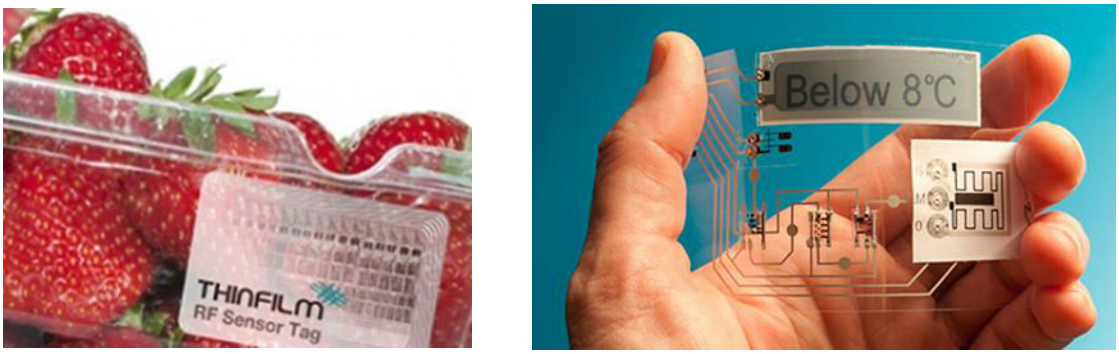

Figure 5.16. Examples of possible self-powered applications from Thinfilm [130].

5.3 Further energy increase: nanostructuration

So far in this work we have talked only about P(VDF-TrFE)-based piezoelectric generators exploiting g_{31} coefficient for simplicity of manufacture with the plate capacitor structure. Back to the analogy with MFC (Chapter 1, section 1.2.3), it would be advantageous to seek to exploit g_{33} coefficient which is twice larger than g_{31}. For this purpose, IDE generators were designed and fabricated (Chapter 2, section 2.2.3). Beyond this simple analogy with MFC, the idea of fiber composite structure pushed at the nanoscale meets that of increased piezoelectric properties with confined P(VDF-TrFE)-based nanostructures [45]-[48]. Thus, we may expect overall increase of piezoelectric voltage and energy proportional to the β-phase increase at nanoscale.

To target other applications, this further increase of harvester efficiency and produced energy is appealing. First tests were performed during this work, and we will now present preliminary results of nanoimprint lithography of the screen printed P(VDF-TrFE). We start with the development of the technique on commercial grade P(VDF-TrFE) from Piezotech.

Commercial grade P(VDF-TrFE)

First nanoimprint experiments were realized on 110 µm thick commercial grade P(VDF-TrFE) material with 75:25 VDF:TrFE ratio. The imprinted patterns consisted of cylindrical pillars with 400 nm diameter, 600 nm height and 1 µm center-to-center distance. Obducat Nano Imprint Lithography EITRE machine was used Figure 5.17.

Figure 5.17. Obducat Nano Imprint Lithography EITRE machine

Imprint parameters for PVDF materials were previously optimized in LTM-CEA laboratory (temperature = 190 ºC, pressure = 10 bar, time = 3 min). To adapt, we first perform differential scanning calorimetry (DSC) analysis on P(VDF-TrFE) samples. The melting temperature T_m of P(VDF-TrFE) was found to be 150 ºC. Therefore the imprint temperature was reduced to 160 ºC - slightly higher than T_m - and the imprint pressure was increased to 20 bars. After nanoimprint, the surface of the samples was studied by atomic force microscopy (AFM) and scanning electronic microscopy (SEM). The results are shown in Figure 5.18.

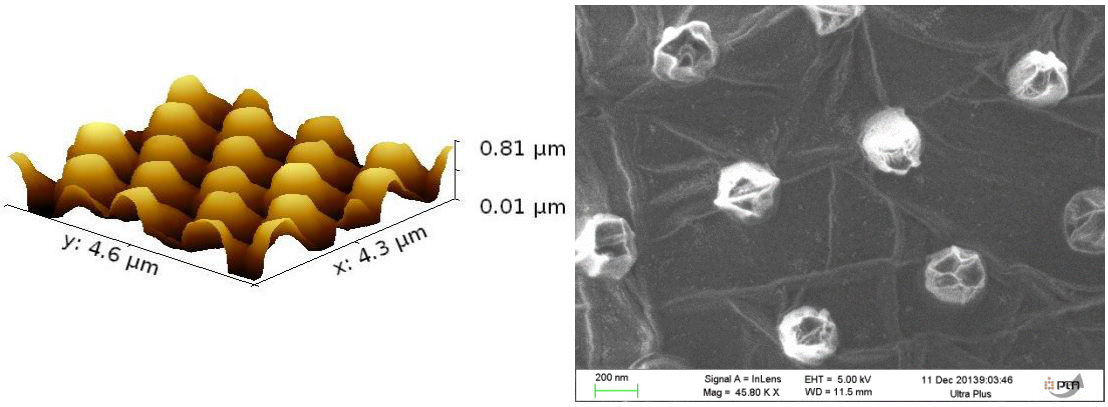

Figure 5.18. AFM (left) and SEM (right) images of nanoimprinted commercial grade P(VDF-TrFE) 75:25.

These primary tests confirmed the imprint parameters for P(VDF-TrFE): the nanopillar structure appears well-defined at the polymer surface, each pillar was uniform and well separated. Height of nanopillars was measured at ~ 600 nm, which confirms that the pattern completely transferred from the mold to the sample. However, electrical characterization cannot estimate the impact of the nanostructures, as its thickness is negligibly small compared to the whole thickness of the material (600 nm vs. 110 µm). So, further nanoimprint tests were performed on the screen printed films of P(VDF-TrFE) of this work.

Screen printed films of P(VDF-TrFE)

Here the aim was to imprint fibers instead of pillars to mimic the MFC structure. Therefore the starting material was screen-printed films of P(VDF-TrFE)-2.6 µm deposited on top of IDE Au-30 nm bottom electrodes (Design-3). For the simplicity of the experiment, dimensions were limited to sub-micron structures. For this purpose, we fabricated a new silicon mold, 2 µm-deep and with patterns consisting of lines and spaces of 1 µm and 0.5 µm. The same nanoimprint conditions were used to realize this structure. Figure 5.19 shows SEM image of a nanoimprinted sample. The lines appear regular and uniform over the imprinted surface (1 cm^2). Each individual line is well visible, without major defects and relatively uniform in width. However, it is hard to have clear indications of the total separation of lines and we may suspect partial imprint with a residual bottom layer.

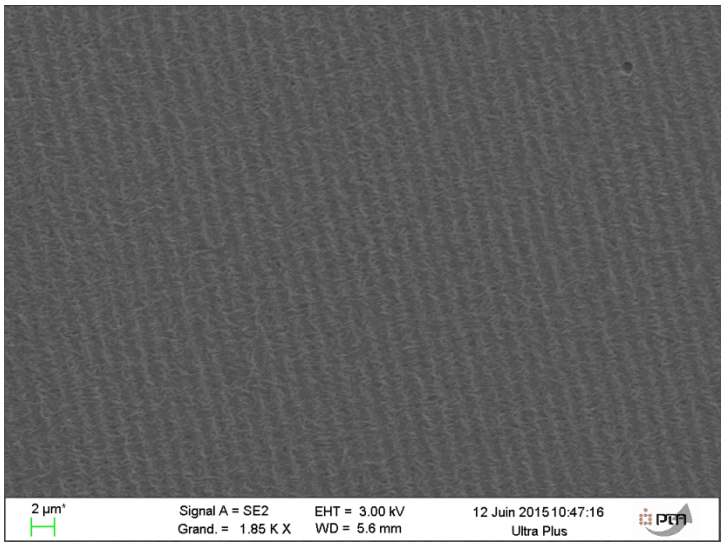

Figure 5.19. Nanoimprinted lines on 2.6 µm screen printed P(VDF-TrFE) film (line and space are 500 nm and 1 µm respectively).

Since the thickness of the imprinted layer is now comparable to the thickness of whole P(VDF-TrFE), we performed electric measurements. We first poled the IDE samples (400 V with aixACCT analyzer) and measured capacitance and polarization loops. The measured capacitance was 0.3 nF, in good agreement with theoretical value (calculated in section 2.2.3). Figure 5.20 shows hysteresis loops at 0.1 Hz before and after nanoimprint. We can observe significant increases of remanent polarization P_r (200%) and coercive field E_c (150%) after nanoimprint which indicates the promotion of higher FE order with nanostructures. However, it is worth mentioning that in both cases P_r is one order of magnitude smaller than that with the MIM capacitor structure. This is probably because the electric field which depends on IDE spacing was not sufficient to polarize the samples completely.

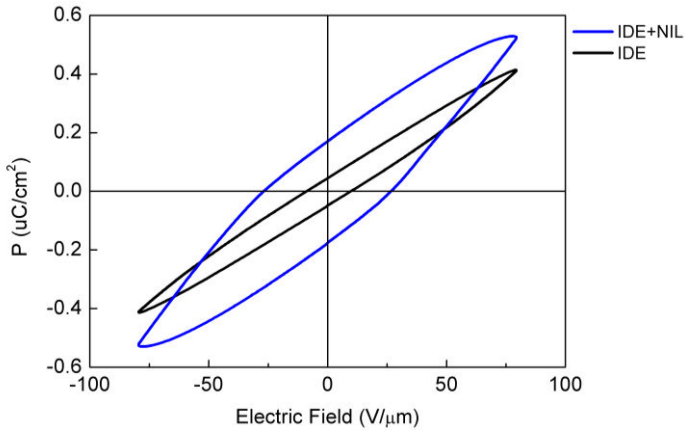

Figure 5.20. Polarization loops at 0.1 Hz of the IDE 2.6 µm screen printed P(VDF-TrFE) generators before and after nanoimprint.

After polarization and hysteresis loop measurements we have observed crack formation on the samples (Figure 5.21). These cracks appeared exactly along the electrodes and propagated to the whole sample length. The character of these cracks suggests that they appear due to application of high voltage. Moreover, piezoelectric measurements have shown no generated voltage. We may suspect inter electrodes electrical breakdown when polarizing the samples and/or mechanical issues at the step coverage with electrodes. Additional tests are required.

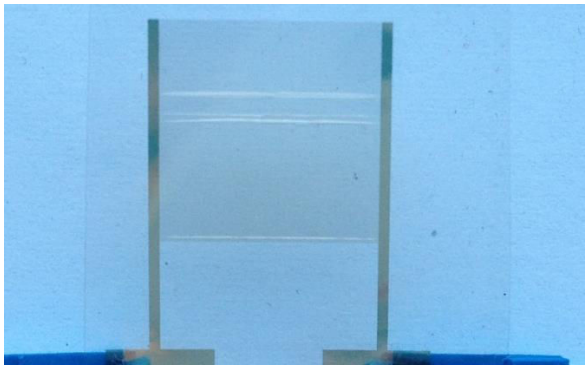

Figure 5.21. Cracks along IDE sample after polarization.

5.4 Conclusions

We realized and validated a new concept of flexible thermal energy harvesting composite based on screen printed P(VDF-TrFE) thin film and SMA foil. Voltage and energy harvesting capabilities were measured as a function of strain. The composite successfully experienced crossed-voltage from both pyro and piezoelectric effects and reached output voltages up to 37 V at 0.56 % strain and 65 ºC. The corresponding electrical energy was 95 µJ and the energy density was 19 mJ/cm^3. These numbers were put in perspective regarding very recent IoT power consumption requirements. We concluded that our thermal composite harvesters are already suitable for IoT applications.

Finally, a combination of nanostructuration and IDE electrodes was explored by nanoimprinting the screen printed P(VDF-TrFE) to mimic MFC (called NFC). The technological work was successful and preliminary electric tests showed an increase in remanent polarization with nanoimprinted structures. However, the piezoelectric response could not be evaluated yet.

General conclusions

The main achievement of this thesis is the design, fabrication and evaluation of a composite thermal energy harvester based on flexible screen printed P(VDF-TrFE) microgenerators coupled with NiTi shape memory alloy. The credit-card size device harvests thermal energy from quasi-static temporal temperature variations, and produces 95 µJ of useful output energy upon heating from room temperature to 65 ºC. This corresponds to an energy density of 19 mJ/cm^3, compatible with RFID tag applications or wireless transmission cards.

The fabrication of microgenerators was achieved with a reproducible screen printing process with new ink-based P(VDF-TrFE) materials. A functional process flow was established for the fabrication of multilayer flexible piezoelectric microgenerators, without dead layers, interfacial defects or inhomogeneity of the film microstructure. The design includes single capacitor test structures for material investigation, and parallel-connected capacitor network structures fitting on a credit card format for the prototyping.

Direct piezoelectric voltage g_{31} coefficient of screen-printed P(VDF-TrFE) thin films was measured and reported for the first time, reaching 0.15 V·m/N for network structure, i.e. twice that of commercial P(VDF-TrFE) material. The microgenerators produce strain-induced voltages up to 10 V with an energy density of 480 µJ/cm^3 at 0.4% strain, limited here by experimental conditions. In addition, the pyroelectric coefficient ρ_Q of the screen printed microgenerator network was measured to be -25 µC/K·m^2, in good agreement with literature.

To perform piezoelectric characterizations, two original loss-less methods of piezoelectric voltage measurements using a non-contacting electrostatic voltmeter and a mechanical switch in open-circuit conditions were proposed. Both methods were proven to give reliable results, allowing to reach remarkably high values of voltage.

Optimal polarization conditions of screen printed P(VDF-TrFE) copolymer were found. High P_r (~7.5 µC/cm^2) and intermediate E_c (40 V/µm) values were obtained for single microgenerators and parallel-connected capacitors, indicating high ferroelectric order.

Two types of top electrodes (Ag ink and PEDOT:PSS) were compared: microgenerators with PEDOT:PSS electrode have shown better performance in terms of leakage current density. Furthermore, samples with Ag top electrodes undergo electrical breakdowns during measurements, which were not observed for PEDOT:PSS samples. We therefore conclude that PEDOT:PSS electrode material is better adapted for screen printing deposition on polymers, and it was used for energy harvesting device prototyping.

Concerning the exploratory work undertaken in this thesis, nanoimprint structures were realized on both bulk and thin film P(VDF-TrFE). Optimal conditions were found, allowing to obtain uniform 500 nm line patterns. Preliminary tests showed an increase in remanent polarization, but further tests are needed to measure its piezoelectric response.

Original RE/FE screen printed heterostructures of P(VDF-TrFE-CTFE) and P(VDF-TrFE) were realized for the first time. Surprisingly, P(VDF-TrFE-CTFE) single layer showed pinched loops and nonzero remanent polarization, typical of a relaxor material. As a result, RE/FE heterostructures presented atypical ferroelectric responses, between pinched hysteresis and leaky structures, due to unrelaxed defect dipoles. We conclude that the poling with P(VDF-TrFE-CTFE) should be improved later.

Finally, the perspectives opened by this work offer two main ways to push forward. First, we can directly use the thermal energy harvesting device developed in this thesis to build an application case, such as a wireless self-powered thermal sensor. In order to do so, the necessary building blocks, namely a thermal switch, a power management stage and a wireless emission card, have been briefly discussed, pointing at possible alternatives and optimization paths to be followed.

Also, the harvester itself can be optimized to yield higher energy densities and efficiency. Two main ideas are proposed: the easiest way is to simply increase the amount of material used, either by building a bigger harvester with the same configuration or by increasing the amount of SMA used in the present configuration. The other option is to increase the energy output of the piezoelectric material. To do so, we have begun an exploratory work combining the nanostructuration of screen printed P(VDF-TrFE), aiming to enhance the piezoelectric properties, and an interdigital electrode scheme, allowing to work in 3-3 mode, which has higher piezoelectric coefficients than 3-1 mode. The paths started by this work look promising and should be continued.

Bibliography

[1] H. Spanggaard and F. C. Krebs, “A brief history of the development of organic and polymeric photovoltaics,” Sol. Energy Mater. Sol. Cells, vol. 83, no. 2–3, pp. 125–146, 2004.

[2] R. M. Owens and G. G. Malliaras, “Organic Electronics at the Interface with Biology,” MRS Bull., vol. 35, no. 06, pp. 449–456, 2010.

[3] S. Gunes, H. Neugebauer, and N. S. Sariciftci, “Conjugated Polymer-Based Organic Solar Cells,” Chem.Rev., vol. 107, pp. 1324–1338, 2007.

[4] C. Troadec, “Printed & flexible Electronics: From a Market & Technology Perspective,” in IITC/MAM conference, 2015.

[5] J. H. Cho, J. Lee, Y. Xia, B. Kim, Y. He, M. J. Renn, T. P. Lodge, and C. D. Frisbie, “Printable ion-gel gate dielectrics for low-voltage polymer thin-film transistors on plastic.,” Nat. Mater., vol. 7, no. 11, pp. 900–906, 2008.

[6] K. J. Baeg, M. Caironi, and Y. Y. Noh, “Toward printed integrated circuits based on unipolar or ambipolar polymer semiconductors,” Adv. Mater., vol. 25, no. 31, pp. 4210–4244, 2013.

[7] B. Kang, W. H. Lee, and K. Cho, “Recent advances in organic transistor printing processes,” ACS Appl. Mater. Interfaces, vol. 5, no. 7, pp. 2302–2315, 2013.

[8] P. F. Moonen, I. Yakimets, and J. Huskens, “Fabrication of transistors on flexible substrates: From mass-printing to high-resolution alternative lithography strategies,” Adv. Mater., vol. 24, no. 41, pp. 5526–5541, 2012.

[9] B. Kam, “Device Architecture and Materials for Organic Ferroelectric Memory Arrays,” 2014.

[10] B. Geffroy, P. le Roy, and C. Prat, “Organic light-emitting diode (OLED) technology: Materials, devices and display technologies,” Polym. Int., vol. 55, no. 6, pp. 572–582, 2006.

[11] V. Subramanian, P. C. Chang, J. B. Lee, S. E. Molesa, and S. K. Volkman, “Printed organic transistors for ultra-low-cost RFID applications,” IEEE Trans. Components Packag. Technol., vol. 28, no. 4, pp. 742–747, 2005.

[12] T. Kietzke, “Recent advances in organic solar cells,” Adv. Optoelectron., vol. 2007, 2007.

[13] J. Zheng, D. Simplot-Ryl, and H. T. Mouftah, “The Internet of Things,” IEEE Commun. Mag., no. November, pp. 30–31, 2011.

[14] R. Khan, S. U. Khan, R. Zaheer, and S. Khan, “Future internet: The internet of things architecture, possible applications and key challenges,” in Proceedings - 10th International Conference on Frontiers of Information Technology, FIT 2012, 2012, pp. 257–260.

[15] R. Das and P. Harrop, “RFID Forecasts, Players and Opportunities 2016-2026,” 2015.

[Online]. Available: http://www.idtechex.com/research/reports/rfid-forecasts-players-and-opportunities-2016-2026-000451.asp.

[16] K. Finkenweller, RFID Handbook: Fundamentals and Applications in Contactless Smart Cards, Radio Frequency Identification and Near-Field, Third Edition Communication. Wiley, 2010.

[17] L. Atzori, A. Iera, and G. Morabito, "The Internet of Things: A survey," Comput. Networks, vol. 54, no. 15, pp. 2787–2805, 2010.

[18] "RFID system." [Online]. Available: http://www.barcodesinc.com.

[19] A. Juels, "RFID Security and Privacy: A Research Survey," J. Sel. Areas Commun., vol. 24, no. 2, pp. 381–394, 2006.

[20] J. Galineau, J.-F. Capsal, P.-J. Cottinet, and M. Lallart, "Scale-like compliant gold electrode: Towards high strain capacitive devices for energy harvesting," Sensors Actuators A Phys., vol. 211, pp. 1–7, 2014.

[21] X. Crispin, F. L. E. Jakobsson, A. Crispin, P. C. M. Grim, P. Andersson, A. Volodin, C. Van Haesendonck, M. Van Der Auweraer, W. R. Salaneck, and M. Berggren, "The Origin of the High Conductivity of (PEDOT - PSS) Plastic Electrodes," Chem. Mater., vol. 18, no. 4, pp. 4354–4360, 2006.

[22] Bayer AG, "Eur. Patent," 339 340, 1988.

[23] B. L. Groenendaal, F. Jonas, D. Freitag, H. Pielartzik, and J. R. Reynolds, "Poly(3,4-ethylenedioxythiophene) and Its Derivatives: Past, Present, and Future," Adv. Mater., vol. 12, no. 7, pp. 481–494, 2000.

[24] Y. H. Kim, C. Sachse, M. L. MacHala, C. May, L. Müller-Meskamp, and K. Leo, "Highly conductive PEDOT:PSS electrode with optimized solvent and thermal post-treatment for ITO-free organic solar cells," Adv. Funct. Mater., vol. 21, no. 6, pp. 1076–1081, 2011.

[25] D. Alemu, H.-Y. Wei, K.-C. Ho, and C.-W. Chu, "Highly conductive PEDOT:PSS electrode by simple film treatment with methanol for ITO-free polymer solar cells," Energy Environ. Sci., vol. 5, no. 11, p. 9662, 2012.

[26] D. a. Mengistie, M. a. Ibrahem, P. C. Wang, and C. W. Chu, "Highly conductive PEDOT:PSS treated with formic acid for ITO-free polymer solar cells," ACS Appl. Mater. Interfaces, vol. 6, no. 4, pp. 2292–2299, 2014.

[27] T. Starner, "Human-powered wearable computing," IBM Syst. J., vol. 35, no. 3.4, pp. 618–629, 1996.

[28] R. Guigon, J.-J. Chaillout, T. Jager, and G. Despesse, "Harvesting raindrop energy: experimental study," Smart Mater. Struct., vol. 17, no. 1, p. 015039, 2008.

[29] S. Takamatsu, T. Kobayashi, T. Imai, T. Yamashita, and T. Itoh, "All Polymer Piezoelectric Film for the Application to Low Resonance Frequency Energy Harvester," Procedia Eng., vol. 25, pp. 203–206, 2011.

[30] G. Canavese, S. Stassi, V. Cauda, A. Verna, P. Motto, A. Chiodoni, S. L. Marasso, and D. Demarchi, "Different scale confinements of PVDF-TrFE as functional material of piezoelectric devices," IEEE Sens. J., vol. 13, no. 6, pp. 2237–2244, 2013.

[31] J. H. Lee, K. Y. Lee, M. K. Gupta, T. Y. Kim, D. Y. Lee, J. Oh, C. Ryu, W. J. Yoo, C. Y. Kang, S. J. Yoon, J. B. Yoo, and S. W. Kim, "Highly stretchable piezoelectric-pyroelectric hybrid nanogenerator," Adv. Mater., vol. 26, no. 5, pp. 765–769, 2014.

[32] Z. Pi, J. Zhang, C. Wen, Z. Zhang, and D. Wu, “Flexible piezoelectric nanogenerator made of poly(vinylidenefluoride-co-trifluoroethylene) (PVDF-TrFE) thin film,” Nano Energy, vol. 7, pp. 33–41, Jul. 2014.

[33] M. Brissaud, *Matériaux piézoélectriques*, PPUR. 2007.

[34] B. Gusarov, L. Gimeno, E. Gusarova, B. Viala, S. Boisseau, and O. Cugat, “Flexible composite thermal energy harvester using piezoelctric PVDF polymer and shape memory alloy,” IEEE Solid-State Sensors, Actuators Microsystems, pp. 722–725, 2015.

[35] H. Kawai, “The Piezoelectricity of Poly (vinylidene Fluoride),” Jpn. J. Appl. Phys., vol. 8, pp. 975–976, 1969.

[36] S. K. Mahadeva, J. Berring, K. Walus, and B. Stoeber, “Effect of poling time and grid voltage on phase transition and piezoelectricity of poly(vinyledene fluoride) thin films using corona poling,” J. Phys. D. Appl. Phys., vol. 46, no. 28, p. 285305, 2013.

[37] J. F. Mano, a M. Costa, and V. H. Schmidt, “Ftir and Dsc Studies of Mechanically Deformed B-Pvdf Films,” J. Macromol. Sci. Phys., vol. 40, no. 3&4, pp. 517–527, 2001.

[38] P. Ueberschlag, “PVDF piezoelectric polymer,” Sens. Rev., vol. 21, no. 2, pp. 118–126, 2001.

[39] J.-K. Yuan, Z.-M. Dang, S.-H. Yao, J.-W. Zha, T. Zhou, S.-T. Li, and J. Bai, “Fabrication and dielectric properties of advanced high permittivity polyaniline/poly(vinylidene fluoride) nanohybrid films with high energy storage density,” J. Mater. Chem., vol. 20, no. 12, p. 2441, 2010.

[40] T. Yamada, T. Ueda, and T. Kitayama, “Ferroelectric-To-Paraelectric Phase Transition of Vinylidene Fluoride-Trifluoroethylene Copolymer.,” J. Appl. Phys., vol. 52, no. 2, pp. 948–952, 1981.

[41] F. Bauer, “Relaxor fluorinated polymers: Novel applications and recent developments,” IEEE Trans. Dielectr. Electr. Insul., vol. 17, no. 4, pp. 1106–1112, 2010.

[42] B. C. B. Chu, X. Z. X. Zhou, B. Neese, Q. M. Zhang, and F. Bauer, “Relaxor ferroelectric poly(vinylidene fluoride-trifluoroethylene-chlorofluoroethylene) terpolymer for high energy density storage capacitors,” IEEE Trans. Dielectr. Electr. Insul., vol. 13, no. 5, pp. 1162–1169, 2006.

[43] P. S., “Criterion for material selection in design of bulk piezoelectric energy harvesters,” IEEE Trans Ultrason Ferroelectr Freq Control, vol. 57, no. 12, 2010.

[44] M. Defosseux, “Conception et caractérisation de microgénérateurs piézoélectriques pour microsystèmes autonomes,” Thèse de doctorat d’université. Grenoble: Université de Grenoble, 2011.

[45] Z. Hu, G. Baralia, V. Bayot, J. F. Gohy, and A. M. Jonas, “Nanoscale control of polymer crystallization by nanoimprint lithography,” Nano Lett., vol. 5, no. 9, pp. 1738–1743, 2005.

[46] X. Li, Y.-F. Lim, K. Yao, F. E. H. Tay, and K. H. Seah, “P(VDF-TrFE) ferroelectric nanotube array for high energy density capacitor applications.,” Phys. Chem. Chem. Phys., vol. 15, no. 2, pp. 515–20, 2013.

[47] J. R. Fang, X. Y. Luo, Z. Ma, Z. K. Shen, Q. Lu, B. R. Lu, G. D. Zhu, X. P. Qu, R. Liu, and Y. F. Chen, “Influence of nano-embossing on properties of poly(VDF-TrFE),” Microelectron. Eng., vol. 87, no. 5–8, pp. 890–892, 2009.

[48] J. R. Fang, Z. K. Shen, S. Yang, Q. Lu, J. Li, Y. F. Chen, and R. Liu, "Nanoimprint of ordered ferro/piezoelectric P(VDF-TrFE) nanostructures," Microelectron. Eng., vol. 88, no. 8, pp. 2033–2036, 2011.

[49] Y. Liu, D. N. Weiss, and J. Li, "Rapid nanoimprinting and excellent piezoresponse of polymeric ferroelectric nanostructures," ACS Nano, vol. 4, no. 1, pp. 83–90, 2010.

[50] C. C. Hong, S. U. Huang, J. Shieh, S. H. Chen, and A. Chen, "Piezoelectricity of sub-20-nm nanoimprinted PVDF-TrFE nanograss," Proc. IEEE Int. Conf. Micro Electro Mech. Syst., no. February, pp. 1336–1339, 2012.

[51] C. Chang, V. H. Tran, J. Wang, Y. K. Fuh, and L. Lin, "Direct-write piezoelectric polymeric nanogenerator with high energy conversion efficiency," Nano Lett., vol. 10, no. 2, pp. 726–731, 2010.

[52] J. Chang, M. Dommer, C. Chang, and L. Lin, "Piezoelectric nanofibers for energy scavenging applications," Nano Energy, vol. 1, no. 3, pp. 356–371, 2012.

[53] S. Y. Chou, P. R. Krauss, W. Zhang, L. Guo, and L. Zhuang, "Sub-10 nm imprint lithography and applications," J. Vac. Sci. Technol. B, vol. 15, pp. 2897–2904, 1997.

[54] C. Gourgon, C. Perret, J. Tallal, F. Lazzarino, S. Landis, O. Joubert, and R. Pelzer, "Uniformity across 200 mm silicon wafers printed by nanoimprint lithography," J. Phys. D. Appl. Phys., vol. 38, no. 1, pp. 70–73, 2005.

[55] "Macro Fiber Composite (MFC) Smart Material Corp." [Online]. Available: http://www.smart-material.com/MFC-product-main.html.

[56] G. A. Lebedev, B. V. Gusarov, B. Viala, J. Delamare, O. Cugat, T. Lafont, and D. I. Zakharov, "Thermal energy harvesting using shape memory/piezoelectric composites," Solid-State Sensors, Actuators Microsystems Conf., pp. 669–670, 2011.

[57] D. Zakharov, G. Lebedev, O. Cugat, J. Delamare, B. Viala, T. Lafont, L. Gimeno, and A. Shelyakov, "Thermal energy conversion by coupled shape memory and piezoelectric effects," J. Micromechanics Microengineering, vol. 22, no. 9, p. 094005, 2012.

[58] T. Huesgen, P. Woias, and N. Kockmann, "Design and fabrication of MEMS thermoelectric generators with high temperature efficiency," Sensors Actuators, A Phys., vol. 145–146, no. 1–2, pp. 423–429, 2008.

[59] G. Sebald, E. Lefeuvre, and D. Guyomar, "Pyroelectric energy conversion: Optimization principles," IEEE Trans. Ultrason. Ferroelectr. Freq. Control, vol. 55, no. 3, pp. 538–551, 2008.

[60] C. M. Wayman, "Shape Memory Alloys," MRS Bull., vol. 1, pp. 49–56, 1993.

[61] D. Zakharov, "Matériaux composites à base d'alliage à mémoire de forme et pyro-/piézoélectrique pour la récupération d'énergie thermique," Thèse de doctorat d'université. Grenoble: Université Grenoble Alpes 2014.

[62] D. Mao, M. a. Quevedo-Lopez, H. Stiegler, B. E. Gnade, and H. N. Alshareef, "Optimization of poly(vinylidene fluoride-trifluoroethylene) films as non-volatile memory for flexible electronics," Org. Electron., vol. 11, no. 5, pp. 925–932, May 2010.

[63] E. Vitoratos, "Conductivity Degradation Study of PEDOT: PSS Films under Heat Treatment in Helium and Atmospheric Air," Open J. Org. Polym. Mater., vol. 02, no. 01, pp. 7–11, 2012.

[64] J. Huang, P. F. Miller, J. C. de Mello, a. J. de Mello, and D. D. C. Bradley, "Influence of thermal treatment on the conductivity and morphology of PEDOT/PSS films," Synth. Met., vol. 139, no. 3, pp. 569–572, 2003.

[65] N. Koch, a Vollmer, a Elschner, and S. Gmbh, "Influence of water on the work function of conducting poly (3,4-ethylenedioxythiophene)/(poly(styrenesulfonate)," Appl. Phys. Lett., vol. 90, no. 2007, p. 043512, 2007.

[66] V. Zardetto, T. M. Brown, A. Reale, and A. Di Carlo, "Substrates for flexible electronics: A practical investigation on the electrical, film flexibility, optical, temperature, and solvent resistance properties," J. Polym. Sci. Part B Polym. Phys., vol. 49, no. 9, pp. 638–648, 2011.

[67] B. a. MacDonald, K. Rollins, D. MacKerron, K. Rakos, R. Eveson, K. Hashimoto, and B. Rustin, "Engineered Films for Display Technologies," Flex. Flat Panel Displays, pp. 11–33, 2005.

[68] "Teijin DuPont Films PET/PEN." [Online]. Available: https://www.teijindupontfilms.jp/english/product/hi_film.html.

[69] "Silver Screen Ink – Metalon® HPS-021LV." [Online]. Available: https://store.novacentrix.com/v/vspfiles/assets/images/metalon hps-021lv_2230.1.pdf.

[70] "PEDOT:PSS CLEVIOS™ S V4." [Online]. Available: http://www.heraeus-clevios.com/media/webmedia_local/media/datenblaetter/81076374_Clevios_S_V4_20101222.pdf.

[71] "DISPLAY CARD." [Online]. Available: http://www.nidsecurity.com/products/.

[72] "Macro fiber composite - MFC." [Online]. Available: http://www.smart-material.com/MFC-product-main.html.

[73] N. Galopin, "Finite Element Modeling of Magnetoelectric Composites with Interdigitated Electrodes," COMPUMAG, 2015.

[74] B. Viala, "Le ferromagnétisme en couches minces pour les hyperfréquences," Habilitation à diriger des recherches. Grenoble: Université de Grenoble, 2008.

[75] Y. T. G. SHIRANE, E. SAWAGUCHI, "Dielectric Properties of Lead Zirconate," Phys. Rev., vol. 84, no. 3, 1951.

[76] M. I. Morozov, D. Damjanovic, M. I. Morozov, and D. Damjanovic, "Hardening-softening transition in Fe-doped Pb(Zr,Ti)O3 ceramics and evolution of the third harmonic of the polarization response," vol. 034107, no. 2008, 2012.

[77] X. Y. Xihong Hao, Jiwei Zhai, "Improved Energy Storage Performance and Fatigue Endurance of Sr-Doped PbZrO 3 Antiferroelectric Thin Films," J. Am. Ceram. Soc., vol. 92, no. 5, pp. 1133–1135, 2009.

[78] J. Gé, "Films anti ferroélectrique à base de PbZrO3 pour le stockage de l'énergie," l'Université de Valenciennes et du Hainaut-Cambresis, 2015.

[79] A. Sarkar and S. B. Krupanidhi, "Ferroelectric interaction and polarization studies in BaTiO[sub 3]/SrTiO[sub 3] superlattice," J. Appl. Phys., vol. 101, no. 10, pp. 104113–104116, 2007.

[80] D. Bao, "Multilayered dielectric/ferroelectric thin films and superlattices," Curr. Opin. Solid State Mater. Sci., vol. 12, no. 3–4, pp. 55–61, 2008.

[81] Y.-Z. Wu, D.-L. Yao, and Z.-Y. Li, "Hysteresis loops of a ferroelectric superlattice with an antiferroelectric interfacial coupling," J. Appl. Phys., vol. 91, no. 3, pp. 1482–

1486, 2002.

[82] L. Pintilie, K. Boldyreva, M. Alexe, and D. Hesse, “Capacitance tuning in antiferroelectric–ferroelectric PbZrO3–Pb(Zr0.8Ti0.2)O3 epitaxial multilayers,” New J. Phys., vol. 10, no. 1, p. 013003 (12pp), 2008.

[83] T. R. S. Seung-Eek Park, “Ultrahigh strain and piezoelectric behavior in relaxor based ferroelectric single crystals,” vol. 82, no. 1804, 1997.

[84] R. Guo, L. E. Cross, S. Park, B. Noheda, D. E. Cox, and G. Shirane, “Origin of the High Piezoelectric Response in PbZr 1- x Ti x O 3,” Phys. Rev. Lett., vol. 84, no. 23, 2000.

[85] X. L. Zhao, J. L. Wang, B. L. Liu, B. B. Tian, Y. H. Zou, S. Sun, J. L. Sun, X. J. Meng, and J. H. Chu, “Enhanced dielectric and ferroelectric properties in the artificial polymer multilayers,” Appl. Phys. Lett., vol. 104, no. 8, pp. 2013–2016, 2014.

[86] J. Kim, H. You, S. Ducharme, and S. Adenwalla, “The effect of interlayer interactions on the ferroelectric–paraelectric phase transition in multilayered thin films of vinylidene fluoride–trifluoroethylene copolymers,” J. Phys. Condens. Matter, vol. 19, no. 8, p. 086206, 2007.

[87] S. Patel, A. Chauhan, and R. Vaish, “A technique for giant mechanical energy harvesting using ferroelectric/antiferroelectric materials,” J. Appl. Phys., vol. 115, no. 8, pp. 1–7, 2014.

[88] J. B. Neaton and K. M. Rabe, “Theory of polarization enhancement in epitaxial BaTiO3/SrTiO3 superlattices,” Appl. Phys. Lett., vol. 82, no. 10, pp. 1586–1588, 2003.

[89] C. Bungaro and K. M. Rabe, “Epitaxially strained [001]-(PbTiO3)1(PbZrO3)1 superlattice and PbTiO3 from first principles,” Phys. Rev. B, vol. 69, no. 18, p. 184101, 2004.

[90] V. a. Stephanovich, I. a. Luk’yanchuk, and M. G. Karkut, “Domain-Enhanced Interlayer Coupling in Ferroelectric/Paraelectric Superlattices,” Phys. Rev. Lett., vol. 94, no. 4, p. 047601, 2005.

[91] R. Ranjith, R. Nikhil, and S. B. Krupanidhi, “Interfacial coupling and its size dependence in PbTiO3 and PbMg1/3Nb2/3O3 multilayers,” Phys. Rev. B, vol. 74, no. 18, p. 184104, 2006.

[92] H. S. Nalwa, Ferroelectric Polymers: Chemistry, Physics, and Applications. New York: Marcel Dekker, Inc, 1995.

[93] O. Pabst, J. Perelaer, E. Beckert, U. S. Schubert, R. Eberhardt, and A. Tünnermann, “All inkjet-printed piezoelectric polymer actuators: Characterization and applications for micropumps in lab-on-a-chip systems,” Org. Electron., vol. 14, no. 12, pp. 3423–3429, Dec. 2013.

[94] R. S. Dahiya, M. Valle, G. Metta, L. Lorenzelli, and S. Pedrotti, “Deposition, processing and characterization of P(VDF-TrFE) thin films for sensing applications,” IEEE Sensors 2008 Conf., pp. 490–493, Oct. 2008.

[95] K. Asadi, D. M. de Leeuw, B. de Boer, and P. W. M. Blom, “Organic non-volatile memories from ferroelectric phase-separated blends.,” Nat. Mater., vol. 7, no. 7, pp. 547–50, Jul. 2008.

[96] Z. Hu, M. Tian, B. Nysten, and A. M. Jonas, “Regular arrays of highly ordered ferroelectric polymer nanostructures for non-volatile low-voltage memories.,” Nat. Mater., vol. 8, no. 1, pp. 62–7, Jan. 2009.

[97] S. Fedosov and A. Sergeeva, “Corona poling of ferroelectric and nonlinear optical polymers,” Mold. J. Phys. Sci., pp. 28–31, 2002.

[98] M. H. Mahmood and H. L. Saadon, “Study of the electro-optic effect in new organic nonlinear optical polymeric materials,” J. Phys. D. Appl. Phys., vol. 45, no. 23, p. 235302, Jun. 2012.

[99] S. Bauer, “Poled polymers for sensors and photonic applications,” J. Appl. Phys., vol. 80, no. 10, p. 5531, 1996.

[100] P. T. Dao, D. J. Williams, W. P. McKenna, and K. Goppert-Berarducci, “Constant current corona charging as a technique for poling organic nonlinear optical thin films and the effect of ambient gas,” J. Appl. Phys., vol. 73, no. 5, p. 2043, 1993.

[101] B. Gross, R. Gerhard-Multhaupt, a. Berraissoul, and G. M. Sessler, “Electron-beam poling of piezoelectric polymer electrets,” J. Appl. Phys., vol. 62, no. 4, p. 1429, 1987.

[102] D. Schilling, K. Dransfeld, E. Bihler, K. Holdik, and W. Eisenmenger, “Polarization profiles of polyvinylidene fluoride films polarized by a focused electron beam,” J. Appl. Phys., vol. 65, no. 1, p. 269, 1989.

[103] S. Fujisaki, H. Ishiwara, and Y. Fujisaki, “Low-voltage operation of ferroelectric poly(vinylidene fluoride-trifluoroethylene) copolymer capacitors and metal-ferroelectric- insulator-semiconductor diodes,” Appl. Phys. Lett., vol. 90, no. 16, p. 162902, 2007.

[104] J. C. Hicks and T. E. Jones, “Frequency dependence of remanent polarization and the correlation of piezoelectric coefficients with remanent polarization in polyvinylidene fluoride,” Ferroelectrics, vol. 32, no. 1, pp. 119–126, 1981.

[105] E. F. Takeo Furukawa, “Piezoelectric Relaxation in Composite Epoxy-PZT System due to Tonic Conduction,” Jpn. J. Appl. Phys., vol. 16, no. 453, 1977.

[106] D. Fu, K. Suzuki, and K. Kato, “Frequency Dependence of Polarization Hysteresis Loop in $CaBi_4Ti_4O_{14}$ Ferroelectric Thin Films,” Integr. Ferroelectr., vol. 61, no. 1, pp. 19–23, 2004.

[107] H. Xu, Z.-Y. Cheng, D. Olson, T. Mai, Q. M. Zhang, and G. Kavarnos, “Ferroelectric and electromechanical properties of poly(vinylidene-fluoride–trifluoroethylene–chlorotrifluoroethylene) terpolymer,” Appl. Phys. Lett., vol. 78, no. 16, p. 2360, 2001.

[108] F. Bauer, E. Fousson, Q. M. Zhang, and L. M. Lee, “Ferroelectric copolymers and terpolymers for electrostrictors: Synthesis and properties,” IEEE Trans. Dielectr. Electr. Insul., vol. 11, no. 2, pp. 293–298, 2004.

[109] D. Damjanovic, Hysteresis in Piezoelectric and Ferroelectric Materials, vol. 3. Elsevier, 2005.

[110] J. F. Scott, “Ferroelectrics go bananas,” J. Phys. Condens. Matter, vol. 20, no. 2, p. 021001, 2008.

[111] Piezotech, “Piezoelectric films technical information.” [Online]. Available: http://www.piezotech.fr/image/documents/22-31-32-33-piezotech-piezoelectric-films-leaflet.pdf.

[112] A. C. Pronk, Theory of the four point dynamic bending test. 2006.

[113] S. P. Beeby, M. J. Tudor, and N. M. White, “Energy harvesting vibration sources for microsystems applications,” Meas. Sci. Technol., vol. 17, no. 12, pp. R175–R195, 2006.

[114] T. Lafont, L. Gimeno, J. Delamare, G. a Lebedev, D. I. Zakharov, B. Viala, O. Cugat, N. Galopin, L. Garbuio, and O. Geoffroy, “Magnetostrictive–piezoelectric composite structures for energy harvesting,” J. Micromechanics Microengineering, vol. 22, no. 9, p. 094009, 2012.

[115] L. W. Martin, S. P. Crane, Y.-H. Chu, M. B. Holcomb, M. Gajek, M. Huijben, C.-H. Yang, N. Balke, and R. Ramesh, “Multiferroics and magnetoelectrics: thin films and nanostructures,” J. Phys. Condens. Matter, vol. 20, no. 43, p. 434220, 2008.

[116] “Definition of a Shape Memory Alloy,” SmartLab TexasA&M. [Online]. Available: http://smart.tamu.edu/overview/smaintro/simple/definition.html.

[117] “Nitinol Specification Guidelines,” Johnson Matthey Medical Components. [Online]. Available: http://jmmedical.com/resources/120/Nitinol-Specification-Guidelines.html.

[118] “NIMESIS.” [Online]. Available: http://www.nimesis.com/.

[119] “MEMRY.” [Online]. Available: http://memry.com.

[120] “3M Scotch-Weld TM Epoxy Adhesives DP460,” Technical Data. [Online]. Available: http://multimedia.3m.com/mws/media/66122O/3mtm-scotch-weld-tm-epoxy-adhesive-dp460-ns-and-off-white.pdf.

[121] W. Huang, “On the selection of shape memory alloys for actuators,” Mater. Des., vol. 23, no. 1, pp. 11–19, 2002.

[122] Boris Gusarov, "PVDF piezoelectric polymers : characterization and application to thermal energy harvesting." Thèse de doctorat d’université. Grenoble: Université Grenoble Alpes, 2015.

[123] A. Cuadras, M. Gasulla, and V. Ferrari, “Thermal energy harvesting through pyroelectricity,” Sensors Actuators A Phys., vol. 158, no. 1, pp. 132–139, 2010.

[124] G. Reiter, “Wireless connectivity for the Internet of Things,” Texas Instrum. White Pap., pp. 1–13, 2014.

[125] “ZigBee Alliance.” .

[126] “EnerBee Start-Up.” [Online]. Available: http://www.enerbee.fr/fr/accueil/.

[127] B. Viala, “Convertisseur d’energie à récuperer et générateur d'electricité,” E.N. 13 60433, 2013.

[128] T. Lafont, “Récupération d’énergie par couplage piézoélectrique et magnétostrictif et électronique de gestion adaptée,” Thèse de doctorat d’université. Grenoble: Université Grenoble Alpes, 2014.

[129] B. Viala, G. Lebedev, J. Delamare, O. Cugat, D. Zakharov, and L. Gimeno Monge, “Energy recovery system,” WO 2014/063952 Al, 2014.

[130] “Thinfilm.” [Online]. Available: http://www.thinfilm.no/.

Résumé étendu en français

Dans les années à venir, les défis liés au changement climatique et l'environnement auront un rôle majeur dans notre vie quotidienne. Les objectifs de réduction de la consommation d'énergie et l'empreinte écologique exigent une multiplicité de solutions à différents niveaux: depuis les particuliers jusqu'aux infrastructures et systèmes industriels. Dans le cas des produits de consommation, actuellement nous avons une unique source d'alimentation des appareils: électrochimique, avec des piles jetables. Les applications commerciales de demain doivent cibler les sources d'énergie alternatives disponibles dans la nature qui ont été négligées jusqu'ici. Ces sources peuvent être thermiques, mécaniques et électromagnétique. Ces solutions «vertes» (sans batterie ou ne nécessitant pas d'être branchées au réseau électrique) s'appuient sur un ou plusieurs des trois grands principes physiques suivants: l'effet Peltier-Seebeck (aussi appelé effet thermoélectrique) qui implique la génération d'un courant électrique en présence de la chaleur; l'effet piézoélectrique direct qui consiste à générer une tension électrique sous l'action d'une contrainte mécanique; et enfin l'effet inductif qui génère un courant électrique à travers un conducteur en présence d'un champ magnétique variable.

L'originalité de notre travail est de réaliser des systèmes de récupération d'énergie flexibles de grande surface (~cm^2) en exploitant les matériaux piézoélectriques organiques à base de fluorure de polyvinylidène (PVDF). Ce matériau est très flexible et durable, ce qui le rend attrayant pour les applications dans des systèmes avec des géométries complexes, par exemple dans les cas où l'énergie devrait être récoltée sur des câbles ou tuyaux tordus, utilisés en contact avec la peau ou intégrés dans des emballages de produits de consommation. En outre, le PVDF et ses copolymères sont disponibles dans des grandes feuilles, ce qui ouvre des perspectives pour l'utilisation dans l'électronique souple de grande surface. Ces propriétés permettront aux systèmes utilisant du PVDF de bénéficier d'énergies et de puissances de sorties élevées, potentiellement supérieures aux solutions conventionnelles utilisant des matériaux piézoélectriques rigides tels que les céramiques.

Un autre avantage du PVDF et ses copolymères est qu'ils sont disponibles sous forme d'encres pour l'électronique imprimable, ce qui peut simplifier et réduire le coût du processus de fabrication. Par conséquent, l'objectif de ce travail est de réaliser des récupérateurs d'énergie souples en films minces de grande surface au moyen de méthodes de sérigraphie.

Électronique flexible

Au cours de dernières années l'électronique flexible (ou imprimée) a reçu une grande attention. Les circuits flexibles possèdent un certain nombre d'avantages par rapport à l'électronique classique à base de silicium, parmi lesquels une grande flexibilité et un poids léger, les rendant utiles pour de nombreuses applications, telles que l'électronique portable. En outre, ils peuvent être transparents, qui peut être utilisé dans le photovoltaïque [1] et les emballages intelligents, pour la nourriture par exemple. Un autre domaine d'application très important implique les interfaces avec la biologie. Les matériaux organiques proposent une meilleure compatibilité mécanique avec les tissus, et leur flexibilité convient aux facteurs de forme non-planaires souvent nécessaires pour les implants [2]. D'autres avantages de l'électronique flexible sont le faible coût de la synthèse des matériaux ainsi que la facilité de fabrication facile de dispositifs à couches minces par des technologies d'impression ou évaporation sous vide / sublimation [3]. En outre, avec des nouveaux matériaux fonctionnels sous forme d'encre, tels que des polymères électroactifs, on peut étendre l'électronique flexible à la conception de systèmes et matériaux « intelligents ».

Ainsi, utilisation de l'électronique imprimée donne la possibilité d'atteindre de nouvelles fonctionnalités et de créer de nouvelles applications. Pour l'instant, nous pouvons distinguer quatre grandes familles d'applications [4]:

•Affichage

•Éclairage

•Capteurs

•Alimentation

L'électronique imprimée: techniques habituelles

Une stratégie importante pour la conception et la fabrication de circuits électroniques flexibles est d'utiliser des matériaux en solution qui peuvent être directement imprimés et intégrés en tant que composants électroniques à haute performance sur des substrats plastiques. Dans ce contexte, les principales motivations pour l'utilisation de l'électronique imprimée sont l'économie potentielle avec les méthodes d'impression à haut débit et la

compatibilité de l'impression avec les processus roll-to-roll sur grande surface plastique ou papier [5].

Puisque les polymères sont généralement solubles dans des solvants organiques, ils sont souvent utilisés pour le dépôt à partir de solution [6]. Une variété d'encres fonctionnelles basées sur des matériaux polymères conducteurs, semi-conducteurs et isolants ont été développés. En raison de leur faible température de traitement, il devient possible de réduire les coûts de production en remplaçant les substrats de silicium avec des matériaux flexibles à faible coût tels que le plastique, le verre mince, et même le papier. Aussi, des procédés d'impression fournissent un moyen d'avoir des plates-formes de recherche et de production efficaces, ce qui les rend intéressantes pour l'industrie [7], comme par exemple Pictic au CEA Liten, qui utilise des équipements de fabrication à grande vitesse. Pour déposer des couches minces organiques, différentes techniques d'impression existent, chacune avec leurs avantages et leurs inconvénients. Nous allons maintenant expliquer brièvement quelques-unes des techniques les plus prometteuses.

La sérigraphie

La sérigraphie est une des techniques d'impression les plus utilisées. Pendant le dépôt, un écran avec le motif souhaité est placé au-dessus de la surface du substrat. L'encre polymère est chargée sur l'écran, qui est ensuite balayé par un squeegee caoutchouc avec une certaine vitesse. Au point de contact, la solution passe à travers les ouvertures de l'écran jusqu'à la surface du substrat. Le matériau est ainsi transféré sur le substrat, en formant le motif souhaité. L'écran se compose généralement d'un treillis poreux, réalisé à partir de matériaux tels qu'un tissu, de l'aluminium ou de l'acier inoxydable [8]. Ce processus est très simple et pas cher par rapport à d'autres méthodes. L'épaisseur de la couche déposée change en fonction de la viscosité de la solution et de la vitesse. Cette technique permet la préparation de couches relativement épaisses (de un à plusieurs microns). La résolution est limitée à 20-100 µm, semblable à l'impression jet d'encre, et la vitesse d'impression est généralement de 2 à 3 m^2/ s [6]. Les principaux inconvénients de cette technique sont les difficultés de production de couches minces homogènes, le gaspillage d'une grande quantité de matériel qui reste sur l'écran après le dépôt, et une consommation élevée de solvants pour le nettoyage de l'écran.

Impression par gravure

L'impression par gravure est une technique d'impression par transfert dans laquelle le dépôt d'encre est effectué à partir d'un réservoir d'encre sur une surface d'impression en utilisant un cylindre d'héliogravure gravé. Ce cylindre est recouvert de cellules périodiques qui sont remplies d'encre, et l'excès est raclé de sa surface en utilisant une lame. Le substrat est placé entre le cylindre d'impression en caoutchouc et le cylindre de gravure avec l'encre. Quand les deux cylindres sont mis en rotation, l'encre contenue dans les motifs est transférée sur le substrat. L'utilisation de l'héliogravure est attrayante en raison de son haut débit, un bon contrôle de la taille de motifs d'impression, et la flexibilité en termes de sélection de substrat. La température du cylindre, de l'encre et du substrat est contrôlée afin d'optimiser les caractéristiques imprimées. La largeur et l'épaisseur du motif dépendent de la largeur et la profondeur de la gravure dans le moule, de la vitesse d'impression, de la viscosité de l'encre, et des énergies de surface entre l'encre et substrat [7]. Ceci est une technique d'impression de masse qui est beaucoup plus productive que d'autres techniques d'impression, avec un débit élevé de 10-60 m^2/s [6].

Impression jet d'encre

L'impression à jet d'encre est un procédé d'impression numérique sans contact. Dans cette technique, semblable à celle d'une imprimante de bureau, une buse est utilisée pour déposer de petits volumes (gouttelettes) de solution sur les différentes zones du substrat [9].

L'absence de masque ou écran, qui sont utilisés pour d'autres techniques, permet le changement rapide et facile de la conception souhaitée et évite le gaspillage d'encre. L'impression par jet d'encre est un montage relativement compact, ce qui en fait une technique couramment utilisée à l'échelle du laboratoire. La résolution réalisable avec l'impression par jet d'encre classique est de 20-50 μm [6]. Le contrôle de la forme, l'épaisseur et la morphologie de la gouttelette se fait en fonction du type de solvant, de la concentration de l'encre et du réglage de la viscosité. L'impression par jet d'encre a quelques inconvénients par rapport aux technologies d'impression de masse, principalement l'utilisation de la buse, qui limite le rendement en termes de débit (0,01-0,5 m^2/s) [6]. En outre, l'uniformité du film et son homogénéité sont également limitées en raison du dépôt de couches goutte à goutte. Ainsi, cette technique reste plus appropriée pour la fabrication à petite échelle en laboratoire.

Conclusions

Ici, nous avons présenté les méthodes d'impression les plus utilisées pour la production de composants électroniques sur des substrats en plastique. Leurs principales caractéristiques en termes de viscosité de la solution, de l'épaisseur de couche déposée et la gamme de débit disponible sont résumés dans le Tableau 1.1.

Tableau 1.1. Caractéristiques des différentes techniques d'impression. Résumé de [6].

Techniques d'impression	Type d'impression	Viscosité [Pas]	Épaisseur [µm]	Vitesse [m^2/s]	Caractéristiques
Jet d'encre	Écriture directe	0.001–0.04	0.01-20	0.01–0.5	Sans contact, petites quantités d'encre, impression numérique, encre à faible viscosité, vitesse lente
Sérigraphie	Écriture directe	0.5–50	0.015-100	2–3	Robuste, simple, couche épaisse possible, grande échelle possible, haute viscosité de l'encre, gaspillage de matériau
Gravure	Transfert	0.01–0.2	< 0.1–8	3–60	Impression rapide, haute résolution, coût relativement élevé de la plaque, à faible engraissement de point

Toutes les techniques décrites sont compatibles avec la fabrication roll-to-roll (R2R), qui est un processus commercial d'impression de masse qui peut combiner différentes techniques d'impression pour la fabrication de composants et dispositifs complets.

Ici seulement les trois méthodes les plus courantes sont décrites, mais une variété d'autres procédés d'impression différents existent. En règle générale, l'objectif est de fabriquer des dispositifs électroniques flexibles transparents ou semi-transparents, flexibles et même enroulables, tels que les écrans à base de diodes organiques électroluminescentes (OLED) [10], les tags d'identification par fréquence radio (RFID) [11] et les cellules photovoltaïques organiques (OSC) [12].

L'électronique imprimée: l'exemple emblématique de la RFID.

L'internet relie des milliards d'"objets" à l'échelle mondiale, par le biais d'ordinateurs et de périphériques informatiques et de services de toute taille et capacité et des applications fonctionnant sur eux. L'internet of Things (IoT) est un nouveau concept qui peut être considéré comme une grande évolution future de l'Internet avec notamment des interconnexions intelligentes de divers objets dans le monde physique, tels que les véhicules, les téléphones portables, les maisons et les personnes [13]. Pour réaliser cette interconnexion chaque objet physique doit être connecté via des nœuds RF sans fil ou équipés d'étiquettes RFID ou d'autres modes d'identification qui peuvent être détectés par des capteurs intelligents [14].

Pour retourner à l'électronique imprimée, les étiquettes RFID sont un exemple des plus pertinents de dispositifs électroniques flexibles d'ultra grande fabrication de masse avec environ 7 milliards d'étiquettes produites en 2014 [15]. Les systèmes RFID se composent d'un ou plusieurs lecteurs RFID et plusieurs étiquettes [16]. Chaque étiquette est caractérisé par un identifiant unique. Les lecteurs amènent les étiquettes à transmettre en générant un signal approprié, ce qui représente une requête pour leurs identifiants des possibles étiquettes présentes dans les environs. Par conséquent, ils peuvent être utilisés dans une gamme d'applications très large comme c'est le suivi d'objets en temps réel, allant de la logistique à la e-santé et la sécurité [17].

D'un point de vue physique, une étiquette RFID est une petite puce électronique pour la transmission de données sans fil. Elle est généralement fixée à une antenne dans un emballage qui ressemble à un sticker adhésif. Les étiquettes RFID modernes peuvent atteindre une taille inférieure à 0,1 mm^2 [17].

Habituellement, les étiquettes RFID sont passives, ce qui signifie qu'elles n'ont pas de source d'alimentation et récoltent l'énergie nécessaire à la transmission de leur ID à partir du signal de requête transmis par un lecteur RFID à proximité. En effet, ce signal génère un courant dans l'antenne de l'étiquette par induction qui est utilisé pour alimenter la puce électronique qui transmet l'ID de l'étiquette. Habituellement, l'efficacité de cette conversion de puissance est très faible [17]. La plage de fonctionnement des tags RFID est également faible, typiquement 10-50 cm [19]. Des étiquettes RFID peuvent être alimentées aussi par piles classiques, mais dans ce cas les batteries doivent être changées régulièrement.

Toutefois, les étiquettes RFID à base de silicium ne sont toujours pas encore aptes à marquer objets individuels comme prévu par l'IoT. Le marquage d'éléments individuels qui peuvent être jetés après utilisation nécessite des étiquettes qui coûtent seulement quelques centimes d'euro. Bien que le coût d'une puce de silicium ne soit pas un problème et même continue à diminuer avec le facteur d'échelle, la nécessité d'établir des connexions externes entre la puce et l'antenne et éventuellement avec des capteurs, met une limite inférieure au coût total des étiquettes [25]. En outre, ces connexions sont soumises à des possibles défaillances mécaniques si les marchandises sont manipulées sans précautions pendant le transport [24]. Une voie pour résoudre les deux problèmes pourrait être de fabriquer l'étiquette entière, comprenant la puce, l'antenne et les capteurs, sur le même substrat flexible en utilisant la technologie à couches minces [9].

L'électronique imprimée: électrodes souples et transparentes.

Dans tous les cas, le déploiement massif de l'IoT tirera bénéfice de matériaux très souples, adaptables, pliables ou portables. En particulier, les électrodes et les interconnexions conformes sont l'un des éléments clés dans la réalisation de la prochaine génération d'électroniques hautement flexibles [20]. En effet, les applications modernes devraient émerger dans la vie quotidienne, comme par exemple des capteurs imprimés sur les marchandises, des journaux électroniques, les appareils électroniques et les écrans portables [21]. Beaucoup de ces applications à venir exigent une production à faible coût et des électrodes spéciales. Ces électrodes ont besoin d'avoir certaines caractéristiques spécifiques, telles que une flexibilité supérieure, transparence, une conductivité élevée, la stabilité à long terme, etc.

Des candidats prometteurs pour ce genre d'électrodes sont les polymères conducteurs, parmi lesquels une grande attention est accordée au PEDOT ou poly (3,4-éthylènedioxythiophène), qui a été développé dans les années 1980 dans les laboratoires de recherche de Bayer AG en Allemagne [22].

Le PEDOT a une conductivité élevée (~ 300 S/cm), une bonne stabilité dans l'état oxydé et est transparent [23]. Mais il a un grand inconvénient qui est sa faible solubilité.

Le problème de la faible solubilité du PEDOT a été résolu par d'autres recherches en le mélangeant avec du poly(styrène sulfonate) (PSS), soluble dans l'eau. La combinaison

résultante de PEDOT:PSS a donné un système soluble dans l'eau avec de bonnes propriétés filmogènes, une bonne conductivité (~ 10 S/cm), une haute transmissibilité de la lumière visible, et une excellente stabilité. La figure 1.7 montre la structure chimique du PEDOT:PSS. Les films de PEDOT:PSS peuvent être chauffés dans l'air à 100 °C pendant plus de 1000 heures avec un minime changement dans la conductivité [23]. Grace à la combinaison de bonnes propriétés conductrices et à sa transparence, le PEDOT:PSS est largement utilisé pour les cellules solaires comme électrode [24] - [26].

La récupération d'énergie: vers flexibilité.

Notre monde est entouré par une variété de sources d'énergie ignorées. Jusqu'à présent, l'humanité utilise activement les énergies fossiles et l'énergie nucléaire, complétées par l'énergie solaire, l'énergie éolienne et de l'eau. Mais nous pouvons imaginer et trouver les moyens d'utiliser des nouvelles sources d'énergie mineures. Une de ces possibilités est la récupération d'énergie, qui est un processus de capture, transformation, utilisation et/ou stockage de l'énergie électrique utile à partir de sources externes alternatives. La récupération d'énergie est une nouvelle option qui permet de renoncer à l'utilisation des batteries classiques. Elle est destinée à remplacer les sources d'alimentation classiques des systèmes embarqués et l'électronique basse consommation de faible puissance, en produisant ainsi des dispositifs autoalimentés. Il y a beaucoup d'exemples de récupération d'énergie qui sont basés sur l'effet piézoélectrique. Les coefficients piézoélectriques sont utilisés pour comparer les performances de différents matériaux. Nous allons maintenant introduire la piézoélectricité et les différents coefficients piézoélectriques qui la caractérisent.

Introduction à la piézoélectricité et pyroélectricité.

Les matériaux piézoélectriques ont la capacité unique de produire une tension électrique quand une contrainte ou force mécanique est appliquée (effet piézoélectrique direct). De même, l'application d'une tension à travers le matériau provoque sa déformation (effet piézoélectrique inverse). Grâce à ces caractéristiques, les matériaux piézoélectriques sont largement utilisés pour différentes applications telles que les systèmes d'allumage, avertisseurs sonores, des actionneurs et des applications de détection. Aujourd'hui, les

développeurs essaient d'utiliser ces matériaux pour la récolte de l'énergie produite par les vibrations, les mouvements du corps humain, de l'énergie des gouttes de pluie etc.

Piézoélectricité.

La piézoélectricité est caractérisée par des coefficients de proportionnalité entre les valeurs mécaniques et électriques. Étant donné que les matériaux piézoélectriques sont anisotropes, ces coefficients sont déterminés pour chaque direction de l'élément et indexés X_{ij}, avec i correspondant à la direction de la mesure électrique, et j correspondant à la direction de la force mécanique. Les axes de la matière sont numérotés de 1 à 3. La direction de polarisation est généralement faite pour coïncider avec l'axe 3.

Les constantes physiques les plus utilisées pour caractériser un matériau piézoélectrique sont:

- d_{ij} la constante piézoélectrique de charge;

- g_{ij} la constante piézoélectrique de tension;

- k_{ij} le facteur de couplage électromécanique;

- e_{ij} la permittivité diélectrique.

Le coefficient d_{ij} est obtenu en mesurant la densité de charge électrique, qui est créée à la surface du film par une contrainte mécanique appliquée selon l'axe j à un matériau piézoélectrique. La valeur est donnée en C/N. Il donne également la contrainte mécanique subie par un matériau piézo-électrique quand un champ électrique est appliqué. Ce coefficient est habituellement utilisé pour caractériser matériau piézoélectrique pour des applications d'actionnement.

À son tour, le coefficient g_{ij} indique le champ électrique généré lorsque la contrainte mécanique est appliquée selon l'axe j. Elle est mesurée en Vm/N. Ce coefficient est moins connu que d_{ij} mais il est essentiel pour la caractérisation d'un piézoélectrique en mode générateur.

Dans notre travail, nous voulons caractériser et comparer les matériaux piézoélectriques pour des applications de récupération d'énergie. Ainsi, la connaissance de g_{ij}

est essentielle. Nous allons décrire plus tard nos techniques de mesure appropriées pour réaliser des estimations directes de g_{ij}.

Pyroélectricité.

La pyroélectricité est une sous-classe de la piézoélectricité. Les matériaux pyroélectriques sont capables de produire une tension électrique quand ils sont soumis à des changements de température. Ils sont caractérisés par un coefficient pyroélectrique p_i, qui montre les changements dans le vecteur de polarisation spontanée avec la température.

Les matériaux pyroélectriques sont couramment utilisés pour l'imagerie thermique infrarouge et pour des capteurs de température infrarouge sans contact. Ces matériaux peuvent être utilisés comme générateurs pyroélectriques aussi, quand une source constante thermique est présent. Ils peuvent aussi être utilisés pour des applications de récupération d'énergie multimodale, en combinaison avec des propriétés piézoélectriques, pour récolter non seulement l'énergie mécanique, mais aussi thermique, comme a été proposé par notre groupe précédemment [34].

Les matériaux pyroélectriques (et donc piézoélectriques) les plus utilisés sont des matériaux céramiques ferroélectriques polycristallins tels que le titanate de baryum (BaTiO3) et le zirconate titanate de plomb (PZT), parce qu'ils ont l'effet piézoélectrique le plus fort. Récemment, une grande attention a été accordée aux polymères piézoélectriques, qui ont des avantages évidents en termes de propriétés mécaniques (par rapport à des céramiques fragiles) et qui, comme nous avons mentionné précédemment, sont compatibles avec les technologies d'impression.

Polymères piézoélectriques: état de l'art

En 1969, Kawai a découvert que certains polymères, en particulier le fluorure de polyvinylidène (PVDF), présentent un fort effet piézoélectrique [35]. Le PVDF est un matériau semi-cristallin, avec des régions de phases cristallines entourées par des régions amorphes. Le PVDF a quatre phases cristallines principales, connues sous le nom de phase I (β), phase II (α), phase III (γ), et phase IV (δ). La quantité relative de chacune dépend des conditions thermiques, mécaniques et électriques de traitement utilisées pour produire le film

de PVDF. La forme la plus générale est la phase α, qui est une phase non-polaire qui ne possède pas de propriétés piézoélectriques. Seule la phase β, qui est hautement orientée, est responsable des propriétés piézo- et pyroélectriques du polymère [36]. Il a été montré que la phase α peut être convertie en phase β par un étirage mécanique [37], [38].

Afin d'obtenir des propriétés piézoélectriques, la phase β doit être polarisée. La polarisation consiste à appliquer un champ électrique élevé au film pour orienter les dipôles moléculaires dans la même direction. Ceci induit une organisation spatiale des segments de chaînes macromoléculaires [38]. Une combinaison d'étirage et de polarisation fournit un alignement des chaînes moléculaires le long du champ électrique.

Avec des études récentes, un copolymère de PVDF, le poly (fluorure de vinylidène-trifluoroéthylène) (P (VDF-TrFE)), a attiré une grande attention. L'addition de TrFE dans le système de PVDF joue un rôle important dans le comportement de la transition de phase. En raison de la taille de l'atome de fluor supplémentaire, le copolymère se cristalliser directement en phase β. Ainsi, l'étirement supplémentaire n'est plus nécessaire, et ce copolymère peut être utilisé directement pour produire des structures finales à partir de la solution [38]. La structure cristalline du copolymère, le comportement de transition de phase et des propriétés ferroélectriques sont affectées par le rapport de VDF/TrFE et les conditions de synthèse [40].

Le PVDF a un coefficient g_{31} supérieur à celui du P(VDF-TrFE), il produit donc la tension la plus élevée par unité de déformation. Cela est également vrai quand on le compare à d'autres piézoélectriques mais à son tour il est pénalisé par un faible YM. D'autre part, les polymères peuvent se déformer jusqu'à 20 à 30%, tandis que les matériaux céramiques classiques ne peuvent résister que jusqu'à 0.1% de déformation. Cela donne des avantages aux PVDF et P (VDF-TrFE) lorsque de grandes déformations sont nécessaires pour les applications.

Malgré son coefficient g_{31} inférieur, le P (VDF-TrFE) cristallise directement dans la phase β et n'a donc pas besoin d'étirement mécanique. Il est ainsi possible de l'intégrer directement dans des dispositifs électroniques imprimés, ce qui n'est pas possible avec le PVDF. La recherche se concentre sur les techniques pour améliorer propriétés piézoélectriques de P(VDF-TrFE). L'un d'eux est le nanostructuration.

Polymères piézoélectriques: nanostructuration.

Puisque les propriétés piézoélectriques du PVDF et de ses copolymères dépendent directement de la phase β, un grand défi pour les chercheurs est de trouver un moyen d'augmenter sa teneur dans le matériau polymère. Un objectif encore plus difficile est le contrôle des propriétés à l'échelle locale qui peut être critique pour divers dispositifs nanométriques tels que les nano capteurs, les mémoires non volatiles et les nano générateurs. Il existe des travaux qui montrent que le confinement de ces matériaux à l'aide de nanostructures permet un meilleur contrôle de la cristallisation du polymère dans la phase β, et dans certaines circonstances, d'orienter ces cristallites. En effet, la nucléation des cristaux est fortement affectée par le confinement du polymère fondu en petits volumes; les mécanismes impliqués peuvent être soit l'exclusion de noyaux hétérogènes ou l'interaction préférentielle des chaînes avec des interfaces [43]. Il est donc possible de contrôler la cristallisation du polymère et d'augmenter sa teneur d'une phase cristalline particulière par nanostructuration en fonction des conditions de traitement. Ces nanostructures peuvent aussi avoir un grand potentiel pour les applications de stockage d'énergie à haute densité en raison des importantes surfaces mises en jeu par rapport à l'épaisseur du film mince [44]. Différentes techniques ont été appliquées pour produire des matériaux ferroélectriques organique micro- et nanostructurés, comme par exemple la lithographie par nanoimpression (NIL) [43], [45] - [48], qui utilise par exemple une membrane d'alumine anodisée comme un moule de mise en forme [30], [44], ou le dessin directe (par exemple électrofilature) classique [49], [50]. Parmi eux, la nanoimpression thermique est dominante. Elle est particulièrement intéressante avec des polymères thermoplastiques puisque c'est une technique peu coûteuse et rapide pour la préparation de structures à couches polymères sur de grandes surfaces avec des tailles de motifs allant jusqu'à 10 nm [51]. Dans cette technique, la micro et nanostructuration est créée par la déformation mécanique d'un film de polymère fondu par des moyens de pressage avec un moule dur (typiquement de Si).

Le processus se déroule sous vide, pour éviter que l'air soit piégé entre l'échantillon et le moule. L'échantillon est d'abord chauffé à proximité de la température de fusion du matériau. Le moule est ensuite pressé contre lui avec une pression constante de 40 bars pendant typiquement plusieurs minutes, tandis que la température est diminuée. Une fois que la température atteint un certain point bas, la pression est relâchée. L'échantillon est ensuite dissocié du moule.

Le lecteur peut trouver un état de l'art plus complet sur la NIL et des détails sur la thermo-nano-impression comme utilisé dans ce travail dans l'article de Cécile Gourgon [52], la personne qui a été activement impliqué dans ce travail au CNRS-LTM.

En raison de son potentiel, ceci est une voie exploratoire que nous allons prendre plus tard dans ce manuscrit. Des films de P (VDF-TrFE) déposés par sérigraphie sur des électrodes interdigitées seront ensuite nanoimprimés sous forme de fibres. La géométrie de la nano-impression est inspirée de la structure des MFC, des composites à base de macro fibres piézo-céramiques, qui sont des matériaux semi-flexibles de Smart Material Corp. [53]. L'utilisation de ces matériaux piézoélectriques semi-flexibles dans notre groupe [34], [54], [55] a ouvert le chemin vers les matériaux composites intelligents pour la récupération d'énergie que nous gardons la suite ici vers des systèmes entièrement flexibles.

Polymères piézoélectriques: composites avec un alliage à mémoire de forme.

Parmi les différentes sources d'énergie, des sources thermiques sont largement disponibles. Habituellement, l'énergie thermique peut être directement convertie en électricité au moyen de matériaux thermoélectriques [56] (Seebeck effet) ou pyroélectriques [57]. La faisabilité des générateurs thermoélectriques a déjà été démontrée. Cependant, de tels dispositifs nécessitent des grands gradients spatiaux de température et une gestion de la source froide pour être efficaces. Récemment, un autre concept de conversion d'énergie thermique à électrique a été démontrée expérimentalement et validée par notre groupe. Elle consiste à utiliser des structures de composites hybrides composées d'un matériau semi-souple céramique piézoélectrique couplé à un alliage à mémoire de forme (SMA) [55]. Un tel couplage est destiné à la récolte des petites variations lentes de température dans le temps autour d'un seuil de température qui est déterminé par la composition de l'alliage.

Des nombreux alliages métalliques présentent un effet de mémoire de forme (SME). Le fondement de cet effet réversible est l'apparition d'une transformation de phase martensitique. Fondamentalement, un alliage à mémoire de forme est déformé dans la phase martensitique, et la reprise de forme se produit lors du chauffage lorsque l'alliage subit une transformation inverse de la phase martensitique en austénite [58]. Les transformations directe et inverse se produisent dans un intervalle de température donné et sont caractérisées par des températures de début et de fin de transformation. En outre, l'hystérésis thermique

thermodynamique empêche ces intervalles de température de coïncider. En raison de cette transformation, un SMA développe une grande contrainte et de la déformation au chauffage (jusqu'à 600 MPa et 10% pour l'alliage NiTi [59]), qui peut être convertie en énergie électrique par couplage avec un matériau piézo-électrique, avec l'efficacité du couplage caractérisé par le coefficient de couplage k^2.

Puisque les SMA sont capables de produire des déformations élevées (une valeur réaliste est ~ 4%), il est important d'utiliser des matériaux piézoélectriques très flexibles qui peuvent supporter tels niveaux de déformation sans rupture. La combinaison de ces deux matériaux peut être utilisée pour l'élaboration de systèmes de récupération d'énergie flexibles. Au cours de ce travail, nous avons réalisé un prototype de récupérateur d'énergie par hybridation du P(VDF-TrFE) avec un SMA à base de NiTi.

Résumé des objectifs de ce travail.

L'objectif principal de ce travail est de démontrer la faisabilité d'une structure composite intelligente souple thermique capable de détecter et de récolter l'énergie d'événements thermiques non-continus, lents et faibles en produisant un démonstrateur fonctionnel. Ici nous avons cherché à hybrider des nouveaux microgénérateurs piézoélectriques à base de P(VDF-TrFE) sérigraphié et de feuilles existantes de SMA à base de NiTi.

On a passé rapidement en revue des approches différentes de la récupération d'énergie en utilisant des matériaux flexibles piézoélectriques. Ceci est un domaine en pleine expansion avec de nombreuses applications commerciales possibles. L'utilisation de polymères permet de nouvelles fonctionnalités où la tenue à des grandes déformations et la légèreté sont nécessaires. Le P (VDF-TrFE) est le candidat polymère piézo-électrique le plus approprié pour le dépôt par sérigraphie et l'intégration, et il est bien adapté pour de telles applications. En outre, il est possible d'améliorer encore ses propriétés par des techniques telles que la lithographie par nanoimpression.

Dans ce travail, nous avons décidé d'utiliser des nouvelles encres formulées de P(VDF-TrFE) pour la sérigraphie, en collaboration avec le Liten et la société Arkema. C'était un véritable défi au départ que de fabriquer des nouveaux microgénérateurs piézoélectriques flexibles efficaces sur des substrats en plastique. Le deuxième défi était d'évaluer dans des

conditions réalistes les capacités de récupération d'énergie de ces microgénérateurs en mesurant d'abord la tension piézoélectrique et l'énergie sans pertes parasites.

L'objectif ultime était de produire une preuve fonctionnelle du concept d'un récupérateur entièrement flexible, capable de détecter des événements thermiques non-continus, ou lents et faibles, qui in fine pourraient être des événements tels que des petits changements de température dans l'air ambiant ou à cause du contact avec la peau. En outre, le cadre de ce travail inclut aussi l'établissement des briques de base pour la réalisation ultérieure d'un capteur sans fils autonome thermique complet. C'est pourquoi des directions d'amélioration faisaient partie des objectifs finaux, tant du point de vue des matériaux, que du circuit de gestion de l'alimentation et de la transmission sans fil.

Proc*édé de fabrication de microgénérateurs piézoélectriques flexible.*

Ce paragraphe présente les matériaux et les méthodes utilisés pour préparer les échantillons de cette thèse. L'intégralité du processus de fabrication des microgénérateurs piézoélectriques flexibles y est aussi détaillée. Le travail expérimental est principalement basé sur le copolymère de PVDF. Le résultat principal de cette section est le dépôt de multicouches à base d'encre P(VDF-TrFE) par sérigraphie. En suivant la chronologie et l'avancement des travaux de dépôt, nous commençons avec une simple structure de condensateur unique et continuons avec la conception et la fabrication d'un réseau de condensateurs connectés en parallèle au format carte de crédit pour le démonstrateur. Au-delà de ce travail, et pour avoir une vision plus large, un travail exploratoire a été engagé avec des nouvelles encres de terpolymère P(VDF-TrFE-CTFE). En particulier, des hétérostructures originales de P(VDF-TrFE) et P(VDF-TrFE-CTFE) ont été réalisées pour la première fois. Finalement, différents matériaux d'électrode (argent, or et PEDOT: PSS) ont été comparés pour étudier comment ils affectent la qualité et la morphologie des films piézoélectriques déposés.

Dans notre travail, la fabrication des échantillons est confrontée à deux défis. Le premier consiste à développer des étapes technologiques en amont et l'autre est de proposer un process flow qui répond aux besoins de l'industrie. C'est pourquoi la fabrication des échantillons a été réalisée sur la plate-forme Pictic du Liten qui est dédiée au transfert industriel des nouvelles technologies imprimés.

Pictic possède des installations de recherche pour l'électronique flexible avec une salle blanche de classe 10'000 de 400 m^2. Elle dispose de plusieurs équipements pour la fabrication et la caractérisation des matériaux, y compris un appareil de sérigraphie automatique.

Process flow

Tout d'abord, 30 nm Au pour l'électrode inférieure ont été déposés sur le substrat organique souple d'épaisseur 125 µm en utilisant une machine de dépôt physique par vapeur (PVD) Alcatel SCM600. Un masque physique a été utilisé pour le transfert des motifs sur le substrat.

Les couches de co- et terpolymères ont été déposées à partir d'encres par sérigraphie. Les épaisseurs totales ont varié de 1.1 à 3.9 µm en fonction du nombre de couches déposées. Ensuite, les échantillons ont été séchés en deux fois, d'abord pendant 3 minutes à 60 °C sur une plaque chauffante, et puis pendant 10 minutes dans un four à infrarouges à 120 ° C pour les terpolymères et à 130 °C pour les copolymères. Ces températures et temps satisfont les conditions d'élimination de solvant et la cristallisation de la phase β piézoélectrique du P(VDF-TrFE) [60]. La première étape de recuit à 60 °C a été introduite pour diminuer le choc thermique sur les échantillons. Sans ce recuit préliminaire, nous avons observé la formation de fissures dans la couche de P(VDF-TrFE).

La prochaine étape est le dépôt des électrodes supérieures par sérigraphie. Deux matériaux différents ont été utilisés pour les électrodes: une pâte d'argent (5 µm) ou du PEDOT:PSS (400 nm). Après le dépôt, les électrodes ont été séchées de la même manière que les couches à base de PVDF.

La dernière étape est l'encapsulation des échantillons avec les électrodes supérieures en PEDOT:PSS. Les motifs étaient couverts par un revêtement organique de protection de 1 µm par sérigraphie. Cette couche est nécessaire pour protéger le PEDOT:PSS puisqu'il est très sensible à l'humidité [61], [62], [63] afin de le maintenir sur des conditions de fonctionnement optimal pour une longue période.

Le polyéthylène téréphtalate (PET) et le polyéthylène naphtalate (PEN) constituent les deux principaux substrats souples transparents utilisés aujourd'hui dans le développement de l'électronique flexible. Non seulement ils offrent une bonne résistance aux solvants et une

tolérance correcte à la température, mais aussi leur transparence intrinsèque les rend appropriés comme substrats pour l'électronique transparente [64]. Grace à leur faible résistance à la traction et à un allongement à la traction élevée les deux substrats peuvent être utilisés pour l'électronique flexible. Puisque pour notre fabrication nous utilisons traitement thermique jusqu'à 130 °C, nous avons choisi le PEN, car sa température de travail est plus élevée (160-180 °C).

Avec un film piézoélectrique il faut au moins une électrode inférieure est nécessaire pour d'abord polariser, puis actionner ou récolter les charges générées induites par contrainte. Habituellement, l'électrode inférieure est réalisée directement sur le substrat pour faciliter la fabrication. Classiquement, elle est faite d'une métallisation d'or. L'or est approprié car il permet l'utilisation d'électrodes conductrices très minces qui sont semi-flexibles. De plus, la faible épaisseur est une condition importante pour un dépôt correct du film piézoélectrique. En effet, une électrode épaisse peut créer une topologie qui est difficile à couvrir complètement sans l'apparition de défauts tels que des fissures latérales, des contraintes résiduelles, etc.

Pour cette raison, nous avons fait le choix d'utiliser 30 nm d'or pour les électrodes inférieures, déposés sur un substrat PEN en utilisant PVD avec masque d'ombre. Avant le dépôt par sérigraphie de la couche piézoélectrique, une étape nécessaire est la formulation de l'encre. Dans notre cas il s'agit d'une solution de P(VDF-TrFE) 15% wt en cyclopentanone avec un VDF:TrFE rapport massique de 75:25%. Il a été préparé en mélangeant avec un agitateur magnétique pendant 24 heures à 80 °C. La grande innovation de ce travail est que nous utilisons la dernière poudre de polymère électro-actif d'Arkema / Piezotech, France.

Ensuite, le matériau a été sérigraphié avec une unité Ekra Asys Group à température ambiante. Les paramètres de dépôt étaient les suivants: vitesse de squeegee de 200 mm/s, pression de 8 N. L'encre préparée a été placée sur l'écran manuellement avec une seringue, et ensuite transmise au substrat par le squeegee contrôlée par la machine.

L'épaisseur typique ciblée était de quelques microns. L'épaisseur minimale (1.3 µm) a été limitée par la sérigraphie. L'épaisseur maximale (3.9 µm) a été limitée dans notre travail par le champ électrique nécessaire au processus de polarisation, typiquement, 100 V/m pour polariser un film de P(VDF-TrFE) (plus de détails dans le chapitre 3). Des films d'épaisseur de plusieurs microns seront donc difficiles, voire impossibles à polariser avec l'équipement existant en raison de la forte tension électrique qui serait nécessaire pour obtenir le champ

souhaité. C'est pourquoi notre objectif était de 4 µm au maximum pour être sûrs qu'ils peuvent être polarisés avec les équipements à notre disposition.

Des électrodes supérieures ont été déposées pour la polarisation et la collecte des charges. Nous avons donc utilisé une structure de condensateur à plaques en métal-isolant-métal (MIM). Dans ce travail, ces électrodes supérieures ont été déposées par sérigraphie. On a testé différents matériaux. Nous avons commencé avec de la pâte d'argent spécialement formulé pour la sérigraphie (~ 5 µm d'épaisseur) (NovaCentrix HPS 021LV [67]). Ensuite, nous avons utilisé un matériau organique plus avancé, à savoir une solution aqueuse de PEDOT:PSS Clevios ™ S V4, Heraeus, Allemagne (~ 0.4 µm d'épaisseur). Sa viscosité varie entre 15-60 dPas, et sa résistivité est de 400 Ohm/sq [68]. Après sérigraphie, le PEDOT:PSS a été séché de la même façon que les couches piézoélectriques.

Le PEDOT:PSS présente de nombreux avantages (électriques, optiques et mécaniques), mais il est sensible à l'environnement (humidité et d'oxygène) et n'est pas stable dans le temps sans protection. Par conséquent, ici, nous avons utilisé un matériau organique de protection (~ 1 µm d'épaisseur). La couche de protection est composée de grands motifs simples (carrés ou rectangulaires) couvrant l'ensemble de la zone microgénérateurs, à l'exception de la zone de connexion.

Avec la sérigraphie, l'épaisseur de la couche déposée dépend habituellement de la viscosité de l'encre et les paramètres de la machine (vitesse et de pression du squeegee, etc.). Avec les encres d'Arkema à base de PVDF, l'épaisseur de film minimale pratique est d'environ 1 µm. Cependant, pour des applications de récupération d'énergie, la figure de mérite est la densité d'énergie, qui augmente avec la capacité et la tension au carré ($E = ½ CV^2$). L'épaisseur du matériau piézoélectrique t est une variable qui change à la fois la capacité (en cas de condensateur à plaques $C=\varepsilon\cdot\varepsilon_0\cdot S/t$) et la tension de sortie ($V=g_{ij}\cdot\sigma\cdot t$).

Pour contrôler l'épaisseur, nous avons développé un processus de dépôt multicouche utilisé pour la première fois avec les encres à base de P(VDF-TrFE) et P(VDF-TrFE-CTFE). Le procédé consiste à déposer chaque couche par sérigraphie au-dessus de la précédente après le séchage. Le nombre d'alternances testé ici est compris entre 1 et 3. Les épaisseurs totales ont varié de 1.1 à 3.9 µm en fonction du nombre de couches déposées. La cristallisation a été effectuée par un recuit après chaque couche déposée.

La mesure de l'épaisseur totale des multicouches et l'observation des interfaces entre les couches sont des questions importantes pour les applications, car les performances du matériau peuvent en dépendre. Par conséquent, cela a été fait par une combinaison de profilométrie de surface, coupe transversale spéciale par microtomie, et microscopie électronique à balayage (MEB).

L'observation MEB de polymères nécessite une préparation spéciale de l'échantillon. Pour voir une section des films et multicouches, de petites coupes transversales ont été préparées par microtomie. Dans ce procédé, l'échantillon est placé à l'intérieur d'une matrice en caoutchouc dur et ensuite coupé avec une lame de diamant. Ensuite, les échantillons ont été recouverts de carbone par évaporation par faisceau d'électrons pour rendre la surface conductrice pour la visualisation MEB. Ceci évite d'accumuler des charges électriques sur les échantillons sous exposition à un faisceau et par conséquent limite la fusion locale du polymère. Ces images MEB permettent de conclure que le dépôt multicouche sérigraphié de P(VDF-TrFE) est uniforme, ne présente pas d'interface entre des dépôts successifs et produit des films cristallisées de façon homogène sans fissures ou d'autres défauts, et qui sont adaptés pour les applications.

Le principal résultat du travail expérimental est ainsi la réalisation d'un processus de sérigraphie reproductible de matériaux à base nouvelles encres de P(VDF-TrFE), y compris le dépôt de multicouches. Nous rapportons l'absence de couches mortes, de défauts aux interfaces ou des hétérogénéités de la microstructure du film. En revanche, nous avons montré que le matériau d'électrode supérieure est une question importante car il peut causer des dommages structurels néfastes sur le film piézoélectrique. Ainsi, un process flow fonctionnel a été créé pour la fabrication de microgénérateurs piézoélectriques flexibles.

La conception des échantillons d'essai a été décrite. Elle est principalement basée sur le modèle du condensateur à plaques pour les films continus, mais on a aussi dessiné un système interdigital alternatif pour les films nanostructurés à venir plus tard. Le design pour les films continus a évolué depuis des structures de test à condensateur unique pour l'étude du matériau vers une structure en réseau de condensateurs parallèles sur un format de carte de crédit pour les applications. La fabrication de prototypes a été complètement terminée.

Enfin, nous avons ouvert de nouvelles directions de recherche et présenté un résumé des travaux d'exploration technologique sur des hétérostructures originales de P(VDF-TrFE) et P(VDF-TrFE-CTFE), également produites par sérigraphie.

Propriétés ferroélectriques.

Le PVDF et son copolymère P(VDF-TrFE) présentent de fortes propriétés ferroélectriques [84]. Puisque tous les matériaux ferroélectriques sont également piézoélectriques (en raison de la symétrie cristalline), il est nécessaire d'étudier les deux propriétés pour donner une analyse complète du matériau. La ferroélectricité dans le PVDF est causée par les dipôles qui se polarisent spontanément et alignent avec le champ électrique externe. La polarisation des dipôles peut être changée vers la direction opposée avec l'inversion du champ électrique. Souvent, les mesures ferroélectriques sont effectuées avant la caractérisation piézoélectrique afin de faire une première évaluation de leur potentiel et leur pertinence pour des applications telles que des générateurs, des capteurs et des actionneurs [32], [85] - [88].

Afin d'obtenir et de stabiliser les propriétés ferroélectriques, le PVDF et ses copolymères doivent être polarisés. Il existe plusieurs méthodes de polarisation pour les polymères tels que la polarisation par électrode (également appelé de polarisation thermique), polarisation corona et polarisation par faisceau d'électrons.

La plupart des tests ont été effectués sur la station analyseur sous pointes aixACCT TF 2000E qui dispose d'un module pur mesures ferroélectriques. Toutes les mesures ont été réalisées à température ambiante. Les échantillons à mesurer correspondent aux structures de test des capacités MIM présentés auparavant. Les contacts pour les pointes ne se fait pas sur la structure même, mais sur des pads de connexion déportés, ce qui évite d'endommager ou perforer les structures multicouche du condensateur.

La polarisation des échantillons a été effectuée à température ambiante par polarisation par électrode à l'aide de pointes de connexion. Pour ce faire, nous utilisons la tension de polarisation maximale de l'équipement (400 V), en générant un champ électrique de manière uniforme et normale aux électrodes. Compte tenu de l'épaisseur des échantillons, ceci correspond à un champ électrique supérieur à 100 V/µm, qui est la valeur recommandée pour polariser complètement les films de P(VDF-TrFE) [86]. On notera que dans le cas des électrodes d'argent le champ est limité à des valeurs plus faibles (~ 45 V/µm) en raison de « points chauds » associés aux défauts de structure et préalablement identifiés menant à la dégradation rapide des échantillons. La tension a été allumée et éteinte instantanément, sans rampe. Divers temps de polarisation, de 1 s à 30 min, ont été testés et pratiquement aucun impact n'a été trouvé.

Deux types de matériaux ont été testés pour les électrodes supérieures (encre Ag et PEDOT: PSS). Les condensateurs avec électrode supérieure en PEDOT:PSS ont montré une plus faible densité de courant de fuite et aucune détérioration électrique jusqu'à 400 V. En revanche, les échantillons avec électrode supérieure en argent avaient des fuites et étaient défaillants à partir de 100 V. Par conséquent, il a été conclu que le PEDOT:PSS est le matériau d'électrode le plus approprié pour continuer ce travail.

Des conditions de polarisation optimales ont été trouvés pour les échantillons de P(VDF-TrFE) conduisant à une valeur de polarisation rémanente P_r remarquable de 7,5 $\mu C/cm^2$, indiquant un ordre ferroélectrique élevé (FE). A l'opposé, les échantillons de P(VDF-TrFE-CTFE) terpolymère ont montré un comportement relaxeur, avec des faibles valeurs de P_r et un cycle d'hystérésis pincé.

Un résultat clé est la confirmation électrique du succès dans la réalisation de multicouches par sérigraphie sans couches mortes ou interfaces déficientes. En ce qui concerne les hétérostructures exploratoires de P(VDF-TrFE) et P(VDF-TrFE-CTFE), produites pour la première fois par sérigraphie multicouche, les mesures ont montré un bon accord avec les calculs théoriques de capacité parallèle. Toutefois, le comportement ferroélectrique était complexe à cause des cycles d'hystérésis pincés, et une compréhension plus poussée des phénomènes mis en jeu dans ces systèmes RE/FE est en dehors du cadre de cette étude.

Propriétés piézoélectriques.

La mesure de la tension piézoélectrique de façon directe est réalisée avec l'introduction d'un interrupteur mécanique dans le circuit de mesure, qui sépare la génération des charges (lorsque la contrainte est appliquée) de leur récupération (lorsque la contrainte est arrêtée). L'interrupteur est maintenu à l'état ouvert lors de la déformation mécanique, tandis que les charges produites s'accumulent dans la structure de condensateur. Lorsque la déformation est terminée, l'interrupteur est fermé et toutes les charges collectées sont transférées d'un seul coup dans le circuit de mesure.

La tension de sortie a été mesurée avec soit un oscilloscope Agilent Technologies DSO1014A, soit avec un voltmètre électrostatique TREK 370. Ce dernier mesure le potentiel électrostatique de surface de l'échantillon sans contact physique, ce qui rend l'impédance d'un

tel système pratiquement infinie, en éliminant le problème d'adaptation d'impédance pour la mesure de tension. En effet, une potentielle fuite des charges électriques peut avoir lieu (et arrive) sur l'impédance d'entrée de l'oscilloscope.

Pour effectuer la caractérisation piézoélectrique directe de nouveaux matériaux et structures, il est nécessaire d'appliquer la contrainte de façon bien contrôlée et avec une grande précision. A cet effet, trois méthodes mécaniques ont été étudiées, et spécialement adaptés pour les polymères:

- Mesures par impact de goutte d'eau;
- Flexion quatre points;
- Flexion sur tube.

Deux types d'échantillons ont été utilisés. Afin d'avoir un point de comparaison avec les valeurs théoriques, le premier type d'échantillons caractérisés est basée sur de PVDF commercial de 40 μm d'épaisseur (Piezotech). Les échantillons pour des tests de flexion quatre points sont faits d'un petit morceau de PVDF de 1x1.5 cm^2 collé sur une plaque de plexiglas de 1.1 mm d'épaisseur avec un adhésif époxy (Scotch-Weld ™). Ces échantillons seront appelés "Piezo-40". Les deuxièmes échantillons sont basés sur les condensateurs simples sérigraphiés (Design-1) de ce travail, préparés d'une manière similaire. La face arrière du substrat PEN a été collée sur la plaque de plexiglas, et le lien entre les électrodes et les fils externes a été réalisée sur la face supérieure au moyen de pâte d'argent et ruban de cuivre.

Les échantillons en réseau de condensateurs connectés en parallèle (Design-2) ne peuvent pas être testés par flexion quatre points, en raison de la limitation de taille de l'équipement. Ils ont été testés par flexion en tubes (sans substrat supplémentaire).

Les échantillons Piézo-40 ont été testés par goutte d'eau, tube et flexion 4-points afin de déterminer la tension de sortie, le coefficient g_{31}, et la densité de l'énergie dans des conditions de circuit ouvert. Ces méthodes ont été comparées en termes de réponse piézoélectrique, répétabilité des résultats et facilité d'utilisation. Parallèlement à des mesures expérimentales, il est essentiel d'effectuer des estimations théoriques de la tension de sortie directe afin de le comparer avec les résultats obtenus.

Dans l'expérience d'impact de goutte d'eau, la tension produite par goutte était de 600 mV. Sur cette base, le de coefficient de couplage k_T a été estimé à 0.26% avec l'équation (4.4). Par rapport à la valeur de la datasheet (10%), ce résultat est très faible, ce qui peut être

dû à des difficultés dans l'estimation de l'énergie mécanique réelle qui est transférée à l'échantillon (en raison de phénomènes de mouillage, de forme non uniforme de la goutte). En outre, il peut être dû aux fuites électriques dans la mesure, puisque la méthode "switch" n'était pas encore utilisée à ce point du travail. Nous nous sommes tournés donc vers des méthodes plus appropriées. Cependant, la méthode de mesure par impact de goutte d'eau peut être utilisée pour des simulations de récolte d'énergie réelle avec des fluides tels que la pluie.

La méthode de flexion sur tube est plus simple à réaliser et conduit à une plus grande déformation (1%) et il est possible de caractériser des échantillons de différentes tailles, mais elle est moins précise et reproductible. D'autre part, le procédé de flexion en quatre points est automatisée, avec une répétabilité élevée, et applique une déformation plus uniforme, mais la déformation était limité à 0.5% avec l'équipement dont nous disposons. Avec ces deux méthodes, nous avons obtenu des résultats supérieurs à ceux de la littérature dans des conditions de génération des charges en circuit ouvert. Par exemple, avec l'échantillon Piézo-40, on a obtenu une valeur record de 80 V à 1% de déformation, qui est la tension piézo-électrique la plus élevée observée dans la littérature avec un matériau à base de PVDF.

Les résultats expérimentaux correspondent bien avec les calculs théoriques, ce qui signifie que les deux méthodes sont appropriées à la caractérisation piézoélectrique et peuvent donc être utilisés pour l'estimation précise du coefficient g_{31}. Il y a une légère différence de la tension autour de quelques volts, qui peut être expliqué par la précision du calcul de la déformation ainsi que par la précision des valeurs dans la datasheet (qui est ± 20%).

Tout d'abord, les différentes méthodes d'application de contrainte pour des matériaux très souples ont été proposées et testées. Les méthodes de flexion quatre points et de flexion sur tube ont été choisis comme les plus appropriées. La validation des méthodes a été réalisée avec du PVDF connu de qualité commerciale conduisant à une bonne répétabilité, et en accord avec les valeurs théoriques.

Deuxièmement, des méthodes améliorées pour des mesures de tension piézoélectrique directe en circuit ouvert ont été proposées en utilisant soit voltmètre électrostatique sans contact soit interrupteur mécanique (et un oscilloscope). On a validé la fiabilité des deux méthodes. De ces expériences, nous avons obtenu une valeur exceptionnelle de tension piézoélectrique maximale pour le PVDF commercial avec 80 V à 1% de déformation. Ces méthodes permettent également l'évaluation directe du coefficient piézoélectrique g_{31} qui peut être calculée à partir de la dépendance déformation-tension observée. La valeur a été établie à

0.07 V·m/N ± 15% pour le PVDF commercial contre une valeur de datasheet de 0.06 ± 20% V·m/N (méthode indirecte).

Un autre résultat clé de ce chapitre est l'évaluation de g_{31} pour des films minces sérigraphiés de P(VDF-TrFE), ce qui est montré pour la première fois. La valeur déclarée est de 0.15 V·m/N ce qui représente Il est deux fois la valeur du P(VDF-TrFE) commercial. Grace à ce coefficient élevé, les microgénérateurs de P(VDF-TrFE) imprimé ont été capables de produire des tensions jusqu'à 10 V à 0.4% de déformation, ce qui correspond à une densité d'énergie de 480 $\mu J/cm^3$, limitée ici seulement par les conditions expérimentales. Densités d'énergie plus élevées sont possibles avec l'application de plus grandes déformations.

En outre, la caractérisation pyroélectrique directe des microgénérateurs en P(VDF-TrFE) imprimé a été réalisée. Un coefficient pyroélectrique ρ_Q de -25 $\mu C/Km^2$ a été mesuré, en bon accord avec la fiche technique.

Par conséquent, cet important chapitre se termine avec des éléments positifs de décision pour l'application de récupération d'énergie thermique qui était ciblée, grâce à la fabrication réussie de microgénérateurs piézo- pyroélectriques souples de haute efficacité avec du P(VDF-TrFE) sérigraphié.

Harvester thermique souple.

Dans cette partie, nous présentons les résultats électriques du premier récupérateur thermique composite entièrement flexible. La structure composite est constituée de P(VDF-TrFE) imprimé et d'un alliage à mémoire de forme thermique (SMA). Le couplage mécanique entre P(VDF-TrFE) et SMA permet la génération simultanée d'une réponse pyro et d'une réponse piézoélectrique à partir d'une source thermique unique. Cela contraste avec des générateurs uniquement piézoélectriques ou pyroélectriques qui ne peuvent bénéficier d'effets supplémentaires (pyro + piézo) que lorsque les deux sources appropriées sont présentes (thermique + mécanique). De cette façon, nous pouvons dire que le composite de ce travail appartient à la classification des multiferroïques car elle implique un double caractère ferroïque, à savoir ferroélectrique et d'effet de mémoire de forme.

Deux principaux fournisseurs de matières SMA ont été identifiés dans le cadre de ce travail. Le premier est Nimesis, France [108]. Cette société fournit principalement des fils à

base de NiTi ayant des diamètres différents (0,1 à 2 mm). En ce qui concerne notre but de démonstration, nous avons préférés des grands éléments SMA. Ils ont été fournis par MEMRY, Allemagne [109] sous la forme de feuilles (100 µm d'épaisseur), à partir desquels des éléments de format de carte de crédit peuvent être facilement découpés.

Le prototype de composite flexible a été réalisé par l'assemblage des deux éléments sur un format de carte de crédit. Le premier élément est le microgénérateur sérigraphié avec un réseau de capacités connectées en parallèle de 2.6 µm d'épaisseur de P(VDF-TrFE). Le deuxième élément est une feuille de 100 µm d'épaisseur de NiTi MEMRY avec une température de transition de 65 ºC. Il a été collé sur le côté arrière du substrat PEN du microgénérateur avec de la colle époxy. Cette colle a été choisie parce qu'elle présente une déformation de cisaillement maximale élevée, ce qui est compatible avec notre application [110]. En outre, elle peut sécher à la température ambiante, ce qui est une condition importante pour assembler le composite à une température inférieure à celle de l'état chaud du SMA (65 °C). Avant le collage, les deux éléments ont été nettoyés avec l'isopropanol. Ensuite, la colle a été appliquée sur les deux surfaces, puis les deux surfaces ont été pressées ensemble. Afin de sécher complètement la colle, le composite a été maintenu à l'intérieur de la presse pendant au moins 24 heures à température ambiante.

Pour évaluer les composites préparés et observer l'effet de l'addition de la couche de SMA, il était nécessaire de chauffer les échantillons à la température de travail du SMA, de manière bien contrôlée et mesurable. Plusieurs méthodes ont été testées par notre groupe, y compris le chauffage électrique par courant [111], le chauffage par bain eau / huile thermostatique [112] et le chauffage par flux d'air [113]. Chaque méthode a ses propres avantages et inconvénients, et peut être utilisé en fonction des conditions de travail et la configuration composite. Ici nous avons utilisé la méthode par flux d'air afin d'être plus proche de l'environnement d'application réel (flux de chaleur). Il a produit des résultats reproductibles.

Pour générer le flux d'air de 65 ºC, un sèche-cheveux classique a été utilisé. Il a été initialement préchauffé pendant 5 secondes. On l'a ensuite placé sur l'échantillon à une distance de 20 cm et maintenu pendant 10 secondes pour parvenir à une distribution de température homogène. Le débit d'air a été appliqué du côté du microgénérateur composite.

Le SMA nécessite d'être pré-tendu à l'état froid (martensite) pour que la transformation induite thermiquement ait lieu. Ici, pour induire la pré-contrainte, la flexion en

tube a été utilisée (comme décrit dans le chapitre 4). Nous avons utilisé des tubes de 84 mm et 50 mm de diamètre autour desquels le composite était pliée (face SMA vers le bas). Puis, lors du chauffage, le composite est retourné dans son état initial (plat), produisant ainsi au même temps de la tension piézo et pyroélectrique.

Afin de simplifier la mise en œuvre électrique du démonstrateur, le composite utilisé ne subit qu'une transformation à sens unique. Cette situation vaut pour les applications de sécurité thermique (indicateur de seuil de température) où l'élément de sécurité doit être utilisé qu'une seule fois. Pour utiliser les transformations réversibles ou encore pour aller vers la récupération d'énergie de cyclage thermique (chauffage et refroidissement), le composite a besoin d'une force de rappel (effet de ressort) pour le ramener à l'état froid pré-déformé. Cela a été démontré dans [59]. Les raideurs et épaisseurs du SMA et du substrat du microgénérateur peuvent être optimisées pour favoriser l'effet de ressort du substrat. Lorsque des déformations dans le plan sont préférées, la pré-contrainte sur le SMA peut être appliquée à l'aide d'une source de traction, par exemple une machine de traction, mais pour le cas présent ceci n'a pas été possible puisqu'il aurait fallu des supports spéciaux avec les grands échantillons utilisés. Alternativement, on pourrait aussi utiliser du SMA avec effet mémoire dans les deux sens, qui n'aurait pas besoin d'une force de rappel externe pour revenir à l'état froid.

Pour mesurer la tension produite avec la structure composite, nous avons utilisé l'oscilloscope avec l'interrupteur, comme décrit dans le chapitre 4. Cependant, les différentes contributions à la tension ont été séparées:

- la tension pyroélectrique est mesurée avec le composite non contraint, par simple chauffage de l'échantillon avec le flux d'air, tout en gardant l'interrupteur ouvert. Après 10 s de chauffage, l'interrupteur est fermé et la tension de crête est enregistrée.

- la tension piézoélectrique est mesurée par flexion du composite sur un tuyau à température ambiante. L'interrupteur est maintenu ouvert pendant la flexion, et fermé une fois la flexion est terminée.

- la réponse composite tension pyro/piézoélectrique combinée: pour bénéficier de la transformation de phase du SMA, le composite est pré-tendu (traction) par une flexion sur tube puis déchargé. Ensuite, la procédure pour le cas pyroélectrique est répétée. Pendant son chauffage le composite subit les effets combinés de la pyroélectricité et la piézoélectricité au

moyen de la déformation du SMA et produit une tension accrue. Il est à noter que les deux tensions sont négatives dans l'expérience et donc s'additionnent.

Nous avons donc réalisé et validé un nouveau concept de composite flexible pour la récupération d'énergie thermique à base de films minces de P(VDF-TrFE) sérigraphié et de feuilles de SMA. Ses capacités de génération de tension et de récupération d'énergie ont été mesurées en fonction de la déformation. Le composite génère bien une tension à la fois pyro et piézoélectrique et a atteint des tensions de sortie jusqu'à 37 V à 65 ºC avec une pre-déformation du SMA de 0.56%. L'énergie électrique correspondant était de 95 μJ, ce qui correspond à une densité d'énergie de 19 mJ/cm^3. Ces valeurs ont été ensuite mises en perspective pour ce point de fonctionnement en les comparant aux exigences très récentes sur la consommation d'énergie des dispositifs pour l'IoT. Nous avons conclu que nos harvesters composites thermiques sont déjà adaptés pour les applications de l'IoT.

Enfin, une combinaison de nanostructuration et d'électrodes interdigitées a été explorée par nano-impression de P(VDF-TrFE) sérigraphié pour imiter des MFC (appelée NFC). Le travail technologique a été un succès et les tests électriques préliminaires ont montré une augmentation de la polarisation rémanente avec des structures nanoimprimées. Cependant, la réponse piézoélectrique n'a pas pu être encore évaluée.

Conclusions générales.

La réalisation principale de cette thèse est la conception, la fabrication et l'évaluation d'un récupérateur thermique composite basé sur microgénérateurs souples à base de P(VDF-TrFE) sérigraphié, couplé avec un alliage à mémoire de forme en NiTi. Le composite, de la taille d'une carte crédit, est capable de générer de l'énergie électrique à partir de variations de temporelles température quasi-statiques, et produit jusqu'à 95 μJ d'énergie utile de sortie lors d'un chauffage de la température ambiante jusqu'à 65 °C. Ceci correspond à une densité d'énergie de 19 mJ/cm^3, compatible avec des applications telles que les étiquettes RFID ou les cartes de transmission sans fil basse consommation.

On a réussi la fabrication de microgénérateurs avec un procédé de sérigraphie reproductible avec de nouvelles encres de P(VDF-TrFE). Un process flow fonctionnel a été créé pour la fabrication de microgénérateurs piézoélectriques flexibles multicouches, sans couches mortes, sans défauts d'interface et avec une homogénéité de la microstructure du

film. Des dessins de structures simples de test avec des condensateurs pour l'étude du matériau, ainsi que le dessin de structures de réseau de condensateurs montés en parallèle sur un format de carte de crédit pour le prototypage ont été réalisés.

Le coefficient de tension piézoélectrique g_{31} des films minces de P(VDF-TrFE) sérigraphiés a été mesuré directement et rapporté pour la première fois, atteignant 0.15 V·m/N pour la structure en réseau, soit le double de celle du P(VDF-TrFE) commercial. Les microgénérateurs produisent des tensions piézoélectriques induites par contrainte inférieur à 10 V avec une densité d'énergie de 480 $\mu J/cm^3$ à 0.4% de déformation, ici limitée par les conditions expérimentales. En outre, le coefficient pyroélectrique ρ_Q du réseau de microgénérateurs sérigraphié a été mesurée à -25 $\mu C/Km^2$, en bon accord avec la littérature.

Pour effectuer des caractérisations piézoélectriques, deux méthodes de mesure originales ont été proposées, permettant des mesures en conditions de circuit ouvert sans pertes de tension piézoélectrique à l'aide d'un voltmètre électrostatique sans contact et un interrupteur mécanique. Les deux méthodes ont été prouvés de donner des résultats fiables, permettant d'atteindre des valeurs remarquablement élevées de tension.

Les conditions de polarisation optimales du P(VDF-TrFE) sérigraphie ont été trouvées. Des valeurs de P_r élevée (~ 7.5 $\mu C/cm^2$) et de E_c intermédiaire (40 V/μm) ont été obtenues pour les microgénérateurs simples et le réseau de condensateurs connectés en parallèle, en indiquant un ordre ferroélectrique élevé.

Deux types d'électrodes supérieures (encre argent et PEDOT:PSS) ont été comparées: les microgénérateurs avec PEDOT: PSS ont montré de meilleures performances en termes de densité de courant de fuite. En outre, les échantillons avec des électrodes supérieures en argent subissent des pannes électriques pendant les mesures, qui ne sont pas observées pour les échantillons avec PEDOT:PSS. Nous concluons donc que le PEDOT:PSS est mieux adapté pour le dépôt par sérigraphie sur des polymères, et il a été utilisé pour le prototypage des dispositifs pour la récupération d'énergie.

Concernant les travaux d'exploration entrepris dans cette thèse, des structures de nanoimpression ont été réalisées à la fois sur en film bulk et sur des couches minces de P(VDF-TrFE). Les conditions optimales ont été trouvées, permettant d'obtenir des motifs de lignes de 500 nm uniformes. Des tests préliminaires ont montré une augmentation de la

polarisation rémanente, mais d'autres tests sont nécessaires pour mesurer sa réponse piézoélectrique.

Des hétérostructures imprimés de P(VDF-TrFE) et P(VDF-TrFE-CTFE) ont été réalisées pour la première fois. Le P(VDF-TrFE-CTFE) a montré un comportement relaxeur, avec des faibles valeurs de polarisation rémanente et une hystérésis pincée. Les hétérostructures mesurées ont montré un comportement électrique complexe à cause de l'hystérésis pincée. Il faudrait dans le futur entreprendre une étude plus poussée pour comprendre les phénomènes mis en jeu dans ces empilements RE/FE.

Enfin, les perspectives ouvertes par ce travail offrent deux principaux chemins pour faire avancer la thématique. Tout d'abord, nous pouvons directement utiliser le dispositif de récupération d'énergie thermique développé dans cette thèse pour construire un exemple d'application concret, comme par exemple un capteur thermique sans fil autoalimenté. Pour ce faire, les briques de base nécessaires, à savoir un interrupteur thermique, un circuit de gestion de l'alimentation et une carte d'émission sans fils, ont été brièvement discutées, montrant les alternatives possibles et les chemins d'optimisation à suivre.

Sinon, le récupérateur lui-même peut être optimisé pour augmenter sa densité d'énergie et son efficacité. Deux idées principales sont proposées ici: le plus simple est de simplement augmenter la quantité de matériau utilisé, soit par la construction d'un harvester plus grand avec la même configuration soit en augmentant la quantité de SMA utilisé dans la configuration actuelle. L'autre option consiste à augmenter le rendement énergétique du matériau piézoélectrique. Pour ce faire, nous avons commencé un travail exploratoire combinant la nanostructuration de P(VDF-TrFE) sérigraphié, visant à améliorer ses propriétés piézoélectriques, et un système d'électrodes interdigitées, permettant de travailler dans le mode 3-3, qui a des coefficients piézoélectriques plus élevés que le mode 3-1. Les chemins ouverts par ce travail semblent prometteurs et doivent être poursuivis.